Buffer Gas Cooled Beams and Cold Molecular Collisions

A dissertation presented

by

David Patterson

to

The Department of Physics

in partial fulfillment of the requirements

for the degree of

Doctor of Philosophy

in the subject of

Physics

Harvard University

Cambridge, Massachusetts

March 2010

Thesis advisor

John M. Doyle

Author

David Patterson

Buffer Gas Cooled Beams and Cold Molecular Collisions

Abstract

The vast majority of techniques for cooling, manipulating, and trapping molecules demonstrated to date rely on specific and unusual features of the molecular species being studied. We present here a suite of tools for cooling a wide variety of molecules, and for creating bright, cold, and slow molecular beams. The buffer gas techniques used depend only on very general qualities of the molecule and we demonstrate them to be widely applicable. Current and future applications to studies of new physics and chemistry are presented.

Contents

Citations to Previously Published Work

Portions of thesis have appeared in the following three papers:

"A bright, guided molecular beam with hydrodynamic enhancement", David Patterson and John M. Doyle, Journal of Chemical Physics **126**, 154307 (2007), doi: 10.1063/1.2717178 ;

"Intense atomic and molecular beams via neon buffer-gas cooling", David Patterson, Julia Rasmussen, and John M. Doyle, New Journal of Physics **11**, 055018(12pp) doi: 10.1088/1367-2630/11/5/055018 ;

"Cooling and Collisions of Large Gas Phase Molecules", David Patterson, Edem Tsikita, and John M. Doyle, Submitted JCCP February 2010

Acknowledgments

I would like to thank everybody who has made the last six years so enjoyable. I would especially like to thank Stan Cotreau and Tom Barrup. Without them I wouldn't have made it.

Chapter 1

Introduction

1.1 Why cold molecules?

Since the invention of laser cooling in 1978[112], cold and ultracold atoms have provided three decades worth of phenomenal results, ranging from ultraprecise spectroscopy to novel quantum phases and quantum information gates. It is now widely acknowledged that it is time for cold molecules to take their turn.

Molecules have extra internal degrees of freedom[1] that are absent in atoms. Manipulation of these degrees of freedom allows for the construction of far more diverse and complex hamiltonians than is possible with atoms. In addition, polar molecules interact with each other and with external systems far more strongly than non-polar atoms or molecules. In many cases it is these strong, tunable interactions can lead to the promise of chemistry that goes qualitatively beyond what can be done with room

[1] All molecules have rotational and vibrational degrees of freedom that are absent in atoms; some molecules have additional degrees of freedom, such as inversion in NH_3 or the Ω doublet structure in the $^3\Delta_1$ state of ThO

$T = 10$ K	High resolution spectroscopy Complex mixture analysis Search for fundamental symmetries Classical and semi-classical collision dynamics
$T = 1$ K	Molecules can be polarized or aligned via external electric or magnetic fields Trapping of low field seeking polar or magnetic molecules Potential for field tunable chemistry Direct observation of dipole-dipole inelastic collisions
$T = 10$ mK	Trapping of high field seeking polar molecules Trapping of large polar molecules Cold controlled chemistry Likely further cooling via evaporative cooling or sympathetic cooling Single rotational state control of large molecules
$T < 1\mu$K	Quantum degeneracy with molecules Quantum phase transitions and multibody physics Ultracold chemistry Low decoherence Q-bit manipulation with polar molecules and mesoscopic systems

Table 1.1: A selection of some of the demonstrated and proposed applications of cold and ultracold molecules. Experiments immediately accessible via the techniques outlined in this thesis are listed in blue

temperature molecular reactions. It is therefore no surprise that there is currently enormous interest in cold and ultracold molecules, in fields as diverse as material science, many body physics, quantum phase transitions, and precision measurement of fundamental constants. Table 1.1 lists a selection of the scientific goals realizable with cold molecules.

In this thesis, tools for producing cold, clean, dense, state selected samples of a wide variety of atoms and molecules will be presented. The methods used to produce these samples are new and quite general, relying on neither unique level structures nor

unusual collisional properties of the molecules. They are applied here to molecules as different as O_2, NH_3, and Naphthalene ($C_{10}H_8$). One can think of a host of immediately possible experiments with molecules from at $T = 1 - 10$ K (listed in blue in table 1.1). Various applications of these tools are presented in chapter 6, including possibilities for extending these techniques into a general method of producing trapped samples of "ultracold anything".

1.2 Molecules are harder than atoms

The same extra degrees of freedom that make cold molecules such a powerful tool present serious challenges to researchers wishing to cool and manipulate neutral molecules.

Two powerful tools used by atomic physicists are notably incompatible, or at least extremely difficult to apply, with molecules. First, laser cooling of molecules has yet to be demonstrated, although proposals exist for certain dipolar molecules[94]. Second, evaporative cooling of low field seeking atoms trapped in magnetic traps has been a crucial tool in making the leap from cold to ultracold. Although proposals for deep, high field seeking traps exist[30], the only demonstrated traps with a depth $>$ 10 mK are traps for low field seeking paramagnetic atoms or molecules, or electric traps for low field seeking polar molecules. Since the absolute ground state of a molecule is necessarily high field seeking, the samples held in these deep traps are in a sense metastable[2] Inelastic scattering between trapped molecules, in which one or

[2]These traps for metastable low field seeking atoms have proven immensely useful. The spontaneous emission limited lifetime of these metastable states is far longer than any realistic experiment run time. Nevertheless, decay from these states to the high field seeking ground state, e.g. in

both of the molecules is exothermically scattered into the untrapped ground state, will therefore lead to trap loss. With very few exceptions, inelastic rates for both magnetic and polar molecules are expected to be far too high to allow for evaporative cooling[13].

It is notable that either low field seeking traps or laser cooling has been used in *every* ultracold[3] atom or molecule experiment to date. For example, while quantum degeneracy has been achieved without laser cooling[32], and without low field seeking traps[3], it has never been achieved without either.

In this thesis we present general techniques to produce cold polar and non-polar molecular beams at temperatures of 2-10K via buffer gas cooling. In some cases, these techniques compete favorably even with cold *atom* sources, and they are in general far brighter than existing sources of cold molecules. Further experiments are presented in which the cold molecules are separated from the buffer gas, providing a general, clean, cold, and slow source of cold molecules.

The techniques developed in this thesis provide high density samples of molecules that are generally cooled to temperatures in the range of 2-10 K. This is cold enough to trap them in a deep, low field seeking trap, but too warm to trap them in any demonstrated high field seeking trap. The great remaining challenge, therefore, is to make the leap from 4 K to 10 mK; once a dense sample of 10 mK molecules has been loaded into a high field seeking trap (for example, a microwave trap or an alternating

majorana losses or via inelastic collisions, is often a limiting factor in these experiments.

[3] "Ultracold" is taken in this thesis to mean "cold enough that atoms or molecules collide via S-wave collisions only". In recent years, especially in the context of cold molecules, "ultracold" has often been used to simply mean "very cold", or perhaps, "about as cold as ultracold atoms." None of the experimental work in this thesis is done in the ultracold regime

gradient trap), further evaporative cooling should be possible. At this point, table 1.1 will go from being a wish-list to a menu.

We have used our newly developed tools to investigate the poorly understood mechanisms for the formation of van der waals dimers at low temperature. In particular we have experimental evidence supporting a "vibrational threshold" model of the formation of molecule-helium complexes at low temperatures, as presented in chapter 5. The tools we have developed to study these processes can be applied to quantitatively study these and other chemical processes at temperatures below 10 K at an unprecedented sensitivity.

In chapter 2, basic buffer gas beams in various regimes are presented, including the theory relevant to efficiently producing beams optimized for either high flux, low forward velocity, or a combination. Demonstrated unguided atomic beams of potassium and ytterbium are presented. In chapter 3, electric and magnetic guides that can separate these beams from the accompanying buffer gas are presented. The guides are demonstrated with cold, guided, state selected beams of ND_3 and O_2. In chapter 4, various methods of loading buffer gas cells, including a versatile, novel method, direct flow loading, are presented. In chapter 5, direct flow loading is used to load naphthalene into a 6 K cryogenic cell. Theoretical and experimental evidence of the role of vibrational spectra in cold two and three body collisions is presented. In chapter 6, various potential future applications of the technologies presented in chapters 2-5 are presented. Of particular note are section 6.1, describing a general, broad spectrum "nose" that could rapidly resolve complex gas mixtures at an unprecedented level of sensitivity, and section 6.5.2, presenting a synthesis of many of the techniques

demonstrated in this thesis to continuously load a high flux of molecules into a trap.

Chapter 2

Slow Beams, Bright Beams, and Slow, Bright Beams

Cold molecules are, by definition, out of equilibrium with their comparatively warm environment. This non-equilibrium is a prerequisite for any manipulation of the molecules, and in many cases it is residual thermalizing processes that limit cold and ultracold experiments[1]. The molecular beam - a stream of molecules in vacuum - is an essential tool for providing this thermal disconnect. The beam allows a physical separation between the "production region", which is essentially in thermal equilibrium, and the "experiment region," which is not. Equilibration rates - for example, collisions rates with background gas - can differ by as much as 8 orders of magnitude between these regions[2]. Atomic and molecular beams are essential

[1]Two examples are background gas collisions, and the absorbtion of blackbody microwaves by trapped polar molecules

[2]A beam is not strictly necessary, and is not used in many buffer gas loading experiments[59]; in these cases, the required enormous change in equilibration rates comes from manipulating buffer gas vapor pressures, which are a strong function of temperature

components of the vast majority of modern cold atom and molecule experiments.

This chapter is organized as follows: section 2.1 outlines figures of merit for a cold beam source. Section 2.2 describes conventional, 300 K beam sources. Section 2.4 describes the theory of buffer gas beams, section 2.5 describes results for a variety of beam designs, and section 2.6 describes potential improvements to the designs demonstrated to date.

2.1 An abstract beam experiment

Figure 2.1 shows a simplified schematic of a generic beam-based trap loading experiment of an atomic or molecular species A, of mass M. The system consists of a beam source, a method or methods to manipulate the phase space of the beam, and a final trap. Examples of phase space manipulation are laser cooling, beam guides, velocity selection and stark deceleration. Often the primary goals of this stage are slowing the beam to a trappable velocity and separating it from the buffer gas. A more specific example of an experiment of this kind is shown in figure 6.15.

The use of a trap is necessary for many experiments. It should be noted that phase space manipulation in many cases continues after the trap is loaded. Many cooling techniques, [for example evaporative cooling, sympathetic cooling with a second species, and adiabatic manipulation of the trap volume] are only possible once the sample is trapped.

An experiment of this kind can in general use only molecules in the beam with a total translational energy of less than a few K. Sections 2.4.3 and 2.4.6 contain more details on high flux, slow beams optimized for this type of experiment. Continuous

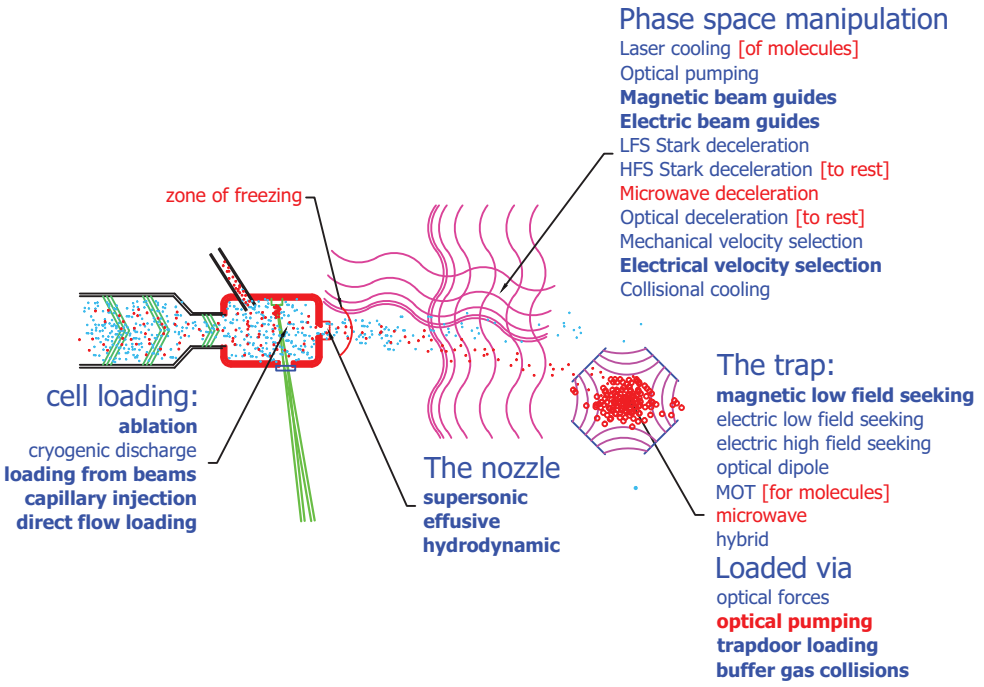

Figure 2.1: A simplified schematic of a beam-based trap loading experiment of an atomic or molecular species A of mass M. The apparatus consists of a beam source, some method to manipulate (and perhaps compress) the phase space occupied by the beam, and a final trap. At some point in the loading sequence, energy must be dissipated by this system. Demonstrated (red) and proposed (blue) methods of each stage of this system are listed. Techniques presented or proposed in this thesis are listed in **bold**.

irreversable loading of traps from beams is discussed in more detail in section 6.5.2.

2.1.1 Beam figures of merit

Atomic and molecular beams - streams of atoms or molecules in vacuum - have a long and successful history, and are essential components in a huge range of present day experiments. The vast majority of these beams are produced in sources that are at room temperature or above, and in sources which are close to thermal equilibrium. For example, the partial pressure of the species of interest A in the source is generally lower or equal to A's saturated vapor pressure[3]. Buffer gas beams are different - the source is significantly colder than room temperature, and the partial pressure of A in the source is enormously higher than its low temperature saturated vapor pressure.

In any buffer gas beam experiment, the translational (and rotational, in the case of a molecule) degrees of freedom of the gas mixture are in approximate thermal equilibrium inside the cell, and out of equilibrium once it is in the beam. It is therefore natural to consider the characteristics of the 'beam' beginning at the time of the last collision between a typical molecule of species A and the buffer gas. This is the location of the "zone of freezing" marked in red in figure 2.1. The beam at this moment can can be characterized by the following figures of merit:

- $v_{forward}$, the mean forward velocity of a molecule in the beam
- T, the temperature of the beam *in the moving frame*. In many cases the beam is not in perfect equilibrium, but to good approximation we can take $T = \frac{3m}{2k_b}\langle v - \langle v \rangle \rangle^2$

[3]This has significant consequences in the case of seeded supersonic beams of radicals, which cannot exist in thermal equilibrium at any temperature. The buffer gas beams presented in this thesis are in fact especially attractive as sources of radicals

- ϕ, the total flux of the beam, in molecules/second[4].

With the exception of an optical force slower, almost all beam slowing methods can remove only a few Kelvin of forward energy per stage. It is therefore usually desirable to begin with a beam which has $v_{forward}$ as low as possible. In addition, (this time with the exception of laser cooling), the phase space manipulation listed in figure 2.1 is in general reversable, so the ultimate temperature of the beam can never be lower than T. [Kinematic cooling[34], is irreversable but generally leads to sample heating, rather than cooling] Since traps are in general very shallow compared to available cryogenic temperatures, we also want T as low as possible for any trapping experiment. Finally, it is clear that a large beam flux ϕ will lead ultimately to higher trap densities, collision rates, and statistics in almost any experiment.

In summary, the ideal beam source would be *slow, cold*, and *bright*.

2.2 Room temperature technologies

Two general classes of technologies, thermal beams and supersonic beams, have been demonstrated for producing atomic and molecular beams from warm (300 K or warmer) sources:

[4]In many cases the relevent figure of merit is actually not the total flux ϕ, but brightness, defined as the flux per unit solid angle. In some cases - particularly with heavy species entrained in a light buffer gas - beams have been demonstrated to have significant "forward peaking", enhancing brightness but not ϕ

Thermal beams

This is the oldest and simplest technology. At its core, a thermal beam source is simply an oven with a hole in the side. In order to produce a significant flux, the oven temperature T_{oven} must be high enough to produce a significant vapor pressure of A. The absence of a carrier gas in these systems means they typically operate in or near the effusive regime (see section 2.4); as a result, these sources typically have $v_{forward} \approx \sqrt{2k_bT_{oven}/M}$, and $T \approx T_{oven}$.

Various groups [83][29] have produced slow, cold beam sources by using velocity selective beam guides or turbines to select the small fraction slow moving molecules from such a beam. These sources have the advantages of being continuous, general, and simple, although the versions demonstrated to date have been limited to rather low fluxes. The oven in these sources must be run in the deeply effusive regime[5], as the slow molecules of interested can easily be knocked out of the first stage of the beam guide by other, faster molecules as discussed in section 2.4.3. These sources also in general do not cool internal degrees of freedom of species A, such as rotation. This is irrelevant for atoms but is a significant disadvantage for sources of any but the smallest of molecules.

Supersonic beams

In a supersonic beam source, the species A is mixed with a high pressure (1-2200 bar) inert carrier gas - typically helium, neon, argon, or xenon - and sprayed through a small (typically < 1 mm) nozzle into a vacuum[65]. There is considerable

[5] *effusive* is discussed more in section 2.4.2; for now, an effusive beam can be taken as a beam with low enough flux that there are no collisions in the beam.

variation in nozzle design, including nozzles as small as 1 μm[80]. The gas rapidly expands, accelerates, and adiabatically cools. This results in a very low T and high instantaneous ϕ, but carries the expense of a high $v_{forward}$ (300 m s^{-1} or greater typical). This tool has proved to be enormously valuable to molecular spectroscopists, and is the first stage of all deceleration based experiments with molecules to date. [10][23] Many of the suggested applications in chapter 6 involve improvements to these experiments with the beam sources presented here (in place of a conventional supersonic source).

Cryogenic supersonic expansions have been demonstrated prior to this work. Jets of pure helium have been made with stagnation temperatures as low as 6 K[14], in particular in order to study the extremely weakly bound He_2 molecule. These experiments produced very low final temperatures and high three body recombination rates, but differ from the work demonstrated in this thesis in that the nozzle holds helium gas in *equilibrium* at 6 K - this implies that the technique would have failed with anything except a beam of pure helium. It is critical to the work in this thesis that the conditions within the nozzle are highly out of thermal equilibrium; the atom or molecule to be studied must be ejected into the beam before it collides with and freezes to the cold cell walls.

2.3 This work

The beams discussed in this work are efforts to take advantage of the low starting temperature of cryogenic buffer gas cells to produce bright beams that are *slower* than conventional supersonic sources and both *slower* and *colder* than conventional

thermal sources. Compared to conventional, 300 K sources, these buffer gas methods lead to higher fluxes and more flexibility in terms of species, especially radicals[6].

The optimal beam source depends on the application. For example, the sources optimized for high ϕ and low T are particularly well suited for high resolution spectroscopy[107], while the sources optimized for low $v_{forward}$ are in general aimed at guiding and trapping experiments (see section 2.4.5).

2.4 Theory of supersonic, hydrodynamic, entrained and effusive buffer gas beams

2.4.1 Within the cell: predicted efficiency

The fraction f of species A that ends up in the molecular beam depends on the dynamics within the cell. Consider the buffer gas cell shown in figure 2.2. The cell - a simple box - is filled with a mixture of buffer gas of mass m, and a small fraction of "impurities" of species A, mass M. The mixture is assumed to thermalize to a temperature T before it exits the nozzle.

Atoms and molecules can leave the cell via two processes: by diffusing to the cell wall (with a small fraction of the molecules diffusing out of the aperture) or by being entrained in the helium flow that is continuously pouring through the aperture. If the diffusion time for an atom or molecule ($\tau_{diffusion}$) is much shorter than the

[6]conventional supersonic beams can produce beams of cold radicals, but in general at much lower fluxes than similar beams molecules. Debate exists over the exact limiting mechanism, but it is very plausibly radical-radical collisions within the high density stagnation chamber and the very first part of the beam

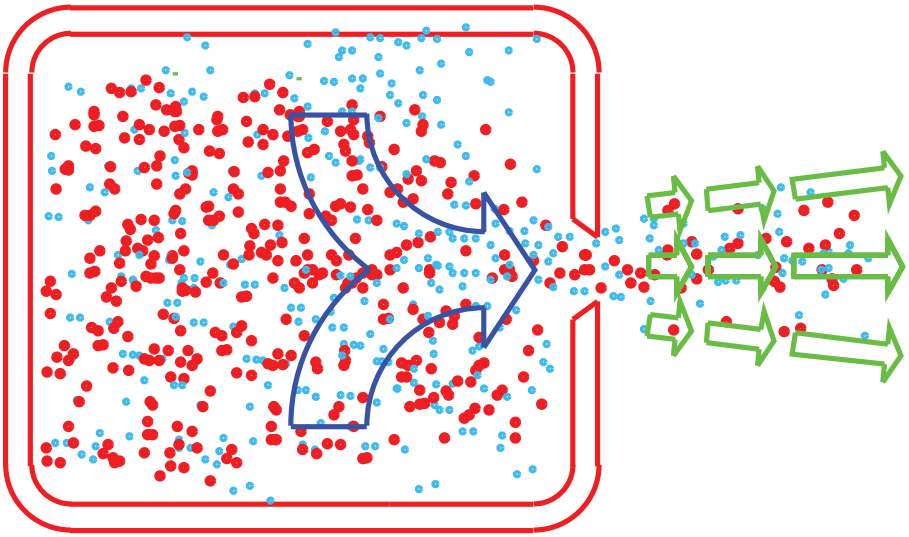

Figure 2.2: A simplified buffer gas beam source. Two dimensionless numbers, γ and N, largely determine the final beam dynamics. Dynamics *within* the cell are governed by $\gamma \equiv \frac{\tau_{diffusion}}{\tau_{pumpout}} \approx \frac{An\sigma}{4L}$ and in general are either *diffusive* ($\gamma < 1$) or *hydrodynamic* ($\gamma > 1$); see section 2.4. Dynamics of the beam are determined by N, the number of collisions between a typical molecule of A and the buffer gas *outside* of the nozzle. These beams vary between perfectly *effusive* ($N = 0$) and *supersonic* ($N >> 1$); see section 2.4.2. In general, the flux ϕ is a function of γ; $v_{forward}$ and T depend on N and T_{cell}.

characteristic time it takes a helium atom (or entrained species) to be pumped out of the cell ($\tau_{pumpout}$), hydrodynamic effects can be ignored. In this diffusive limit the fraction that escape into the beam from a cell of side length L with aperture area A is $f \approx A/\pi L^2$ (about about 10^{-3} for a typical geometry)footnoteThese calculations assume a roughly symmetric cell, $L_x \approx L_y \approx L_z$. This type of cell generally maximizes beam flux ϕ; for other geometries, the analysis of the section can be used in reasonable approximation taking $L = L_{min}$. If, on the other hand, $\tau_{diffusion} \gg \tau_{pumpout}$, a large fraction of the molecules are entrained in the buffer gas flow and are swept into the

beam. The dimensionless parameter

$$\gamma \equiv \frac{\tau_{diffusion}}{\tau_{pumpout}} \tag{2.1}$$

therefore provides a good indication of dynamics within the cell, with $\gamma \ll 1$ implying the diffusion limit and $\gamma \gg 1$ implying the entrainment limit.

The entrainment being discussed here is *not* the same effect that is seen in typical supersonic nozzles, where collisions *within the nozzle* (as opposed to the volume well before the nozzle) are important and flow velocities are large compared to the sonic velocity. The mean flow velocity of helium within our buffer gas cells is typically much less than the speed of sound in the helium gas.

Both $\tau_{diffusion}$ and $\tau_{pumpout}$ can be estimated for simple geometries. Consider a cell, with side length L and an aperture of area A, filled with gas of density n.

The flow velocity at the center of the aperture is about mach 1, or

$$|\bar{v}| = \sqrt{2k_bT/m}$$

Correcting for the fact that the flow is slower near the aperture edge, total flux through the aperture is[86]

$$\phi = \frac{\bar{v}nA}{4} = \frac{nA}{4}\sqrt{2k_bT/m} \tag{2.2}$$

atoms/second. This is the result for an aperture in the molecular flow regime, but the result is only changed by a factor of 2.6 if operating in the viscous regime. At still higher flows, the flow would become turbulent and equation 2.2 no longer holds[7]

[7]turbulence is unusual in gasses at the low densities typical of buffer gas cells; even at sonic flow velocities, the Reynolds number is always less than $L < l$; a 1 cm scale cell will not be turbulent at any density less than $n \approx 5 \times 10^{17}$

The total number of atoms within the cell is

$$N = L^3 n$$

So the pumpout time $\tau_{pumpout}$ is given by

$$\tau_{pumpout} = \frac{N}{\phi} = \frac{L^3}{4A}(k_b T/m)^{-1/2} \tag{2.3}$$

For $\tau_{diffusion}$, consider first the case where $m = M$, and the A-helium elastic scattering cross section is given by σ. In this case, the mean free path λ is given by

$$\lambda = \frac{1}{n\sigma}$$

The mean free time $\bar{\tau}$ is given by

$$\bar{\tau} = \frac{\lambda}{\bar{v}} = \left(\frac{m}{2k_b T n^2 \sigma^2}\right)^{1/2}$$

The atom needs to take $\approx \frac{L^2}{4\lambda^2}$ steps in order to reach the cell wall and stick; this leads to

$$\tau_{diffusion} \approx \frac{L^2}{4\lambda\bar{v}} \approx \frac{L^2 n\sigma}{4}\left(\frac{m}{2k_b T}\right)^{1/2} \tag{2.4}$$

Equation 2.4 in fact holds for $M \neq m$ as well; this is discussed in greater detail in section 4.2.1.

Putting together equations 2.1, 2.3, and 2.4, we get

$$\gamma = \frac{kAn\sigma}{L} \tag{2.5}$$

Where k is a dimensionless constant of order unity.

It is informative to write equation 2.5 in terms of the flow rate ϕ, which can be controlled, rather than n, which depends on ϕ and the geometry. From

$$\phi = \sqrt{n^2 A^2 k_b T / 8m}$$

We get

$$n = \frac{4\phi}{A}\left(\frac{m}{2k_b T}\right)^{1/2} \tag{2.6}$$

or 2.5

$$\gamma = \frac{4k\phi\sigma}{L}\left(\frac{m}{2k_b T}\right)^{1/2} \tag{2.7}$$

Equation 2.7 is extremely simple, as most of the parameters are fixed; the dependence on A has dropped out. Evaluated in meaningful units, assuming $k = 1$ and helium buffer gas at $T = 4.2$ K, it becomes simply

$$\gamma = \frac{1.21\phi \text{ [sccm]}}{L \text{ [cm]}} \tag{2.8}$$

This simple model therefore predicts that the efficiency f, defined as the ratio of beam flux to the flux entering the cell, will be nearly unity for $\frac{An\sigma}{L} > 1$, and drop rapidly - eventually to $f \approx AL^{-3}$ - for $\frac{An\sigma}{L} \ll 1$.

Figure 2.11 shows the measured efficiency as a function of $\gamma = \frac{An\sigma}{4L}$

f for intermediate γ

There is of course an intermediate regime, for $0 < \gamma < 1$. In this regime, molecules which diffuse randomly to a volume near the aperture tend to be hydrodynamically

swept out into the beam, but molecules that end up elsewhere in the cell are not effected by this wind.

Approximate scaling in this regime can be found by identifying a size scale L_{eff} where hydrodynamics dominate. By definition, for $\gamma = 1$, $L_{eff} = L$. Since $\gamma \propto L^{-1}$, for $\gamma < 1$, $L_{eff} \approx \gamma L$. The efficiency is expected to scale as the ratio of the area of the cell to the area of this "hydrodynamic volume". This leads to the following qualitative model of the total efficiency f:

$$f = \begin{cases} \frac{A}{6L^2} & \text{for } \gamma \leq \sqrt{A/6L^2}\,, \\ \gamma^2 & \text{for } \sqrt{A/6L^2} < \gamma \leq 1\,, \\ 1 & \text{for } 1 < \gamma \end{cases} \tag{2.9}$$

This efficiency f as a function of helium flow ϕ is plotted in figure 2.3.

2.4.2 Within the Nozzle: predicted $v_{forward}$

In the previous section, we showed that the flux ϕ of the beam depends on the dynamics within the cell. In the section, we show that the distribution of forward velocities in the beam depends on the mass M of species A, the mass m of the buffer gas, and N, the number of collisions a typical molecule of A undergoes while it is in the beam.

As in section 2.4, consider a beam consisting of a small fraction of species A "impurities" of mass M mixed with a much larger flow of a nobel gas of mass m. The mixture is assumed to thermalize to a temperature T before it exits the nozzle. Within the cell, the gas flow is well approximated by an incompressible fluid. That is, the microscopic velocity $\bar{v} \approx \sqrt{2k_bT/M} >> v_{flow}$. A microscopic observer would

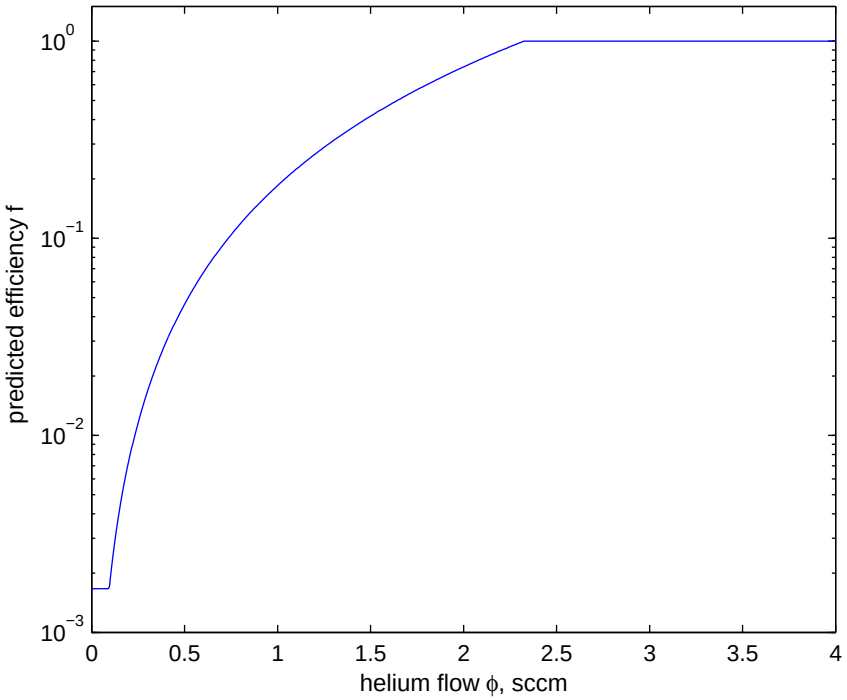

Figure 2.3: Equation 2.9 plotted for various values of helium flow ϕ. This plot assumes a cell of size $L = 1$ cm and a round aperture of radius $r = 0.5$ mm; the difference between the diffusive and hydrodynamic regimes is almost three orders of magnitude. The qualitative agreement with experiment (figure 2.11) is reasonable. There are no free parameters in this 'fit'.

see helium and impurity molecules passing with a general drift to towards the nozzle, but in general molecules are moving in every direction. In other words, the gas is roughly in thermal equilibrium.

As the mixture passes through the nozzle and expands, this equilibrium will be broken. Depending on the number of collisions N within and just outside the nozzle, such a beam can operate in one of three regimes:

- *effusive*, characterized by $N < 1$ collision. In such beams, molecules of A

typically undergo no collisions once they are outside of the cell. These beams have a forward velocity of order $\bar{v} \approx (2k_bT/M)^{1/2}$ and relatively low flux.

- *entrained*, characterized by $1 < N < 100$ collisions; the flow through the nozzle is hydrodynamic, but isothermal; the species A is in local moving-frame equilibrium with the carrier gas. These beams typically have a large flux enhancement compared to effusive beams due to hydrodynamics within the cell, as described in section 2.4 and reference[76]. Entrained beams have a modestly boosted mean forward velocity of $\bar{v} \approx 1.5(2k_bT/m)^{1/2}$. Note that for $m = M$, this forward velocity is only slightly above that of the effusive source.

- *fully supersonic*, characterized by $N > 1000$ collisions in and outside the nozzle. In this regime, there is significant adiabatic cooling as the gas expands into the vacuum; the forward velocity distribution is sharply peaked around a velocity $\bar{v} \approx 2.4 \times (2k_BT/m)^{1/2}$[65]. This is only a factor of $\sim$2 faster than effusive sources for $M = m$, but much more for $M \gg m$; in addition, there "slow tail" of the velocity distribution is highly suppressed in these beams.

Figure 2.4 and 2.5 show the forward energy spectrum to be expected in each of these regimes for various values of M and m.

The fundamental goal of a most of the beams presented in this chapter is to realize a beam that is both *bright* and *slow*.

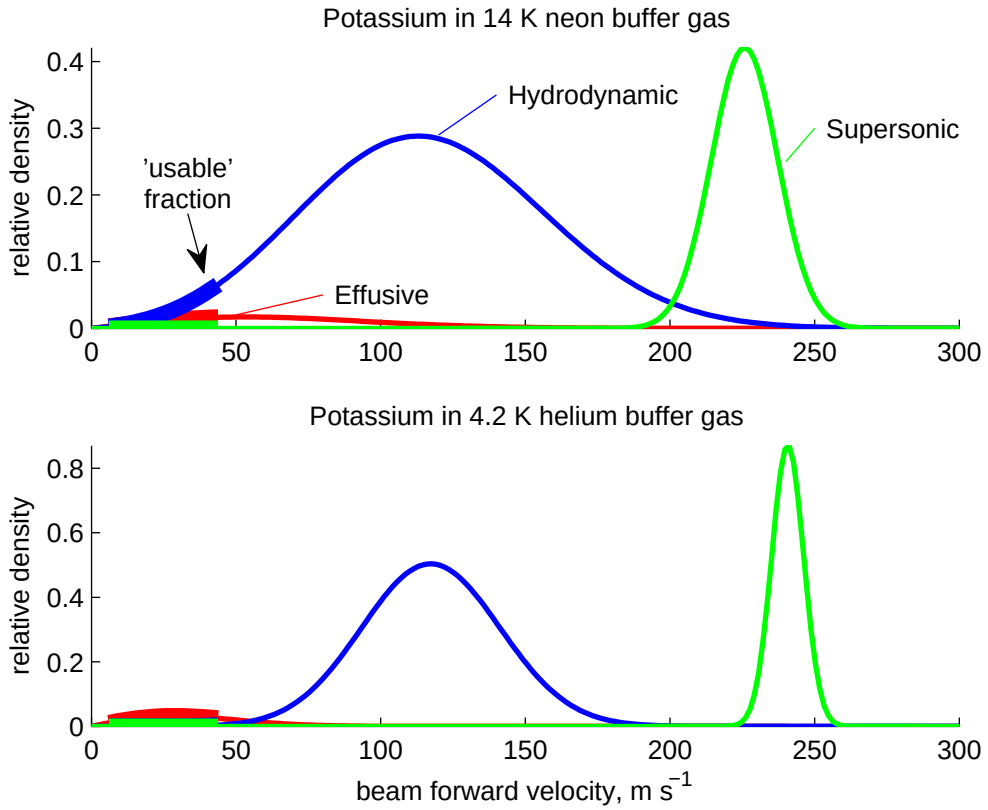

Figure 2.4: Simulated forward velocity distributions for buffer gas beams in various regimes; for this simulation the potassium ($M = 40$) is used as the species to be studied. The upper plot shows an effusive, entrained, and supersonic beam with a 14 K neon buffer gas; the lower plot shows the same three regimes with a 4.2 K helium buffer gas. The heavy line labeled 'usable fraction' represents the portion of the beam with energies below 5 K, and represents the upper end of the typical energy range that can be loaded into a low fields seeking electric or magnetic trap. The effusive beam is shown with a smaller total flux than the other beams, but this flux reduction is greatly underestimated in this plot.

Section 2.4.7 contains further discussion of neon as a buffer gas.

2.4.3 Almost effusive beams

Figure 2.4 shows theoretical forward velocity distributions for $N = 0$, 1 and 30 collisions. It is not unusual to be interested in the very slowest portion of a beam. Naively, one might think that the criteria for being 'an effusive source' would be

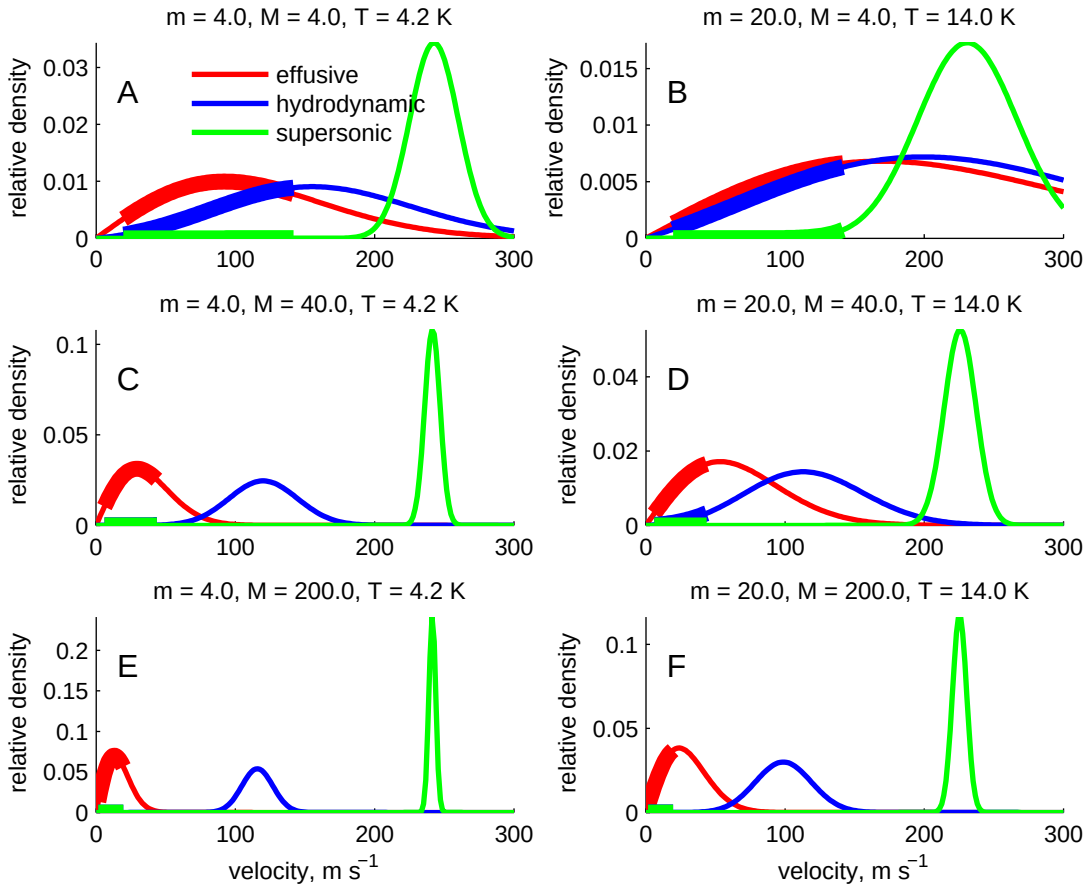

Figure 2.5: Simulated forward velocity distributions for buffer gas beams in various regimes, various values of carrier mass m, and various values of impurity mass M. As in figure 2.4, the "trappable" fraction between 1 K and 5 K is marked in bold. The left hand plots (A, C, and E) show beams mediated by 4.2 K helium; the right hand plots show beams mediated by 14 K neon. Unlike figure 2.4, all curves are normalized to the same total flux, although in fact the effusive source (red curves) would be dramatically lower.

that the average number of collisions $N < 1$. This is true if the figure of merit is the mean forward velocity, $v_{forward}$, but if the experimenter is interested in the very slowest molecules, this is no longer the case. Figure 2.4.3 shows a histogram of calculated velocities expected for a "nearly effusive" potassium source at $T = 6$ K,

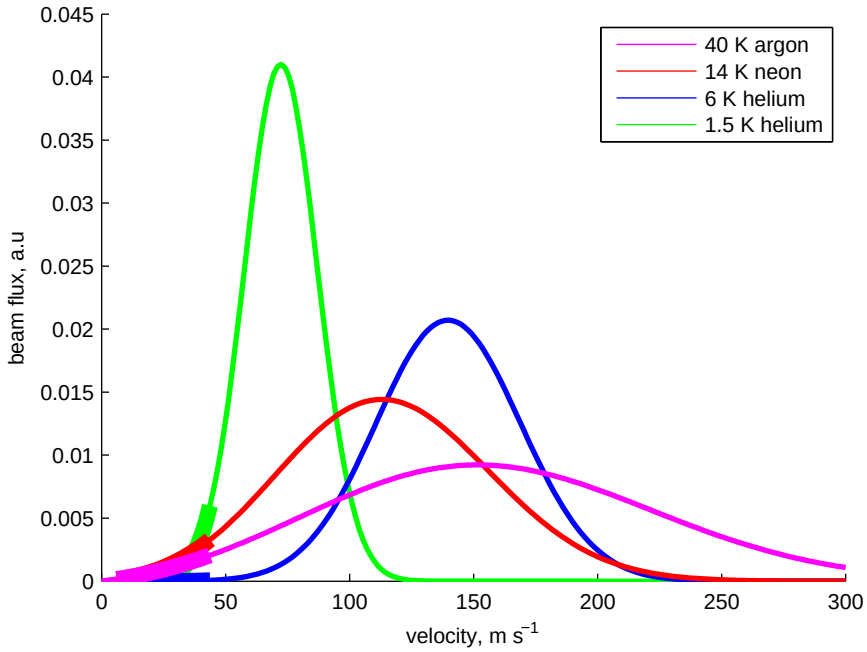

Figure 2.6: Simulated forward velocity distributions for potassium ($M = 40$) entrained in 1.5 K helium, 6 K helium, 14 K neon, and 40 K argon buffer gas beams. The warm neon beam is competitive with a 1.5 K helium, and substantially outperforms a 6K helium source.

with $N = 0, 0.5$, or 1. In the case of $N = 1$, the mean energy of the potassium beam has increased very little, but the very slowest atoms have been all but eliminated. This is because these slow atoms spend much longer in high-density regime near the nozzle, and are proportionally much more likely to be repeatedly hit by helium atoms streaming past. This effect gets dramatically worse for heavy species, or for situations where $D_{trap} << T$. Sources of cold molecules with that select the very slowest molecules from a warm source suffer greatly from this phenomenon[83].

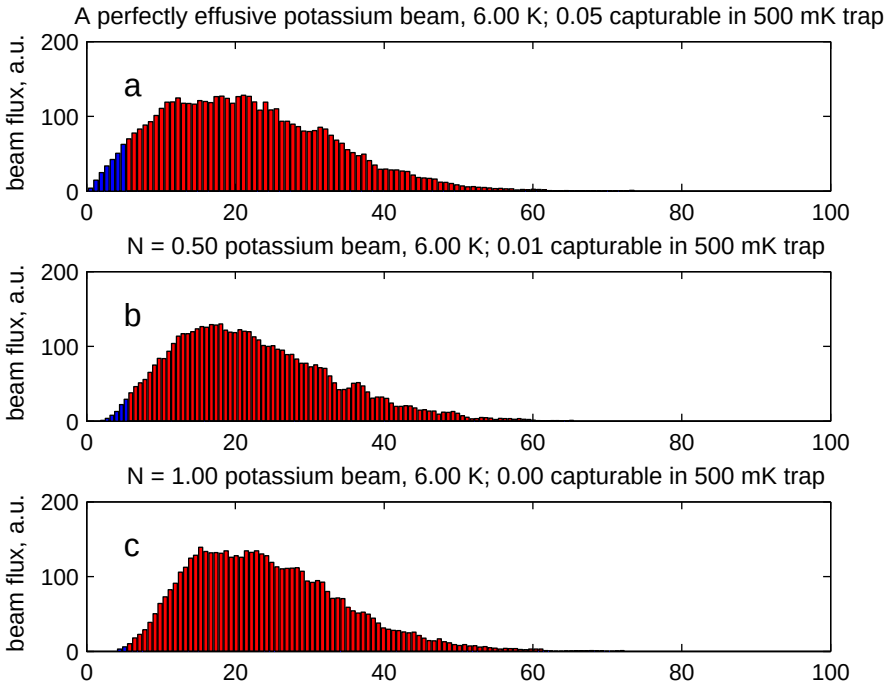

Figure 2.7: Numerically simulated forward velocity distributions for potassium ($M = 40$) beams in 6 K helium in the 'almost effusive' regime. (a): An ideal effusive beam; (b) and (c): Beams where the mean number of collisions N is set to 0.5 and 1 respectively. The blue portion of the distrubution is the fraction that could be loaded into a 500 mK deep trap. Note how these slowest atoms are disproportionally disturbed by even a small number of collisions. The selective acceleration of the slowest moving beams leads to a slight cooling of the velocity distribution in the moving frame.

2.4.4 Estimating N

'Accelerating' collisions, which contribute to the velocity boost seen in entrained beams, can occur as soon as the buffer gas is no longer in approximate lab-frame equilibrium. In the microscopic picture, this occurs once the macroscopic flow velocity v_{flow} is on the same order as the microscopic velocity $|\bar{v}| \approx \sqrt{2k_bT/m}$. This becomes true once the gas is within ≈ 1 diameter of the nozzle.

For most species A we have $\bar{v_{He}} > \bar{v_A}$, so the position dependent collision rate $\Gamma(r)$ is given in reasonable approximation by

$$\Gamma(r) = \bar{v}_{He} n(r) \sigma$$

The total number of collisions is therefore

$$N = \int_0^\infty \Gamma(t)\mathrm{dt} = \int_0^\infty \frac{\Gamma(r)}{v_A}\mathrm{dr} = \int_0^\infty \frac{\bar{v}_{He} n(r)\sigma}{v_A}\mathrm{dr} \tag{2.10}$$

For large N, v_{He} varies as the beam cools, and v_A varies as the the beam becomes 'boosted'. In this case equation 2.10 must be solved numerically, but a reasonable approximation can be reached by assuming $\bar{v}_{He} \approx \sqrt{2k_bT/m}$, and $v_A \approx \sqrt{2k_bT/M}$. In general it takes about M/m collisions to thermalize species A with helium (see section 4.2.1), so these assumptions will be valid if $N < M/m$. These assumptions lead us in general to *overestimate* N.

Under these assumptions, equation 2.10 becomes

$$N \approx \left(\frac{M}{m}\right)^{1/2} \sigma \int_0^\infty n(r)\mathrm{dr}$$

The density $n(r)$ for a slit nozzle, of width r_1 and length r_2 (see section 2.4.5) is given in equation 2.11, with n_0 the internal cell density. For a round nozzle, take $r_1 = r_2$.

can be approximated as

$$n(r) = \begin{cases} \frac{n_0}{4} & \text{for } 0 < r < r_1\,, \\ \frac{n_0 r_1}{4r} & \text{for } r_1 < r < r_2,\,, \\ \frac{n_0 r_1 r_2}{4r^2} & \text{for } r_2 < r \end{cases} \tag{2.11}$$

This gives

$$N \approx \frac{n_0 \sigma r_1}{4} \left(\frac{M}{m}\right)^{1/2} \left(\int_0^{r_1} \mathrm{d}r + r_1 \int_{r_1}^{r_2} \frac{\mathrm{d}r}{r} + r_1 r_2 \int_{r_2}^{\infty} \frac{\mathrm{d}r}{r^2}\right)$$

or

$$N \approx \frac{n_0 \sigma r_1}{4} \left(\frac{M}{m}\right)^{1/2} \left(2 + \ln \frac{r_2}{r_1}\right) \tag{2.12}$$

For the case of a round aperture, $r_1 = r_2$, and we get

$$N \approx \frac{n_0 \sigma r_1}{2} \left(\frac{M}{m}\right)^{1/2} \approx \frac{2r_1}{\lambda} \left(\frac{M}{m}\right)^{1/2}$$

Using equation 2.6, we get as a function of ϕ

$$N \approx \frac{\phi \sigma}{r_2} \left(\frac{M}{2k_b T}\right)^{1/2} \left(2 + \ln \frac{r_2}{r_1}\right) \tag{2.13}$$

Under typical conditions, of $L = 1$ cm, $r_1 = r_2 = 0.1$ cm, $\phi = 1$ sccm, and $M = 40$ (potassium), we get $\gamma \approx .4$ and $N \approx 100$ - a bright, but highly boosted, beam.

2.4.5 Bright *and* effusive?

The ideal source would be bright and slow; that is, we want $\gamma \gtrsim 1$ and $N \ll 1$. Assembling equations 2.5 and 2.12, and assuming for now a circular aperture, we get

$$\gamma \approx \frac{r^2 n_0 \sigma}{L} \tag{2.14}$$

and

$$N \approx 2n_0\sigma r \left(\frac{M}{m}\right)^{1/2} \tag{2.15}$$

Solving for the dimensionless figure of merit $\frac{\gamma}{N}$ gives

$$\frac{\gamma}{N} = \frac{r}{8L}\left(\frac{m}{M}\right)^{1/2} \tag{2.16}$$

As $r < L$ for obvious physical reasons, and in general $m < M$, it is apparent that $\frac{\gamma}{N} > 1$ is impossible for such a source. Figure 2.4 illustrates this fundamental frustration of trying to study or trap cold molecules in beams. In the hydrodynamic regime, beams are very *bright*, as a significant fraction of the molecules in the cell are swept into the beam. Effusive beams contain a large fraction of *slow* molecules. Equation 2.16 is nevertheless apparently promising; it suggests that beams with small N and reasonable γ could be produced from small cells with large apertures in them.

Equation 2.16 suggests that the simplest way to maximize $\frac{\gamma}{N}$ and satisfy the criteria of equations 2.14 and 2.15 is to make a small cell (small L) with a large aperture (large r). Unfortunately, the density n in such cells is in general too low to *produce* the cold samples in the first place. Most of the cell loading techniques outlined in chapter 4 require the mean free path λ to be much smaller than L. The exception is cells loaded directly from molecular beams, as in [22]; A large aperture cell based on such a source is in fact a reasonable proposal, but has yet to be demonstrated. Figure 2.8 illustrates a hypothetical experiment based around this source.

If we constrain ourselves to more conventional cell loading techniques, the criteria of equations 2.14 and 2.15 must be coupled with a third 'source' criteria. Although this criteria varies with source, and in fact with species, it is generally true that we

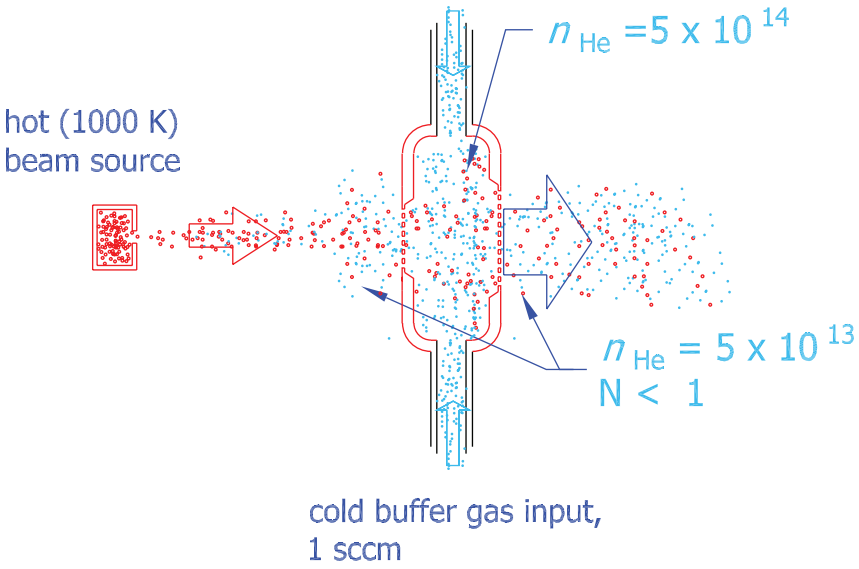

Figure 2.8: A "magic plate" beam source that can run at extremely low buffer gas densities. A hot beam source is aimed at a plate with mesh on each side; after it enters the plate, about 5% of the (now cooled) input gas diffuses through the output mesh. The helium flow is tuned so the incoming beam undergoes just a few collisions as it diffuses through the plate; mesh inputs and outputs ensure that $N < 1$ on both the input and output sides of the plate. A plate operating at 4 K would have an estimated total efficiency ϕ_{out}/ϕ_{in} of 1%, and could easily run in the effusive regime due to the low helium density. This would result in an increase the rotational and translational phase space density of a molecular beam by 4 orders of magnitude. The system would place minimal gas loads on the cryogenics compared to other cold sources, due to the low required helium density.

need at least 10 collisions within the cell to thermalize the incoming, hot gas. This criteria in it's weakest form is therefore

$$n_0 \gtrsim 10/\sigma L \tag{2.17}$$

This "source" criteria directly contradicts the direction that equation 2.16 pushes us in, leaving the experimenter in a difficult position. Indeed, simple helium filled buffer gas cells with round apertures have only been used to produce either high flux, boosted beams [77], or very low flux, effusive beams [71].

The cells considered up to this point - simple boxes with holes in them - are attempting to achieve two tasks - appropriate conditions for cell loading and appropriate conditions for beam collisions - with only one free parameter. Such simple geometries work well for hydrodynamic, highly boosted beams, but effusive beams with any reasonable flux are unrealizable.

To further illustrate this point, let us consider a numerical example. Consider our 'typical' cell with $L = 1$ cm, $r_1 = r_2 = 0.1$ cm, $\phi = 1$ sccm, $M = 40$ (potassium), and T =4 K. The density within this cell is $n_0 \approx 2 \times 10^{16}$; our dimensionless parameters of $\gamma \approx .4$ and $N \approx 100$ imply a bright, but highly boosted, beam.

If we wished to adjust this experiment to set $N < 1$ - an effusive source - it is natural to begin by reducing r. The density $n_0 \propto \phi r^{-2}$, so reducing r while keeping ϕ constant would rapidly increase the density in the cell. If we (somewhat arbitrarily) dictate that n_0 will be kept constant, and reduce r by a factor of 100, we end up with $r = 10$ μm, $\phi = .01$ sccm, $n_0 = 2 \times 10^{16}$, $\gamma \approx .004$, and $N \approx 1$. Even ignoring the inevitable plugging of the nozzle that this very small aperture will lead to, this very small γ is a dealbreaker - the efficiency f, estimated from 2.9, would be 10^{-5}, barely better than the 'purely effusive' value of $f \approx 10^{-6}$.

Somewhat counterintuitively, we do [slightly] better by *enlarging* $r = r_1 = r_2$; the drop in n more than makes up for the longer path length in the nozzle. However, even with $r = 1$ cm - the cell is now a box with one side missing - we have $N \approx 10$. We have no alternative but to reduce ϕ by a factor of 10 as well. This will reduce γ by a factor of 10, and f by a factor of 100 - but the situation is in fact even worse than this. The density "inside" this extremely open cell has dropped by a factor of

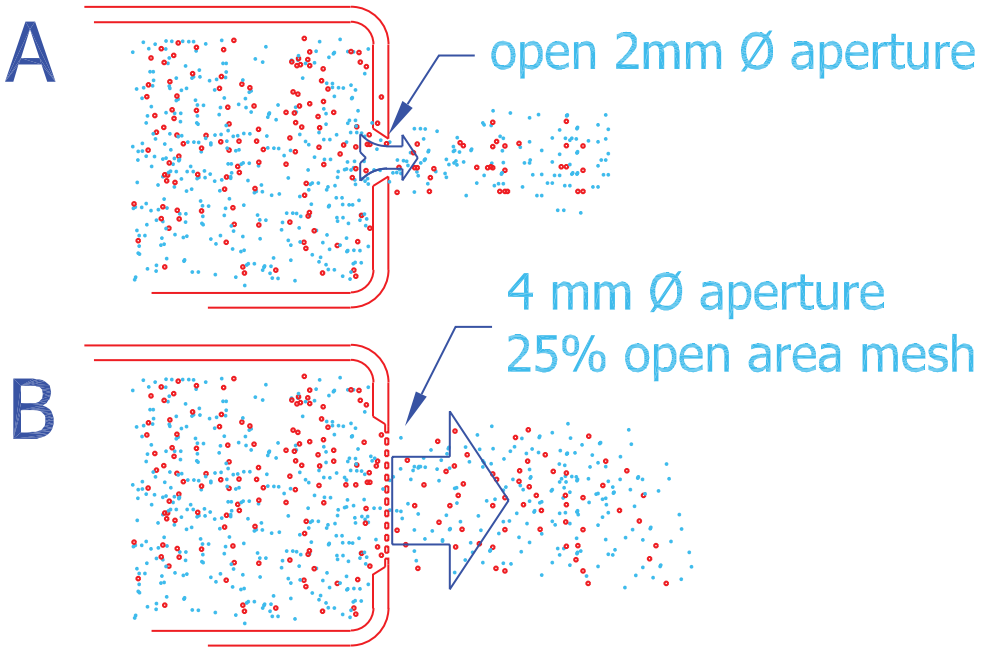

Figure 2.9: An open aperture (A), and an equivalent open area mesh covered aperture (B). A 25% transparent mesh will moderately reduce N, at the price of a physically larger source.

100. Ablation yields will be abysmal even before they are further decreased by a low f; and in fact our usual assumptions about thermal equilibrium within the cell are by now highly suspect.

We therefore examine some more complex cell geometries in efforts to satisfy equations 2.14,2.15, and 2.17.

Mesh covered nozzles

Our first attempt to achieve bright, slow beams was to put a piece of metal mesh across the exit aperture, as shown in figure 2.9. This reduces the area of the aperture and the beam flux, but the hope was that it would more significantly reduce beam forward velocity, resulting in a net gain of slow molecules. This is a standard way

to throttle high velocity flows, and as shown in figure 2.16, it is to some degree successful. In order to compare equivalent systems, the total open area of a mesh covered aperture must be equal to the total area of an open aperture. This means that an open aperture of radius r_{open} must be replaced by a larger aperture covered with mesh of transparency f, with radius $r_{mesh} = r_{open} f^{-1/2}$.

This substitution reduces N in two ways. First, a mesh of transparency f implies that the density outside the mesh is $\approx 1/f$ times lower than the density in the cell; this reduces the collision rate outside the nozzle by a factor of $\approx f^{-1}$. Taking into account $r_{mesh} = r_{open} f^{-1/2}$, this leads to a net reduction of N by a $f^{-1/2}$. Second, the mesh acts as an impedance on the hydrodynamic flow; equivalently, it effectively prevents collisions within but close to the nozzle from contributing to the forward boost, as these collisions are almost equally likely to come from ahead or behind. Even very transparent meshes can have large effects on flows when the density is high, the velocity is high, and the pressure drop across the mesh is low, but this is not the case in any reasonable beam experiment.

Slit nozzles

The calculations up to this point have been for a circular aperture. The aperture can also be a long, narrow slit, of width r_1 and length r_2; such nozzles generally lead to lower N than is found in a circular aperture of equal area.

For a long, thin nozzle of dimension r_1 and r_2, equation 2.16 becomes

$$\frac{\gamma}{N} = \frac{r_2}{4L(2 + \ln \frac{r_2}{r_1})} \left(\frac{m}{M}\right)^{1/2} \tag{2.18}$$

Roughly speaking, such a slit behaves like an aperture of radius $r_{eff} = (r_1 r_2)^{1/2}$ from the point of view of the dynamics *within* the cell, and like an aperture of radius $r_{eff} \approx r_1$ from the point of view of dynamics *outside* of the cell. This is a step in the right direction, and indeed slit nozzles do show significant improvement compared to round nozzles; however, geometrical constraints - essentially $r_1 < L$ - in general limit these improvements to order of unity.

2.4.6 Two stage geometries

Even with mesh covered apertures and high aspect ratio slits, one stage cells leave the experimenter with a choice between a low flux, slow source or a bright, fast one. This dilemma, and the desire to functionally separate the cell loading side from the beam production side, led us to design a two stage cell, as shown in figure 2.10. The first stage operates as a standard hydrodynamic beam source, with $\gamma \approx 1$, $N \approx 100$; the second stage, with ϕ considerably reduced via vents out the side, operates in or near the diffusive regime, with $\gamma \approx 0.1$ and $N \approx 1$.

Most critically, the production conditions and nozzle conditions can be independently tuned by varying the size of the intermediate aperture. In the experimental realization of this work, the intermediate aperture was a 1 mm wide slit; the length could be adjusted while cold from 0 to 10 mm via a sliding aluminum shutter.

The final system has a theoretical $N = 1$ and net $f = .02$; experimental results suggest $N = 4$ (see figure 2.17) and $f = 0.04$, although absolute measurements of f are unreliable. This unexpectedly high value for f is possibly explained by fortuitous velocity slip between the Yb impurities and the helium gas; this 'velocity slip' is a

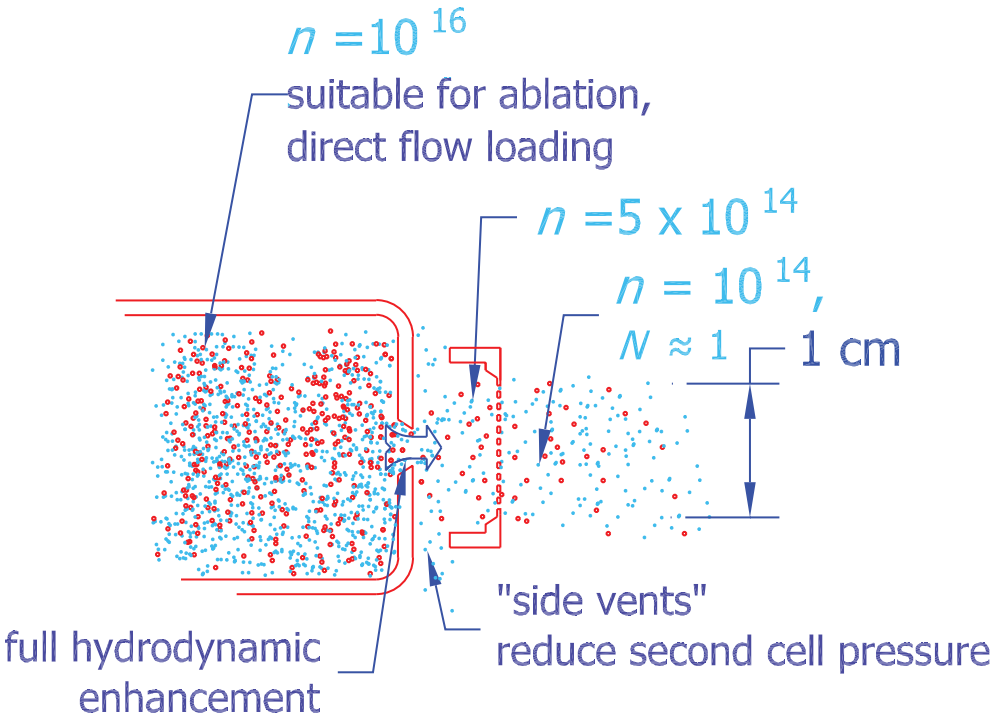

Figure 2.10: A two stage nozzle. The left hand chamber operates as a standard hydrodynamic beam source, with $\gamma \approx 1$, $N \approx 100$, and an assumed f of .5. The right hand side represents an extremely leaky cell - the majority of the flow leaks out the gaps in the side, where it cannot interfere with the forward moving beam. About 25% of the flow enters the second cell, which ends in a large, mesh covered aperture (1.5 cm diameter, 28% transparency). γ for this second cell is considerably lower - on the order of $\gamma = 0.1$ - but the cell is so open that even in the diffusive limit (case 1 in equation 2.9), the efficiency f of the second cell is .05, for a total predicted f of .02.

well known phenomenon in supersonic beams[80], and results in the heavier species' velocity distribution being substantially more forward pointed than the carrier gas. If this is the case, the 'vents' shown in figure 2.10 are releasing pure helium, with almost no Yb entrained in it, although this was not experimentally confirmed.

As an additional advantage, the last surface the gas thermalizes with before being emitted into the beam is the 2nd stage of the nozzle. It is generally straightforward to insulate this stage for the vast majority of the parasitic heat loads in the system,

including the heat loads that are inevitable byproducts of cell loading. This advantage was critical in the guided oxygen work presented in section 3.1, where a small pumped helium pot with a heat budget of a few mWatt was able to cool this stage to 2.6 K, despite a $\approx$ 1 Watt heat load on the main cell, which remained at 6 K or warmer. Extending these techniques to dilution refrigerators, with heat budgets in the 100s of μWatt range, is entirely feasible (see figure 2.25. Loading rates are in general a strong function of power, so this freedom to "abuse" the main cell is a valuable advantage in terms of ϕ as well as T.

Photos of a two stage nozzle are in appendix C.7.

2.4.7 Neon as a buffer gas

Helium vs. neon

In order to achieve the lowest possible temperature, the overwhelming majority of buffer gas cooling experiments to date have used helium as the buffer gas. With a sufficiently high vapor pressure at temperatures as low as 300 mK (for ^{3}He), compared to a lower limit of $\approx$ 12 K for neon, helium is the natural choice when low temperature is the only figure of merit.

Both magnetic and electrostatic traps have depths of at most a few K. It is therefore natural to maximize the flux of molecules with a total energy less than a given energy $E_{trappable} \approx$ 1 K, assumed here to be less than $T_{cell} \approx 4 - 20K$. Somewhat counterintuitively, by this metric an entrained beam using 15 K neon as the buffer gas can substantially outperform a similar beam using 4 K helium. Figure 2.6 shows the simulated forward velocity distribution for such a source using 1.5 K helium, 6

K helium, 15 K neon, and 40 K argon as the buffer gas. It is clear that despite the higher temperature required for a neon or argon beam, there are more cold, low energy atoms in the neon beam than in the 6 K helium beam. Figure 2.5 shows similar velocity distributions for various species entrained in both helium and neon buffer gasses.

Using neon instead of helium as the buffer gas carries several important technical advantages as well. Most notably, neon has a negligible vapor pressure at our cryostat's base temperature of 5 K, meaning that any cold surface becomes a high speed cryopump. The vacuum outside the cell can be maintained at a high level (1×10^{-6} torr in the main chamber, $< 10^{-8}$ torr in a differentially cryopumped "experiment chamber") even with a high flow of order 10^{19} neon atom s^{-1} through the cell. Figure 2.20 shows a realization of such a differentially pumped system, and figure 2.23 shows a proposed version of the nozzle that will significantly reduce dewar background gas, which even with neon has proved to be a pervasive problem in our slow beam work. The higher cell temperature also implies that the cell can tolerate substantially higher heat loads, implicitly leading to higher beam fluxes.

The principle disadvantages of neon are that the higher temperature leads to less rotational cooling in molecules than that available from 4 K (or colder) helium, and that the binding energies of neon to molecules E_{Ne-X} are typically almost 3 times the corresponding energies E_{He-X}, due to largely to neon's larger polarizability[8]. This difference could potentially lead to the unwanted formation of X·Ne complexes, as

[8]The helium binding energy E_{He-X} is also decreased by the larger zero-point vibrational energy of helium due to it's smaller mass. This quantum effect varies with species – it is of course larger for physically small potentials – but can be significant; in some cases, e.g. X=rubidium, a bound He-Rb state is not even supported by the potential.

discussed in section 5.4.

Figures 2.19, 2.21, and 3.8 present data from potassium and ammonia beams that illustrate the potential advantage of neon buffer gas.

2.5 Results

Figure 2.12 shows the optics layout used to characterize our buffer gas beams. The beam flux is measured via absorbtion spectroscopy with a laser passing orthogonally through the atomic beam; this beam can also measure the transverse temperature of the beam via doppler broadening. The forward velocity of the beam is measured in a similar way, via the doppler shifts in the absorbtion spectrum of a beam propagating antiparallel to the atomic beam.

2.5.1 One and two stage nozzles

One stage nozzles

Figure 2.11 shows the measured efficiency of an ablated Yb beam with a simple one stage nozzle for various values of γ. The qualitative agreement with equation 2.9, also shown, is reasonable. Absolute efficiency measurements are difficult to make, as uncertainties in the geometry - in particular, the ytterbium density within the cell - are difficult to eliminate completely; the discrepency in the y axis is therefore probably an experimental artifact.

Figure 2.16 shows the mean forward velocity and relative flux of beams of atomic ytterbium, introduced into the cell via laser ablation. Velocities and fluxes are shown for a representative sample of aperture designs. The basic frustrations predicted in equations 2.14 and 2.15, as well as figure 2.16 are readily apparent - bright, forward boosted beams are easy to make; a beam that is slower and has lower flux can also be produced, but it is difficult to produce a beam that is both bright and slow. The

two stage nozzle (red triangles in figure 2.16) clearly produce the slowest beams.

Figure 2.17 shows the velocity profile from one of these "almost effusive" beams from a two stage nozzle, with a mean forward velocity of 30 m s^{-1}. This corresponds to 9 Kelvin forward energy, with approximately 1 K of spread around this value. Note that this implied cooling is *not* supersonic; it is an artifact of the preferential acceleration of a portion of the velocity distribution. (See figure 2.4.3). The beam is measurably non-effusive; comparison with a simulated "almost effusive" velocity distribution suggests that $N \approx 4$.

2.5.2 Heating from ablation

The role of heating from ablation - ignored in the analysis of this chapter, and all too often ignored in buffer gas loading experiments in general - is troublesome in these experiments. Our traditional doppler thermometry is rather slow, limited to < 400 Hz by the scan rate of our diode lasers. In the past this has prevented us from resolving dynamics in the first 1-2 msec after an ablation pulse. The time of flight "thermometry" shown in figure 2.15 strongly suggests that even ablation pulse powers of 2 mJ, which we would generally consider very low, have a dramatic effect on cell dynamics.

It is difficult to deconvolve this effect from others in beam dynamics, but it is in fact plausible that this is a major reason why two stage nozzles seem to work. As discussed in section 2.4.6, it appears to be the temperature of the *second* stage in a two stage nozzle that determines the final beam $v_{forward}$ and T. The second stage is largely shielded from the ablation pulse, and the long mean free path in this stage

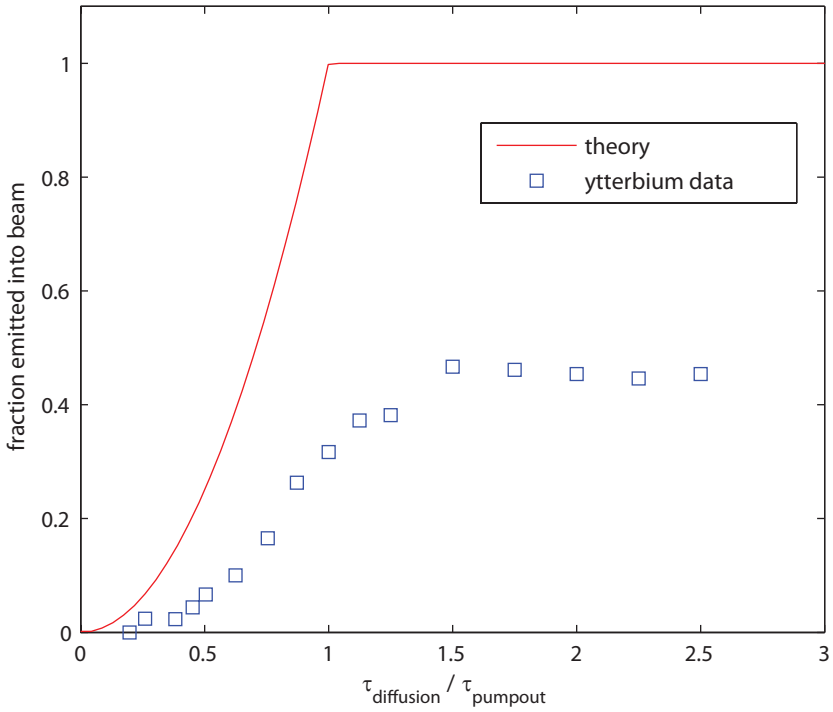

Figure 2.11: The measured efficiency f for a single stage aperture for various values of γ. At high buffer gas densities, which correspond to long diffusion times and therefore high $\gamma \equiv \tau_{diffusion}/\tau_{pumpout}$, up to 40% of the cold ablated atoms are detected in the beam. The peak instantaneous flux represented here is 5×10^{15} atom s^{-1} sr^{-1}. Equation 2.9 is shown in red for comparison. The mesh used in our experiments is photo-etched 130 μm thick 316 stainless steel or copper, has a transparency $f = .28$, 136 μm diameter holes, and is manufactured by tech-etch.

allows for very rapid thermalization with the stage walls. This picture is not, however, entirely consistent - spectra taken inside the cell 10 msec after the pulse show a *cold*, not hot, first stage buffer gas temperature, and our group has for many years been working with cold, ablated samples, produced with much more than 2 mJ per pulse. For now this remains merely a source of concern - and a motivation to move away from ablation based sources.

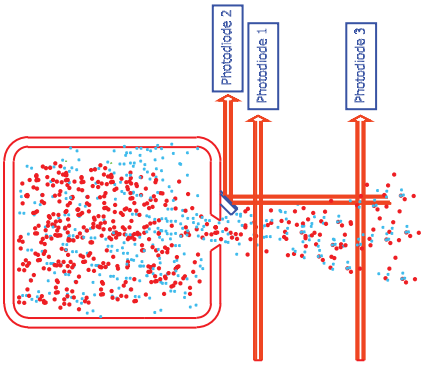

Figure 2.12: Laser configuration for characterizing buffer gas beams. Beam flux is measured via absorbtion spectroscopy on photodiode 1. The beam axial velocity distribution can be measured two ways: the default method is by measuring doppler shifts on the axial beam (photodiode 2); data taken with this method is shown in figure 2.13. An alternative is to measure the time of flight difference between when a pulsed atomic beam crosses the lasers 1 and 3. Data taken using this method is shown in figure 2.14.

2.5.3 Direct flow loading into beams

The data shown thus far in this chapter is from buffer gas beams loaded via ablation, a fundamentally *pulsed* source. Figure 2.19 shows the transverse and axial velocity distribution of a continuous, neon-cooled buffer gas mediated beam of cold potassium. This beam is loaded by directly flowing a mixture of potassium and neon from a hot oven to the cold (15 K) cell. The brightest beams produced with this technique had a *peak* flux 50 times higher and an *mean* flux 1000 times higher than the ablated rubidium beams shown in figure 2.13.

The apparatus is shown in figure 2.18; for more details of this loading method, see chapters 4 and 5. This demonstration, and reference [77] in general, provides the "missing link" between the general, high flux direct flow loading and the beam based experiments proposed in chapter 6.

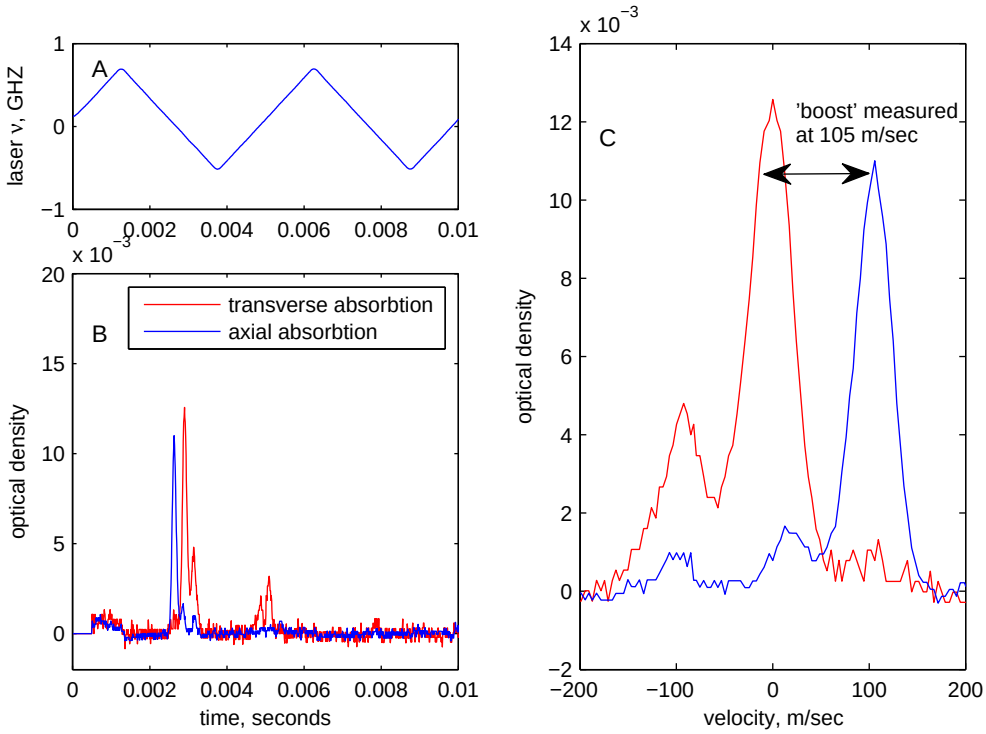

Figure 2.13: Typical raw data for a buffer gas beam characterization (doppler method). (A) Laser frequency as a function of time; the ablation pulse takes place at t = 0. (B) The transverse and axial absorbtion as a function of time; the geometry of these beams is shown in figure 2.12. The first 5 $\times 10^{-4}$ seconds are corrupted by the pulsed laser, and are zeroed in this plot. (C) The spectra shown in (B), converted to velocity units = $c\frac{\Delta\omega}{\omega}$. The frequency shift between the red trace, from a laser that propagates orthoganally to the atomic beam, and the blue trace, from an axial laser, represents the forward velocity of the beam. This data is taken on the ^{85}Rb D_2 line, F = 3, F' = 2,3,4. The cell was loaded via ablation of a solid RbCl precursor

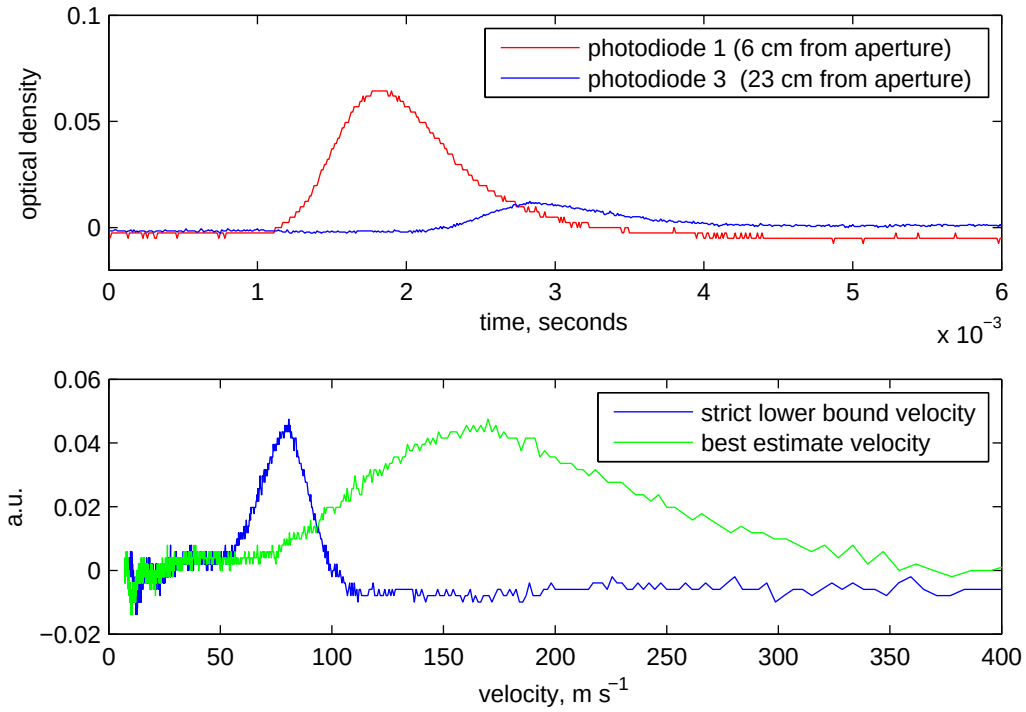

Figure 2.14: Typical raw data for a buffer gas beam characterization (time of flight method). Upper plot: absorbtion on the near (red trace) and far (blue trace) laser as a function of time. Lower plot: The far trace converted into a velocity distribution. Interpretation of this trace is ambiguous, because the arrival time of an atom is a function both of it's velocity and of it's departure time from the cell; this 'departure delay' makes a non-negligible contribution to the time profile. The green trace is a 'best estimate' velocity profile based on the time of the peak in the near (red trace) beam; the blue trace is an absolute lower bound of the velocity profile, where it is assumed, inaccurately, that every atom leaves the cell immediately at t=0. This data was taken with an ablation loaded beam of ytterbium.

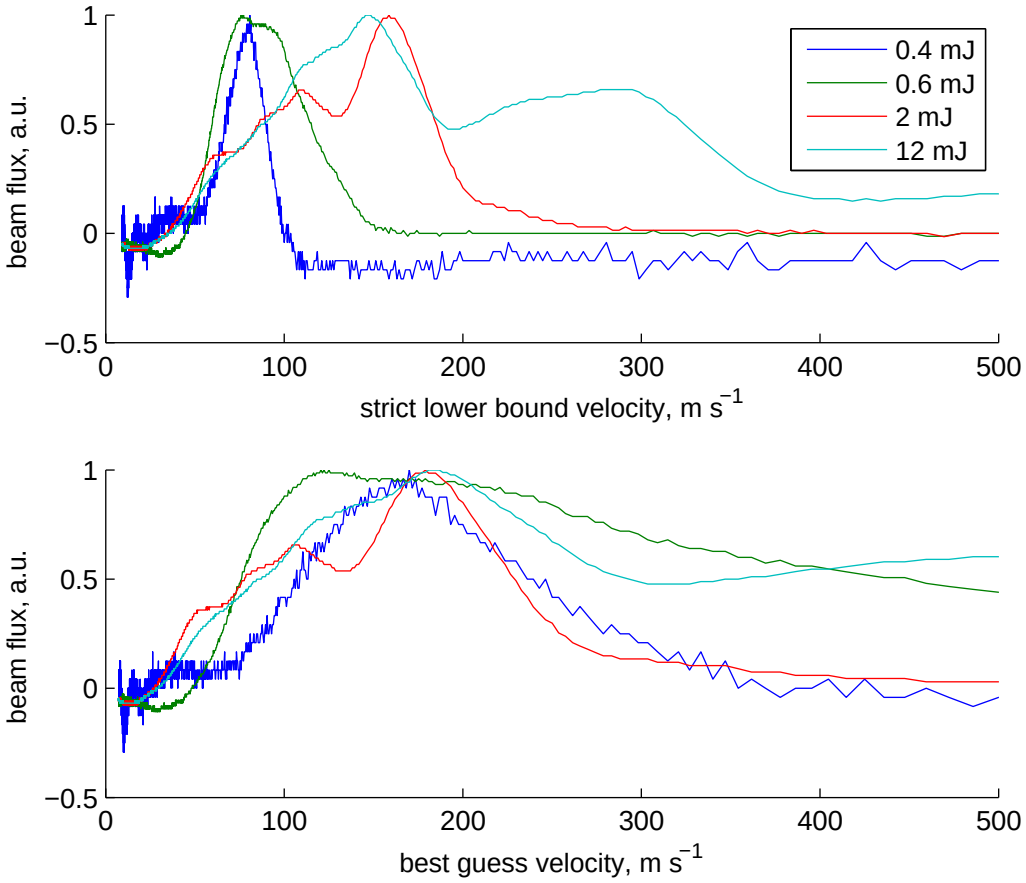

Figure 2.15: Time of flight velocity profiles for ytterbium ablated with various laser pulse energies. The upper plot shows the absolute lower bound velocity profile for each power; the lower plot shows the 'best estimate' profile, although at high energies these profiles are highly suspect. It is clear that even rather modest 2 mJ pulse energies dramatically heat the buffer gas.

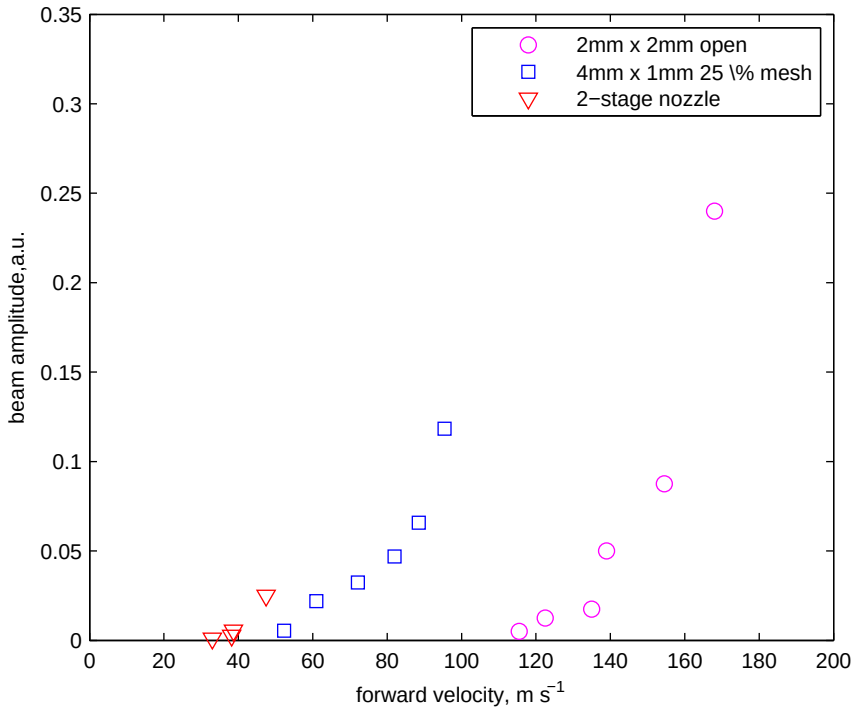

Figure 2.16: The mean axial velocity (referred to as the 'velocity boost' in the text) and the overall flux for a ytterbium beam produced in an open 2 mm diameter aperture, a 4mm x 1mm slit covered in 25% transparent mesh, and a two-stage nozzle, as described in section 2.4.6. Direct comparison between the beam fluxes should be viewed with some skepticism, due to uncontrolled variations in ablation yield and laser alignment. Nevertheless, it is clear that the two stage nozzle yields a much slower beam than a one stage equivalent.

Cryogenic jet-cooled beams

At very high flow rates and buffer gas densities, it is expected that there will be enough collisions for the gas to cool as it expands into the vacuum. Figure 2.21 shows axial and transverse velocity distributions for a boosted beam of potassium entrained in a high flow of neon buffer gas (aperture 1 mm x 3mm open slit, 50 sccm neon flow, T_{cell} 14 K). This beam was measured inside a differentially cryopumped "cold box" as shown in figure 2.20.

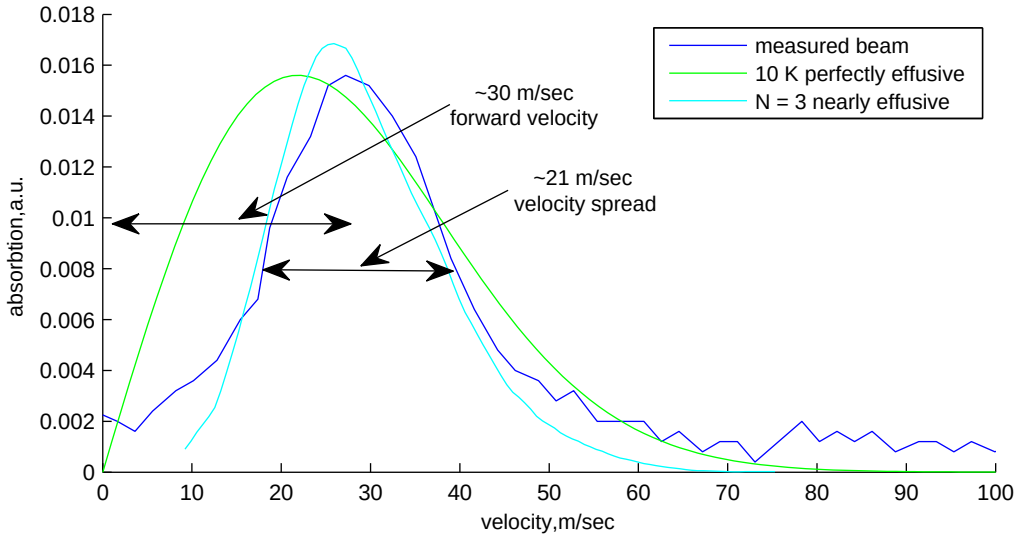

Figure 2.17: The spectrum of the ytterbium beam produced in a two stage nozzle, as described in section 2.4.6. The simulated velocity distribution of a 10 K perfectly effusive source and an 'almost effusive' source with $N = 3$ is shown for comparison.

Both the transverse and longitudinal velocity distributions measured in figure 2.21 are substantially colder than 14 K. The transverse temperature is set by the collimating slits on the input side of the cold box, but the longitudinal temperature is strongly suggestive of significant supersonic cooling. In additional experiments with similar high flux neon-mediated beams of ThO[107], we have also seen evidence of significant rotational cooling.

This continuous beam represents an attractive alternative to many experiments working with supersonic beams sources, simply because it has a modest forward velocity of $v_{forward} = 160$ m s^{-1} is significantly lower than the ≈ 330 m s^{-1} of

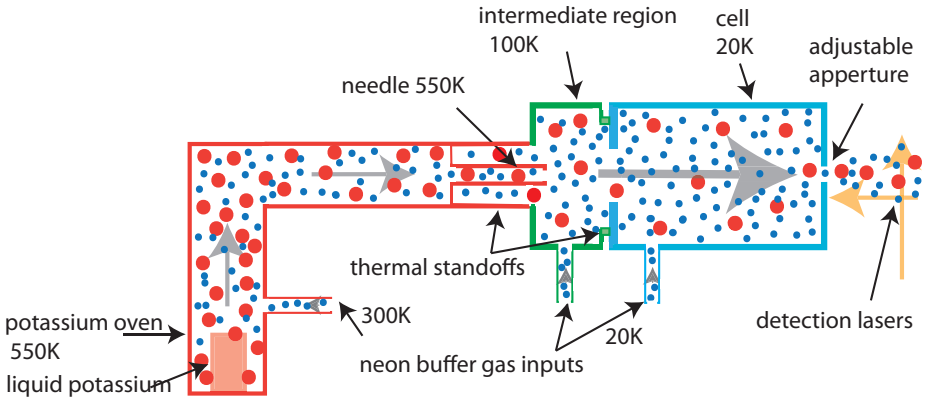

Figure 2.18: Overview of the bright, continuous potassium source apparatus. An oven supplies a hot (550K) mixture of potassium and neon that flows through an intermediate region (100K) to a cold tube "cell" (15K). The oven, intermediate plate, and cell are separated by thermal standoffs to reduce heat loads. A cold beam of potassium and neon exits an adjustable aperture on the far side of the cell where its characteristics are measured by absorption spectroscopy.

traditional supersonic sources. For example, such a source could be decellerated to rest by a stark decellerator with 1/4 as many stages as the one required for a room temperature supersonic source.

Traditional room temperature supersonic sources have stagnation densities of 4×10^{19} cm^{-3} or even higher[65]. Even at our highest flow rates of 50 sccm, our cell densities ($n \approx 4\phi/A\bar{v} = 2 \times 10^{17}$ cm^{-3}) are significantly lower than this. It makes more sense, however, to compare our densities with the point in the supersonic jet *when it has cooled to* $\approx$ *14 K*. Simulations of supersonic jets, similar to those presented in figure 5.7, suggest that the density at this point for typical jets is $\approx 2 \times 10^{18}$ cm^{-3}, still an order of magnitude above our density.

This discrepancy is partially explained by the fact that our jets are expanding more slowly than traditional 300 K jets. This is mostly a consequence of our lower forward velocity. The expansion rate $\frac{\dot{n}}{n} = \frac{\bar{v}}{r}$; in order to maintain adiabaticity the

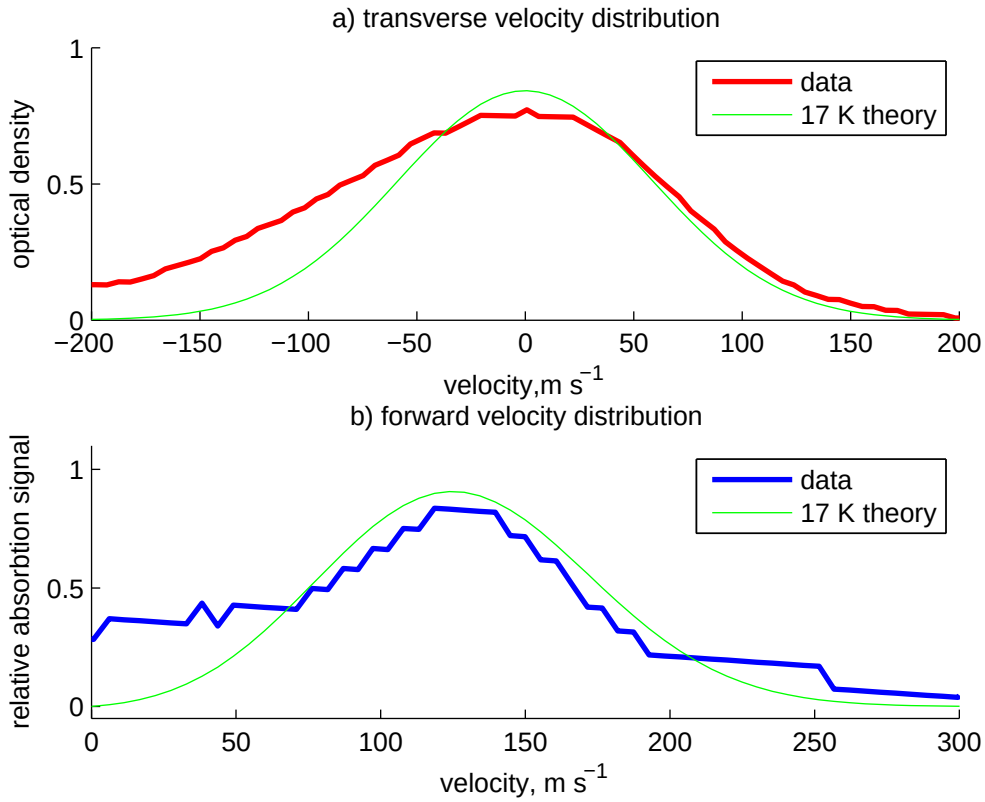

Figure 2.19: Measured transverse [a] and forward [b] velocity distribution of a high flux, continuous beam of potassium, with 17 K neon used as the buffer gas. The apparatus used for this work is shown in figure 2.18. This beam is optimized for high flux, rather than low forward velocity; it corresponds to the 'entrained' regime discussed in section 2.4.2 and the blue curve in figure 2.4a. The green curves represent the expected distribution from a entrained beam with $T_{gas} = 17$ K. The amplitude is the only free parameter in these fits. The left side of each plot is somewhat distorted by the nearby $F = 0$ hyperfine line. This data represents a continuous beam with a potassium flux of 1×10^{15} atoms / second; we have observed fluxes as high as 1×10^{16} atoms / second, but they are not shown here because the high optical density (≈ 8) makes their interpretation less straightforward.

collision rate must be substantially higher than this. r is comparable in the two systems; traditional jets with a 200 μ nozzle hit 10 K at about $r = 2$ mm; our jets hit 10 K almost immediately at $r = r_{nozzle} \approx 2$ mm. This requirement on adiabaticity suggests another (to date unexplored) advantage of cryogenic beams - their slow

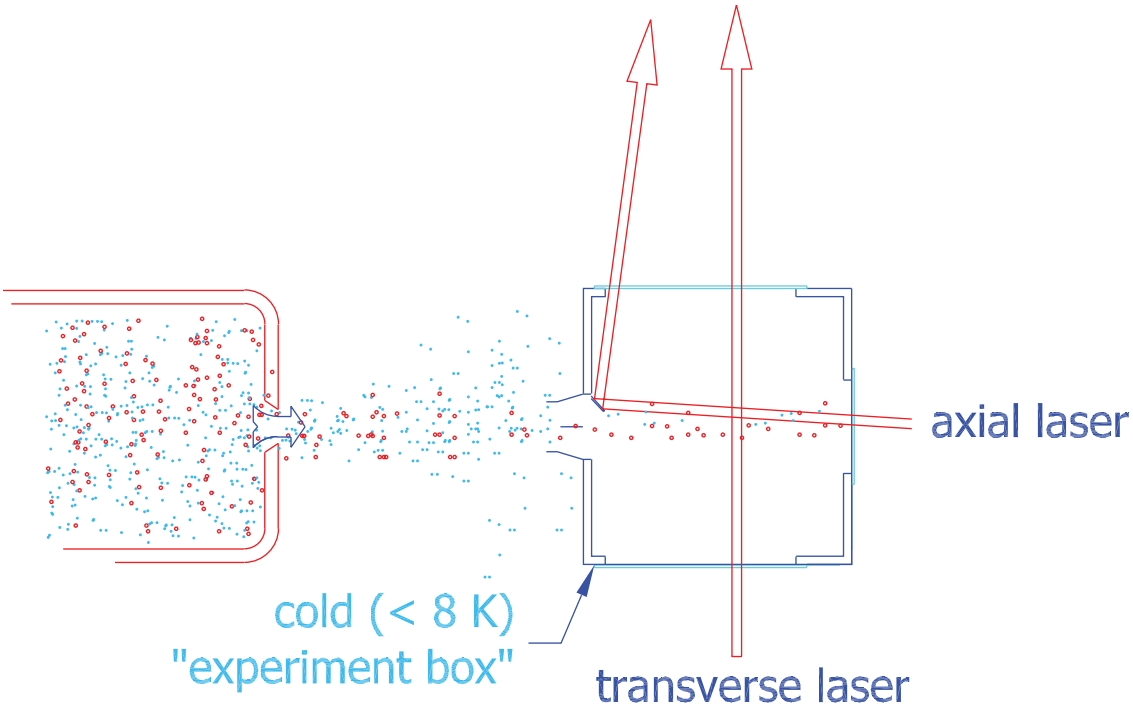

Figure 2.20: Cryogenic layout for characterizing cyrogenic jet cooled beams. The cold copper "experiment box" had no surfaces within it warmer than $\sim$ 8 K; this ensures an extremely low neon vapor pressure. Further differential pumping within such a box can be done with simple mechanical partitions. In future experiments, simple shutters could be used to rapidly close off this differentially pumped chamber, which we believe will rapidly achieve an extremely high vacuum. There is no helium introduced anywhere in this system. A photo of the dewar showing a realization of this differential pumping is in appendix C.1

forward velocity means they expand slowly, so they need less gas density to satisfy $\gamma_{collision} > \frac{\dot{n}}{n}$. This implies they will cool further than 300 K sources under identical gas loads.

We have observed the effect only with neon buffer gas, but this is probably technical. Our increased cryopumping speeds with neon allow us to run at about 20 times higher fluxes of neon than helium, and it is only in this high flow ($>$ 20 sccm) regime that supersonic cooling is observed. The differential pumping suggested in section

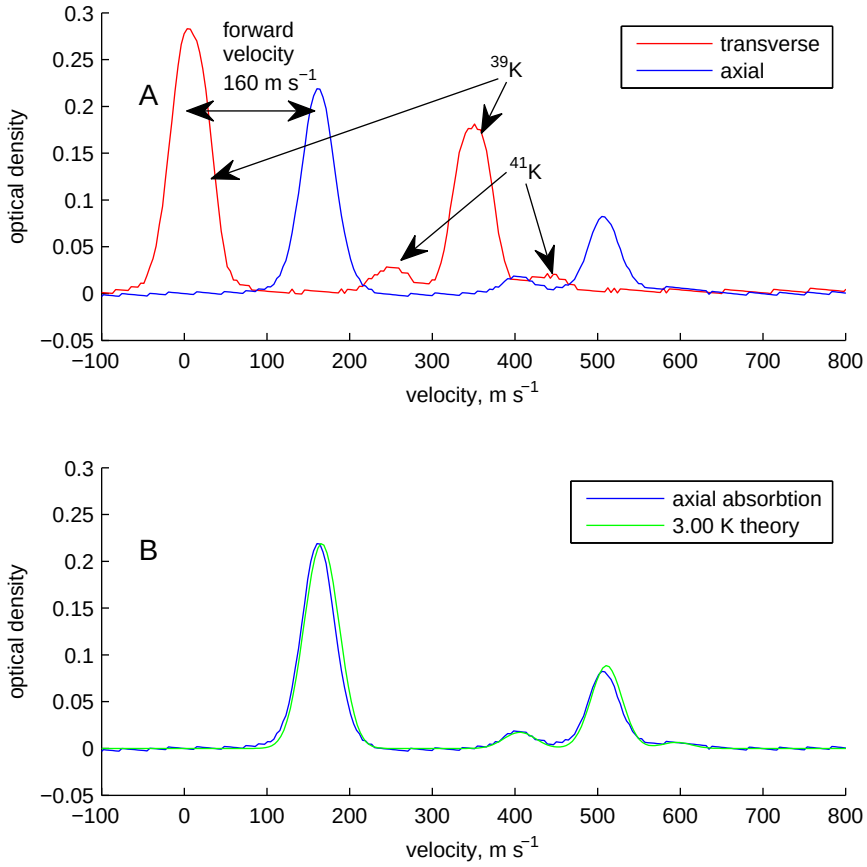

Figure 2.21: Transverse and longitudinal velocity distributions for a supersonically cooled beam of potassium entrained in neon. (A) The transverse (red) and longitudinal (blue) absorbtion spectrum. The x axis is shown in doppler shifted "velocity units" of $c\Delta\omega/\omega$. This data was taken with on the potassium D2 line at 766.7 nm; peaks from both ^{39}K and ^{41}K are visible. The upper state hyperfine structure is not resolved. (B) The longitudinal velocity distribution with an excellent fit to 3.0 K theory. This beam was produced with a cell temperature of 14 K; the coldest point in the cryostat was $\approx$ 8 K.

2.23 would allow us to access this regime with helium as well as neon buffer gas, and at correspondingly lower starting temperatures.

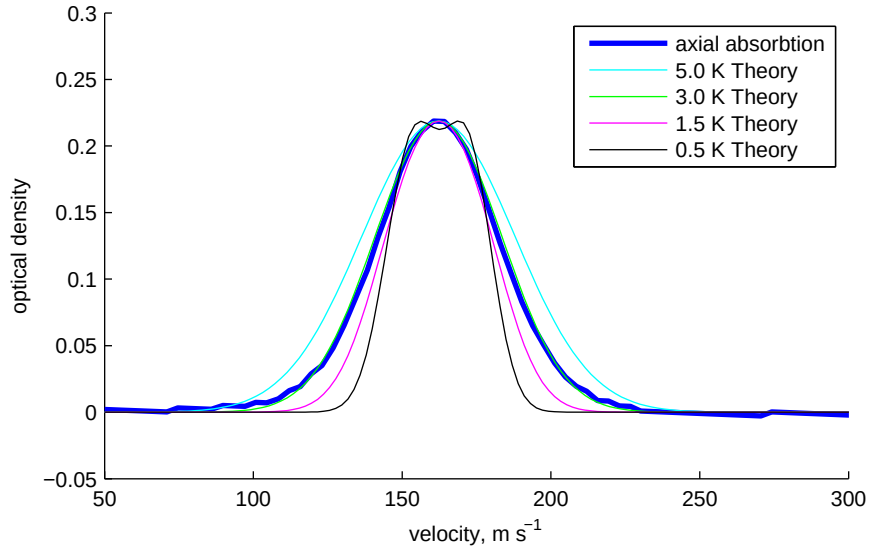

Figure 2.22: The ^{39}F = 2→F' line (the large left hand peak) from figure 2.21B. Theoretical doppler-broadened spectra for several temperatures are shown. The upper hyperfine structure is not resolved; care must be taken in such cases that measured linewidths represent doppler broadening, rather than artificial widths from several partially resolved lines. The coldest theory, at 0.5 K, resolves the F′ = 3 upper state, and it is clear that the spectrum is inconsistent with both 5 K and and 1.5 K fits.

2.6 Future improvements

Figure 2.23 shows a modification to the two stage nozzle design to significantly reduce the background gas load on the dewar. This is especially important when using direct flow loading (see section 4.2), which generally requires a high buffer gas flux to efficiently transport species A into the cell. In several cases this limit has prevented us from using helium as a buffer gas in direct flow loading experiments; the design proposed in section 2.23 should lift this constraint.

Figure 2.24 shows a proposal for modified two stage nozzle with the second stage attached to a dilution refrigerator; this is a direct extrapolation from the "1 K pot" cooled cell demonstrated in section 3.1. A "warm cell", assumed to be at 4 K, is

loaded with a mixture of species A and ^{4}He buffer gas[9]. Cooling this gas to 0 K places a heat load of $\frac{3}{2}\dot{N}k_bT$, or 350 μWatt; this would imply a base temperature of a dilution refrigerator of < 200 mK. In fact the base temperature would be limited by the ^{4}He vapor pressure curve, but it is notable that the density in the second cell is a low 10^{15} cm^{-3}; the base temperature would probably be about 500 mK. At this temperature, the dilution unit could be replaced by a much cheaper and simpler closed ^{3}He refrigerator of approximately equal cooling power, as is used in [21].

At $T = 500$ mK, the mean velocity of an entrained beam of species A is ~ 46 m s^{-1}; this corresponds to an energy of $\sim 0.5M/m$. Simulated outputs of these beams are shown in figure 2.25.

[9]In principle ^{3}He is also a possibility, but efficient and faultless recycling is a requirement; even a "low flow" design at 10 sccm costs \$10 / minute at current ^{3}He prices

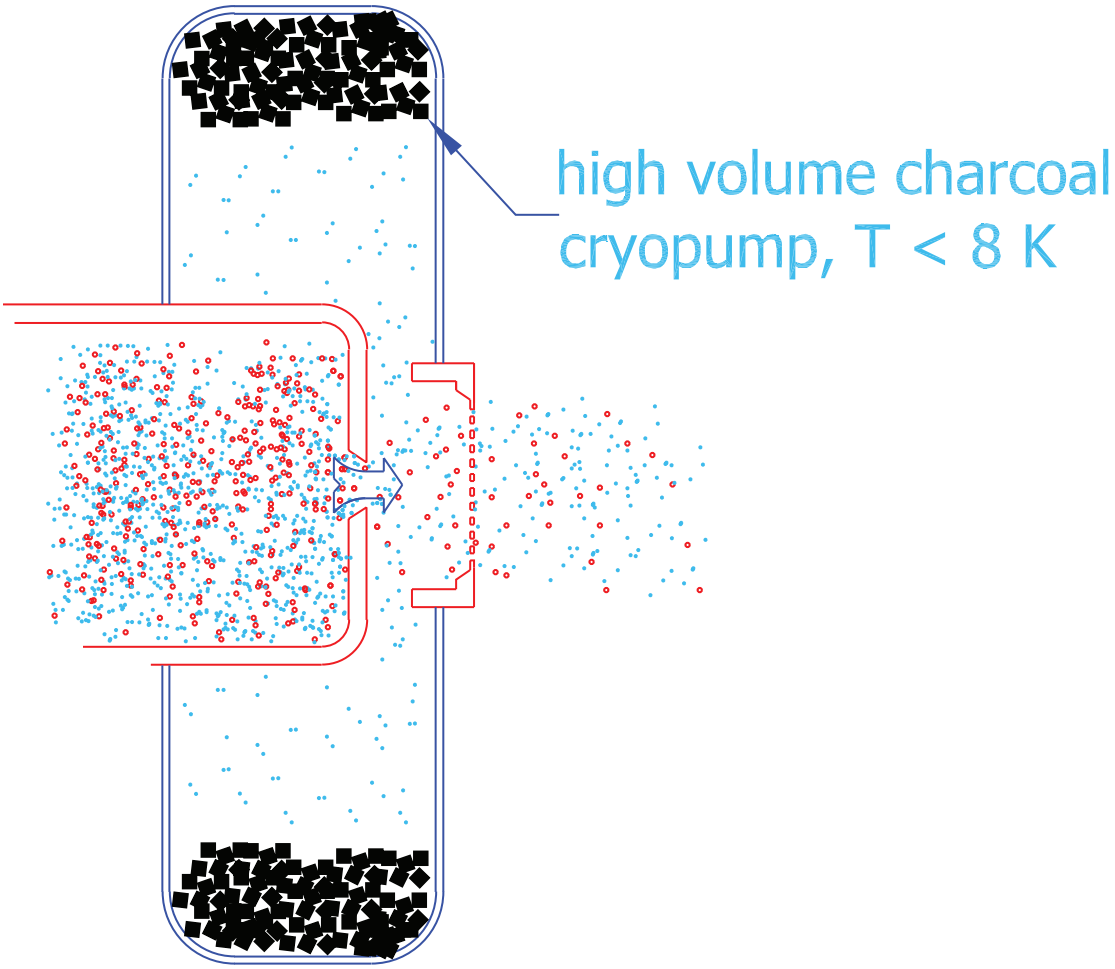

Figure 2.23: A proposed improvement of the two stage nozzle of figure 2.10. High volume cryopumps capture the majority of the helium buffer gas that spills out the "vents", preventing it from contaminating the general dewar vacuum. This is particularly important when combining this nozzle with very high flows of buffer gas, as is required by direct flow loading (section 4.2). The vacuum in the "gills" would not have to be very good by trapping standards, as long as it is low enough to not impede flow into the vents on the sides nozzle second stage.

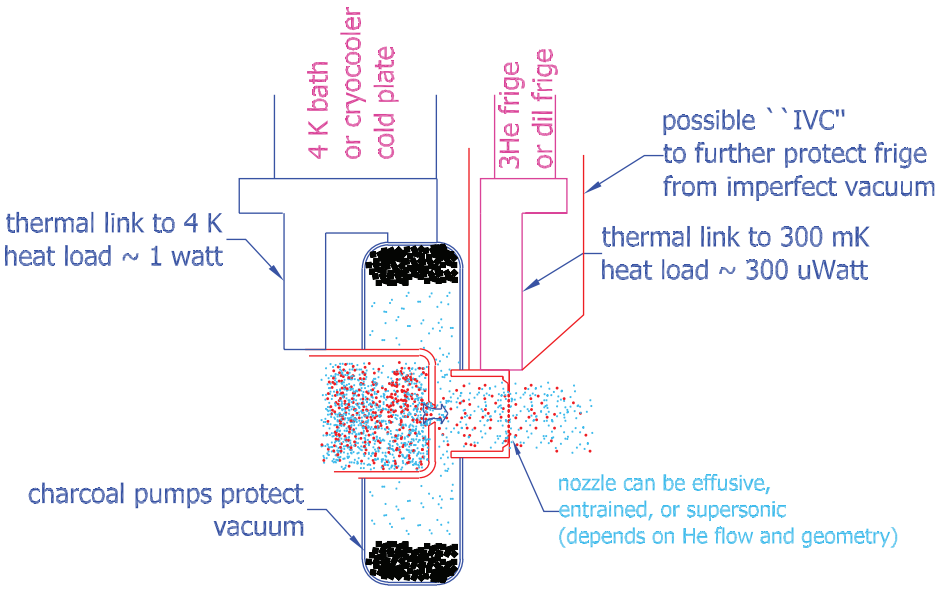

Figure 2.24: A proposed improvement of the two-stage nozzle taking full advantage of the fact that the beam temperature depends only on the temperature is the final stage, which can be exposed to very low heat loads. This is a natural extension of the approach taken with the guided oxygen work in chapter 3. Although the two-stage nozzles described in this chapter were largely effusive sources, this geometry would provide a high flux, slow beam in any of the regimes described in section 2.4. Temperatures as low as 1 K could be acheived very economically if the frige unit were replaced by a well-designed 1K pot with appropriate thermal protection.

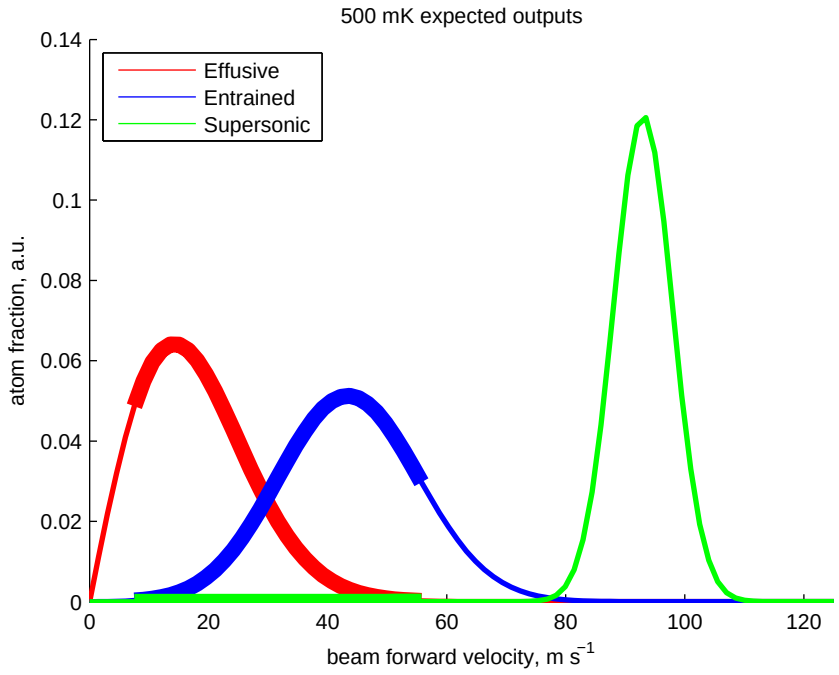

Figure 2.25: Simulated forward velocity distributions for buffer gas beams in various regimes assuming a cell temperature of 500 mK; for this simulation a species A with ($M = 20$) is used. Forward velocity distributions for effusive, entrained, and supersonic beams are shown. The bold lines represent the "trappable" portion between 1 and 4 K.

Chapter 3

Guided beams

The beams of ytterbium and rubidium described in section 2.5.1 consist almost entirely of cold buffer gas, containing only a small fraction (typically $< 10^{-4}$) of the species of interest. This is not a problem for many precision spectroscopy experiments, where the buffer gas remains a spectroscopically invisible partner, but both trap loading experiments and collisional studies cannot use such beams: 'uninteresting' collisions with the background gas in the beam dominate the collision dynamics, and lead to rapid trap loss in the case of trapping experiments. It is therefore desirable to separate the species of interest from the background gas.

This separation is especially important when there is a significant velocity slip between the species of interest and the buffer gas; this generally occurs in effusive sources with $M > m_{He}$. The slowest molecules in these beams can be scattered to faster velocities by buffer gas atoms even rather far from the nozzle; in the case of a guided beam, these late collisions can knock slow, guided molecules out of the guide. Separation of such beams is extremely similar to the velocity filtered cold molecule

sources discussed in section 2.2[83], and is plagued by the same problems when the very coldest molecules are desired.

Separation is generally achieved by manipulating the species of interest with an external field; the inert buffer gas does not interact with the field. Electric, magnetic, and optical forces have been used for this purpose; in general the field to be used is dictated by the properties of the species being studied.

In the ideal case a beam guide can be constructed, efficiently transporting the beam, perhaps through several stages of differential pumping, to an ultra-high vacuum 'experiment region'. Beam guides have been demonstrated for low field seeking paramagnetic atoms and molecules [71], [78], [83], low field seeking polar molecules [10], and high field seeking polar molecules[12]. Off resonant optical forces have also been used to manipulate[25][74] and guide[58] atomic beams, but the strength of the interaction in general limits this technique to applications where the temperature of the species is in the mK range or below.[1] A beam guide is not strictly necessary; any field configuration which deflects the beam will suffice, although without a guide the density in the beam will rapidly decrease as the beam diverges. For more discussion of non-guiding beam separators see section 6.4.2.

In addition to providing a clean, buffer-gas free beam, the beam guide/deflector will in general act as a state selector, passing only the subset of atoms or molecules that enter the guide with the appropriate orientation with respect to the applied field.

---

[1] An exception is pulsed optical fields; due to the very high electric field in these pulses, even barely polarizable atoms can be enormously deflected by pulsed lasers, with potential depths as high as several hundred K[40]. The major drawback of this powerful and almost universal technique - it can be applied even to nobel gas atoms - is the small physical and temporal size of the pulse, which as a result typically overlaps very poorly with the phase space occupied by the molecular beam

If the guide/deflector can be rapidly switched on and off (this is the case for all the techniques described above with the exception of magnetic guides), timing of this switching can provide accurate velocity selection as well; see for example section 3.2. The combined beam/guide system can therefore provide a clean, cold, switchable, continuous, state selected, and velocity selected atomic or molecular beam - the ideal input stage for collisional studies or trap loading experiments.

The state selection would be particularly useful in a hypothetical collision experiment looking for inelastic, state-changing collisions; since there is generally a class of states that is not present in the guided beam, careful detection of molecules in those states can reveal molecules which underwent inelastic collisions, either with other gas phase molecules, or with a physical surface. Since most spectroscopic detection methods can thoroughly discriminate between the relevant states, the background, and hence the noise, in such experiments would typically be very low.

3.1 Guided O_2

The two stage nozzle described in section 2.10 was used to realize a high flux, hydrodynamically enhanced source of cold O_2.[76]. This source was used to load a magnetic guide, producing a guided beam of cold O_2 with a continuous flux of 3×10^{12} molecule s^{-1} into a room-temperature high-vacuum region. This flux compares favorably to cold *atom* sources and far exceeds previous demonstrated fluxes of cold molecules.

We chose to guide O_2 because it is relatively easy to introduce into our cold cell and has a high magnetic moment of 2 μ_b. Because the O_2 is cooled in a low magnetic

field, it is expected that the molecules occupy a uniform statistical mixture of Zeeman states. Thus, $\approx 1/9$ of the molecules exiting the aperture are in the maximally guided $N = 1$, $J = 2$, $m_J = 2$ state, where N is the rotational quantum number, J is the total angular momentum quantum number, and m_J is its projection on the axis defined by the magnetic field. We estimate that the contribution to guided beam flux from other states is small ($< 10\%$).

3.1.1 Apparatus

The heart of the experimental apparatus is a ≈ 2.5 cm size cell anchored to the cold plate of a cryostat. This cell is a copper box with two fill lines (one for helium and one for oxygen) on one side and an aperture on the opposite side. To produce beams of O_2 we flow He and O_2 continuously into the cell, where they mix and thermalize to the temperature of the cell. The He does not freeze to the walls of the cell but any O_2 molecule that touches the wall does; the O_2 cools by thermalizing with the helium. The helium and a fraction of the O_2 escape through a double-stage aperture as described in section 2.10. The balance of the O_2 remains frozen on the cell walls. The apparatus is shown in figure 3.1, and a typical raw data set from the RGA is shown in figure 4.3.

In more detail, the copper cell is $2.5 \times 2.5 \times 2.5$ cm ($V \approx 15$ cm^3) and its temperature is varied between $T = 2.6$ K - 25 K. It is surrounded by (dewar) vacuum, heat shields and optical windows 3.1. Cooling of the cell is done with a pulsed tube refrigerator and a small pumped liquid helium reservoir (used to achieve temperatures below 4 K). The copper helium gas fill line to the cell is thermally anchored to a 1.3

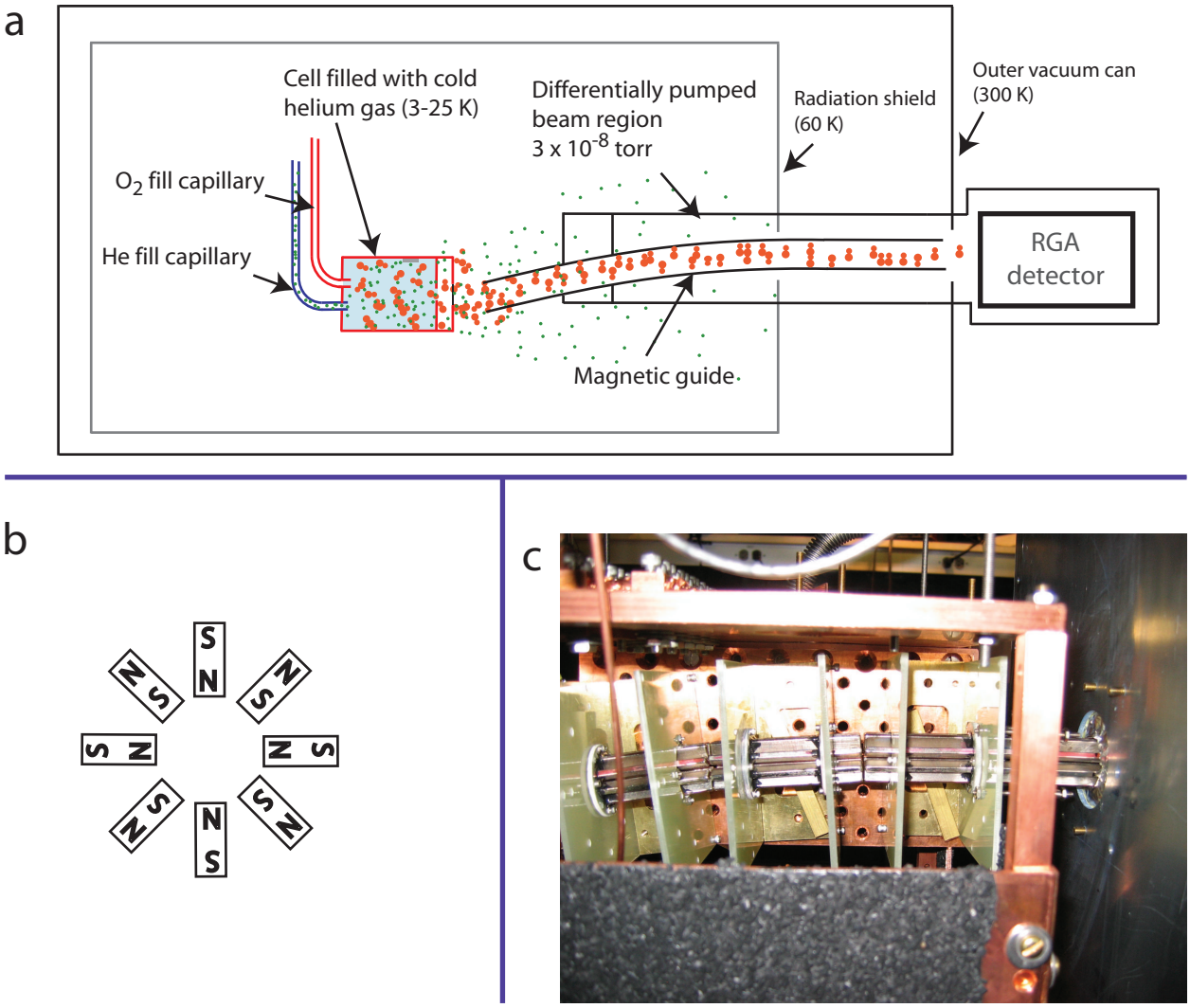

Figure 3.1: Guided oxygen experimental apparatus. Hot ($\approx$ 100K) O_2 molecules thermalize with helium gas in a cold (3-25K) copper cell. The mixture then sprays through the slit aperture and enters a beam guide. Cold, low field seeking molecules are guided into an RGA detector.

K cold plate a few centimeters before it enters the cell. The O_2 fill line is held at 100 K, above the freezing point of oxygen. A short stainless steel sleeve thermally disconnects the relatively warm O_2 line from the cell; a photo is shown in figure C.8. Since this work was published, significant improvements of this injector design have

been made by Buuren et. al.[101] Helium is typically flowed into the cell at 1×10^{17}-8×10^{18} atom s^{-1} and O_2 is flowed into the cell at similar rates, typically 1×10^{17}-3×10^{18} molecule s^{-1}.

Despite the large helium gas flow, the beam region vacuum is maintained at a low 3×10^{-8} torr by two stages of differential pumping with high speed cryopumps made of activated charcoal ($T = 6.5$K, 2000 cm^2 total apparent area).

A 30 cm long magnetic guide is located with the guide entrance 1 cm from the aperture. The guide is constructed from an array of permanent NdFeB magnets (each magnet 0.3 cm $\times$ 0.6 cm $\times$ 7.5 cm). The magnets are arranged in a linear octopole, such that low field seeking molecules are confined to the center of the guide. The far end of the guide (the "guide exit") is not at cryogenic temperatures, but rather deposits the guided molecules into a room temperature residual gas analyzer (RGA). The guide has an inner diameter of 0.9 cm and 5000 G depth, equivalent to 680 mK for O_2 in its most magnetic guidable state. The guide undergoes a single bend with radius of curvature $r = 20$ cm.[2] This bend ensures that only guided molecules can pass; i.e. O_2 must be moving slower than 7000 cm s^{-1} (9 K equivalent temperature) to be guided around the bend. Any helium which enters the guide will be rapidly pumped out through the slots between the magnets ($\approx$ 40 % total open area). The entire system imposes a heat load of $\approx$ 1 watt on the 4 K pulsed-tube refrigerator.

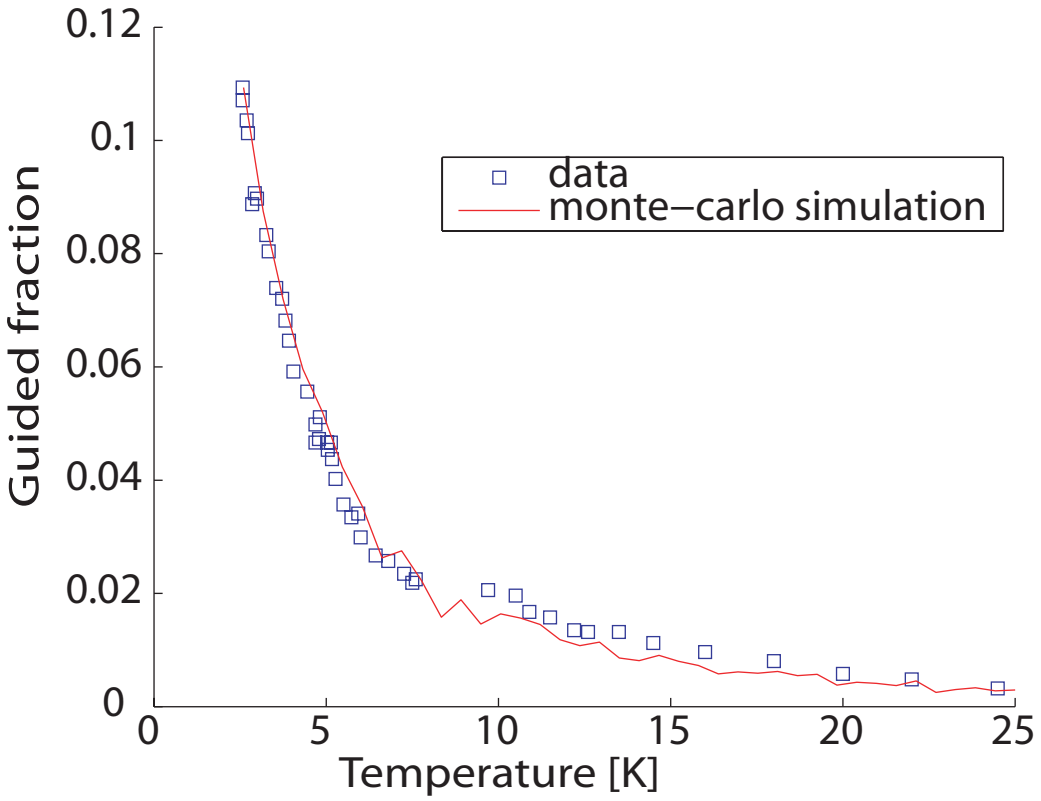

Figure 3.2: Guided flux of O_2 as a function of cell temperature. The temperature dependence of the measured flux is in excellent agreement with the Monte-Carlo simulation (solid line). The vertical axis represents the absolute guided fraction (the ratio of the number of guided O_2 molecules to the number exiting the source) as calculated by the simulation. The only free parameter in this fit is the absolute scale. In order to run for extended periods of time while avoiding plugging the aperture, this data was taken with oxygen input (0.5 sccm) and helium input (0.4 sccm) about one order of magnitude lower than that used to demonstrate our peak flux of 3×10^{12} O_2 s^{-1}. The highest flux shown here represents 2.5×10^{11} O_2 s^{-1}

3.1.2 Results

The molecule source and guide were characterized by varying the O_2 flow, helium flow, and cell temperature, while always monitoring the output flux of O_2. Fig. 3.2

[2]To be more precise, the guide is not bent, but is made up from a number of short (2 cm) straight segments. Simulations show that the small (¡ 1 mm) gaps between these segments necessary to produce a "bend" lead to insignificant loss.

shows our guided flux for a range of temperatures. Because the depth of the guide (680 mK) is less than the temperature of the source over the entire range of temperatures used, a colder source always leads to a higher flux of guided molecules. A Monte-Carlo simulation of our guide is plotted with the data. Agreement is excellent, showing not only that we are guiding molecules but that the details of the system are well understood.

Our maximum measured guided flux of 3×10^{12} O_2 s^{-1} is achieved by simultaneously flowing 10 sccm of O_2 and 2 sccm of helium into the cell (sccm is standard atmosphere-cc per minute). The system can operate at this peak flux for about 100 seconds before the aperture becomes plugged with oxygen ice.

We note that we are confident that the O_2 in our guide is cold rotationally as well as translationally. In all our previous work with buffer gas cooling and in many supersonic beam experiments it has been observed that rotational thermalization rates are comparable or faster than elastic scattering rates[109, 53].

3.2 Guided ND_3

Although the guided molecular oxygen source described above was cold, state selected, and slow, the system described in section 3.1 was inconvenient for quantitative analysis of the guided beam. In particular, the permanent magnetic guide could not be switched on and off, so the velocity distribution in the beam could not be directly measured. This limitation, along with the difficulties posed by the lack of laser-accessible transitions in molecular O_2, led us to construct an electrostatically guided beam source for polar molecules.

3.2.1 Why ND_3?

ND_3 had been previously guided[83][102] and trapped[85] in both low field seeking[9] and high field seeking[104] traps. The small inversion splitting of deuterated ammonia means that it can be completely polarized in fields as low as 5 kV/cm, which are easily produced and switched in the laboratory. ND_3 is a gas at room temperature, which makes direct injection loading of the cell (see section 4.1.2) straightforward. The stark shifts of the rotational ground state inversion manifold of ND_3 are shown in figure 3.3

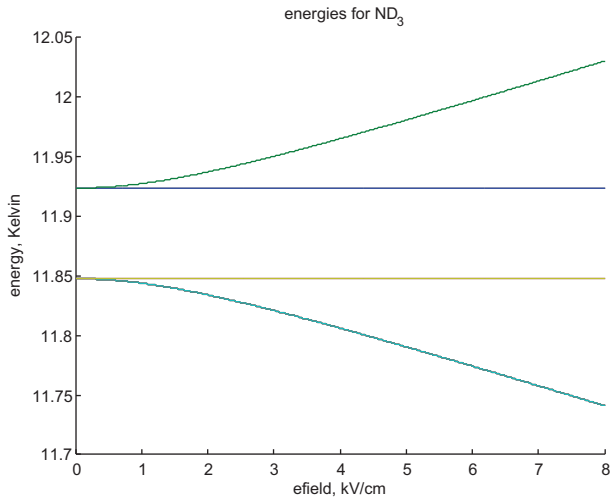

Figure 3.3: Energy of the J=1,K=1 inversion doublet of ND_3. This manifold represents the rotational ground state of para-ammonia; only the highest state shown here (light green) is guided in by our low field seeking guide.

3.2.2 ND_3 apparatus

The cell and nozzle for our guided ND_3 work is similar to the one discussed in section 3.1. The ND_3 is fed directly into the cell via a capillary at $T = 280$ K. Cold

ND_3 molecules exit the cell and after a short gap of 30 mm, enter an electrostatic guide.

Ammonia has no single photon transitions with reasonable (> 160 nm) wavelengths, effectively eliminating laser induced fluorescence and absorbtion as detection methods. Instead, ND_3 molecules exiting the guide were were detected via 2+1 REMPI using a 6 mJ pulsed laser at 317 nm. This laser was focussed via a 300 mm focal length fused silica lens (beam diameter 10 mm); due to the rather low mode quality of the UV beam, the spot size at the focus is estimated at about 50 μm, 10 times larger than 10 μm diffractive limit. The ND_3+ ions produced were accelerated via electrostatic plates and then detected via a multichannel plate. The mass resolution of this time of flight mass spectrometer was $\approx$ 1 part in 50; This was sufficient to resolve ND_3 from ND_2H. This REMPI detection scheme is state selective and has excellent timing resolution, based on the time of the ionizing pulse, but the relatively high linewidth of the laser precludes any type of direct velocity measurements via doppler shifts. A sketch of the MCP assembly is shown in figure 3.4.

The guide consists of six 1 mm diameter stainless steel rods with a center-center spacing of 2 mm. The guide entrance is positioned 30 mm from the exit aperture of the cell, slightly beyond the expected position of the last collision between a typical ND_3 molecule and buffer gas atom. The position of this last collision is velocity dependent, with slow molecules suffering more collisions. We therefore speculate that the dominant loss mechanism for the very slowest molecules in the beam is collisions with buffer gas atoms in the first few centimeters of the guide; see section 2.4.3 for further discussion.

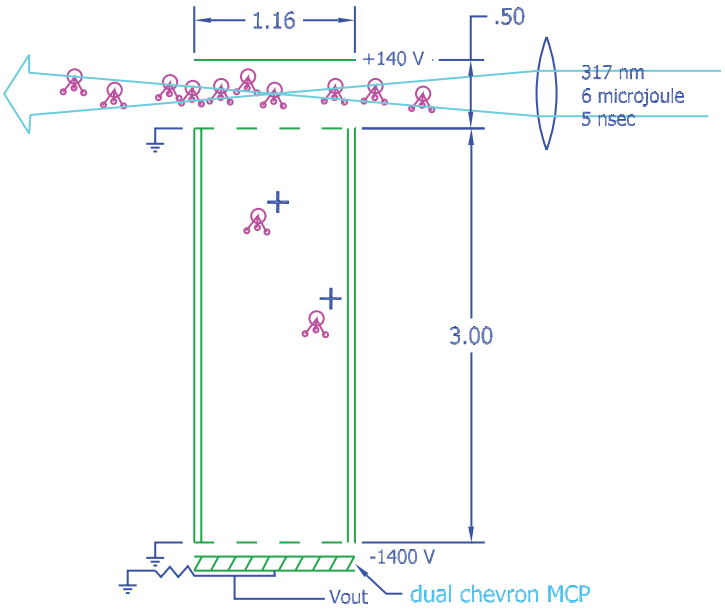

Figure 3.4: Overview of the mass spectrometer assembly for 2+1 REMPI detection of ND_3. Dimensions in inches. The MCP itself did not function unless it was heated to ≈ 80 K; this is a known effect, which arises from the freezing out of charge carriers on the surface of the channels. Photos of the assembly are found in appendix C.6.

The guide is constructed from alternating rods held at 5 kV and ground, producing a linear hexapole field. The guide rods were held in place with Ultem brackets; the entire assembly was mounted to the 6K cold plate. Two guides were constructed. The first was 15 cm long and described an arc with a 24 cm radius; the second was 70 cm long and describes a complete loop with a bend radius of 8 cm. The first 30 cm of this second guide can be switched on or off independently from the rest of the guide. Photos of these guides are shown in figure 3.7 and figure C.3

Arcing and leakage current

Both spontaneous arcing and surface leakage currents along insulators are typically problematic for a high electric field room temperature apparatus. We were unable

to test our apparatus at room temperature, due to bad vacuum from our large, dirty cryopumps, but at low temperatures no detectable (< 0.1 μA) leakage current flowed along the surface of the Ultem brackets despite the fact that few precautions were taken to avoid such currents, and later experiments with teflon standoffs showed similar immunity to leakage. We also saw no electrical arcing, although our maximum field of 50 kV/cm is rather modest by industry standards. We took very few precautions to prepare our surfaces well; the electrode rods shown in figure 3.7 were 316 stainless steel welding rod; they were hand polished on a lathe for the shorter guide (upper pictures in figure 3.7) and unpolished in the longer guide (lower pictures in figure 3.7). We speculate that such surface currents are suppressed at low temperatures, which has been reported elsewhere for other plastics [42].

3.2.3 Guided ND_3 results

Figure 3.5 shows the multi-channel plate signal as a function of laser frequency with the shorter guide installed. There is clearly an enormous increase in signal when the guide is turned on. This signal represents guided, state selected molecules with velocity $\lesssim$ the guide cutoff velocity of 160 m s^{-1}.

In a typical experimental run with the longer, more sharply bent guide, the first 30 cm of the guide is turned off and the remainder of the guide is charged. The first section is then turned on, and, after a variable delay, the pulsed REMPI laser is fired, measuring the density of molecules a few cm away from the guide exit. The velocity distribution in the guide, shown in figure 3.6, is inferred by varying this delay. We only present a conservative lower bound on the guided molecule flux as absolute density

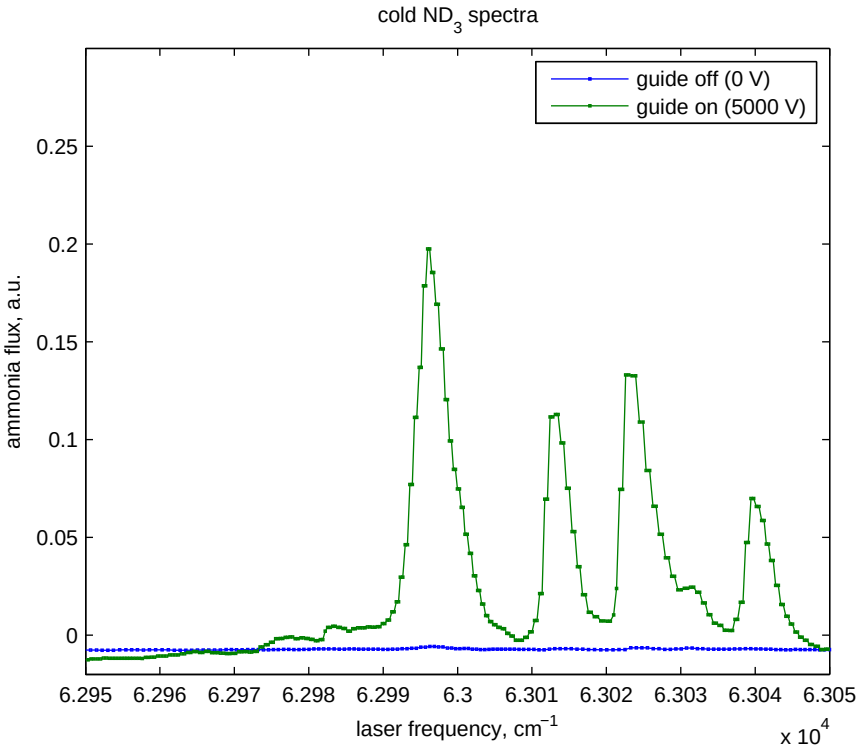

Figure 3.5: Typical guided spectrum of the ND_3 B5 SVL rotational manifold. The $\Delta P = 0$ selection rule for this two photon transition implies that guided (antisymmetric) states couple only to odd vibrational states; no guided signal is seen on the B6 transition ($\approx$ 63550 cm^{-1}). The blue trace shows the spectrum with the guide turned off; a very small signal is detected, due to unguided ND_3 that scatters into the detection region. This signal represents a guided flux of about 10^{10} molecules s^{-1}

measurements are notoriously unreliable in MPI experiments; our quoted flux is based on very conservative comparisons with similar, calibrated experiments on ND_3 done in other groups[8]. We find a lower bound of 3×10^8 guided molecules per second with an average energy corresponding to a temperature of about 4 K.

The ND_3 beam was initially demonstrated using both helium and neon as a buffer gas. Figure 3.8 shows the measured velocity distribution of a guided beam of ND_3 using helium and neon as buffer gas under otherwise similar conditions. The guide used in this work has a significantly larger (70 cm) radius of curvature, leading to a much

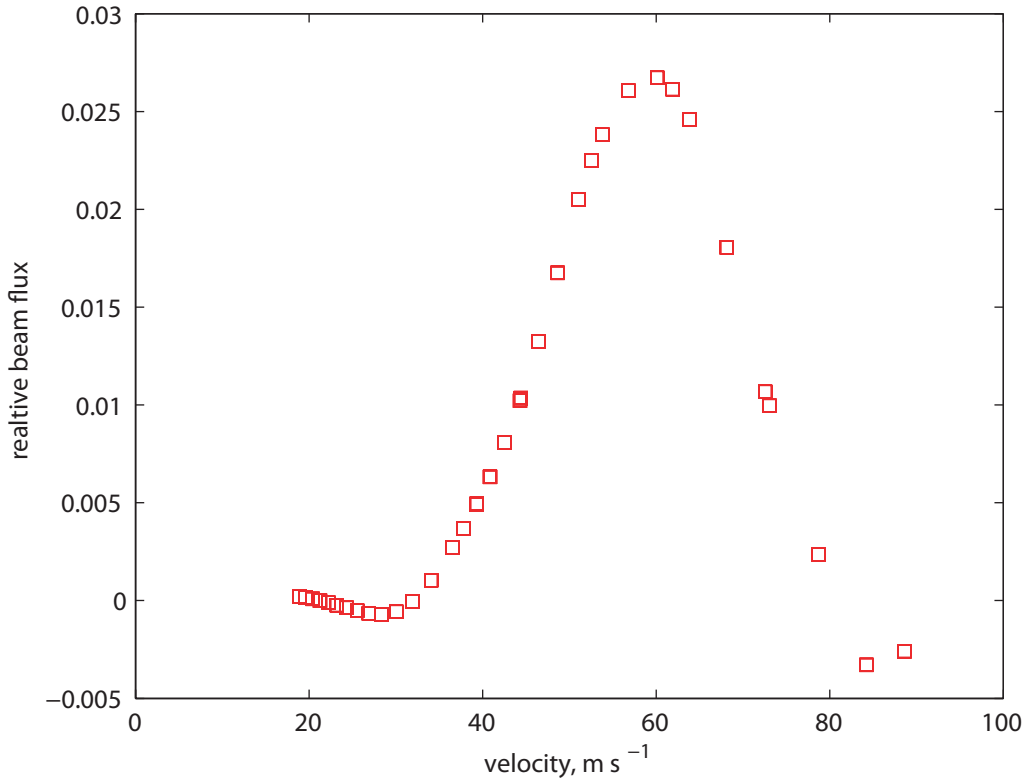

Figure 3.6: Velocity distribution at the output of a 70 cm long electrostatic guide with a bend radius of 8 cm. The output of this guide is completely separated from the neon buffer gas, and represents a pure, state-selected, low energy beam. This data represents 3×10^8 ND_3 molecules s^{-1}, with a mean energy of about 4 K.

higher velocity cutoff in the beam guide output velocity distribution. Significantly more slow molecules are produced in the beam using neon buffer gas.

3.2.4 Guide depth, guide radius, and guided velocity

A molecule moving down a bent beam guide experiences a potential that is a sum of the electrostatic potential from the guide, and a pseudopotential from the centrifugal force $F = mv^2/r$. Figure 3.9 shows this effective potential for various velocities and voltages. The guides do not show a sharp velocity cutoff, but rather

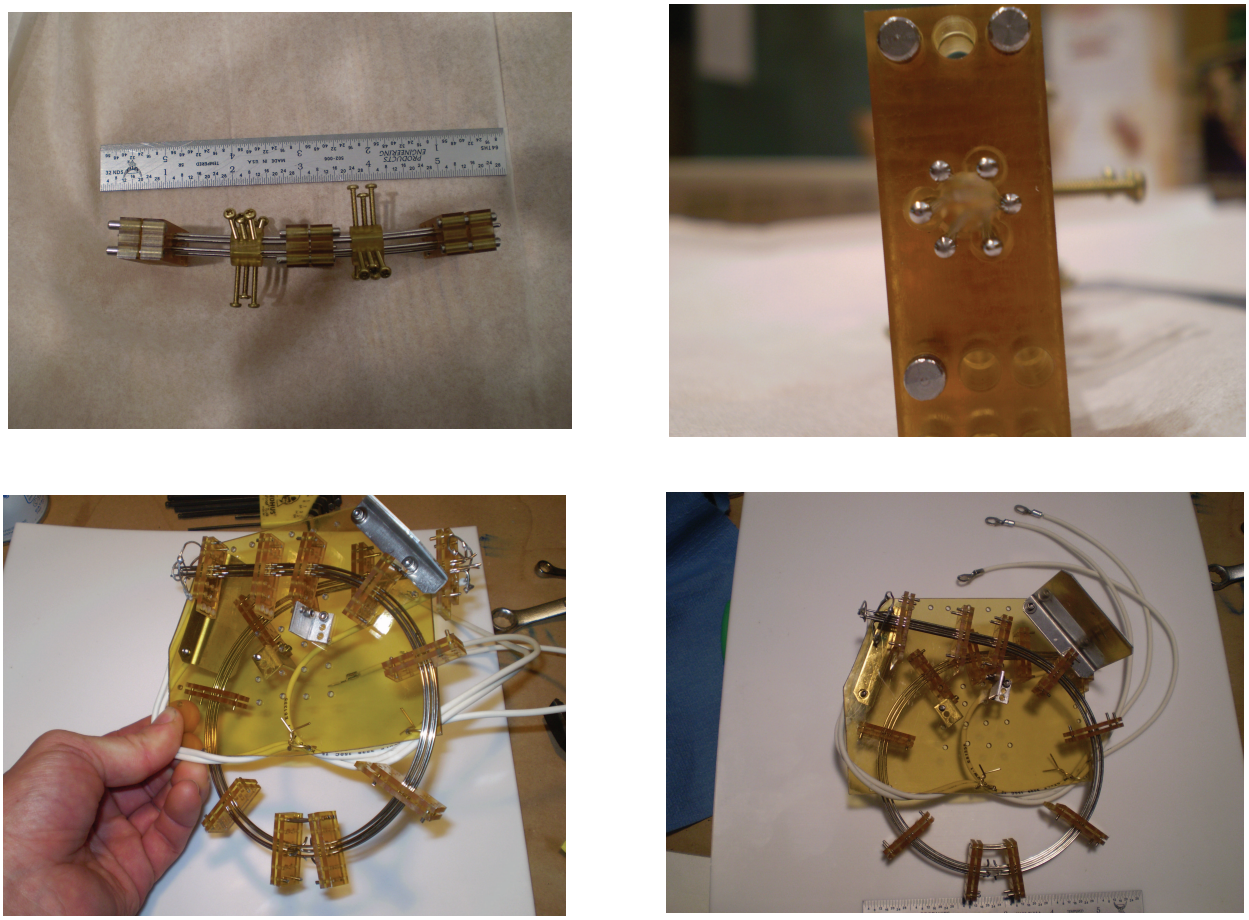

Figure 3.7: The electrostatic hexapole guides. The rods are 1.5 mm diameter 316 stainless steel welding rods, cleaned but not electroplated or polished; the holders are .125 inch thick, made from ultem. No arcing or leakage currents were detected with voltages up to 6000 volts between adjacent rods.

get more and more shallow transversely as the centrifugal pseudopotential gradually overwhelms the electrostatic potential. The transverse guide depth, and therefore the guided flux, is therefore expected to gradually diminish as $v_{forward}$ increases. Figure 3.10 shows the guided flux as a function of guide voltage. Guiding begins to turn on at V = 1000 volts, providing early strong evidence that slow molecules ($v < 1000$ m s^{-1}) were in the beam.

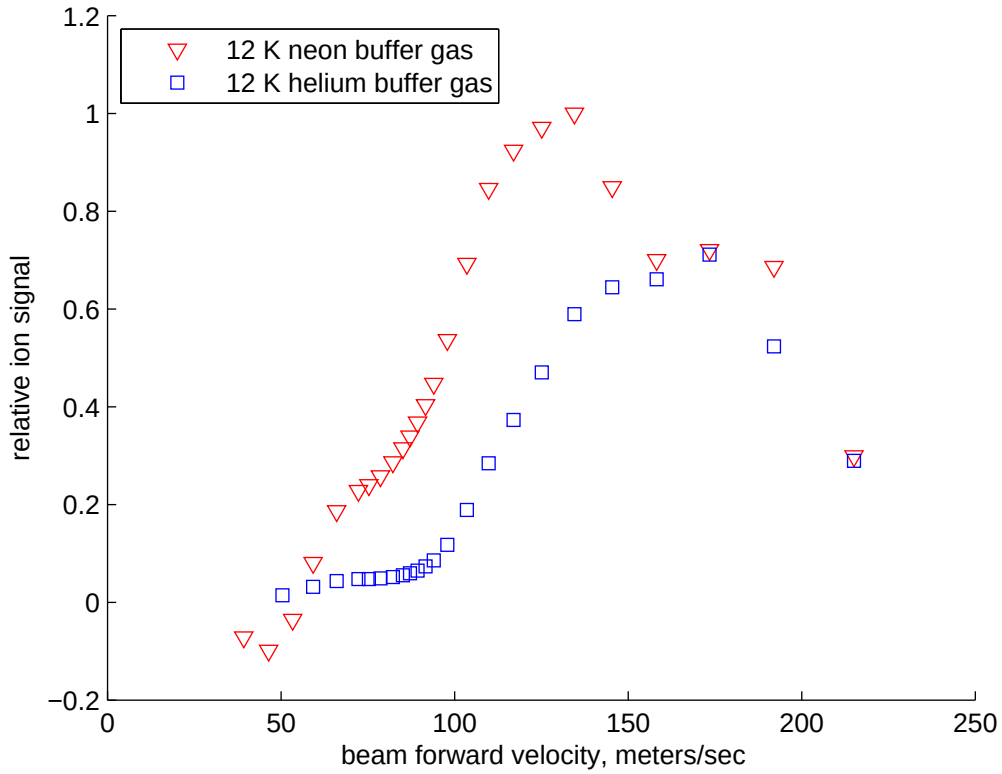

Figure 3.8: Measured forward velocity distribution of a guided ND_3 beam using 12 K helium [blue square] and 12 K neon [red triangle] as a buffer gas. This data was taken with the shorter guide described in section 3.2.2. The beam using neon contains substantially more low-velocity molecules. Molecules with a velocity higher than 200 m s^{-1} are moving too fast to be guided by this bent electrostatic guide (bend radius r =70 cm.) The red data [neon] represents a guided beam of about 2×10^{10} ND_3 molecules s^{-1} at a mean energy of $\approx$ 20 K.

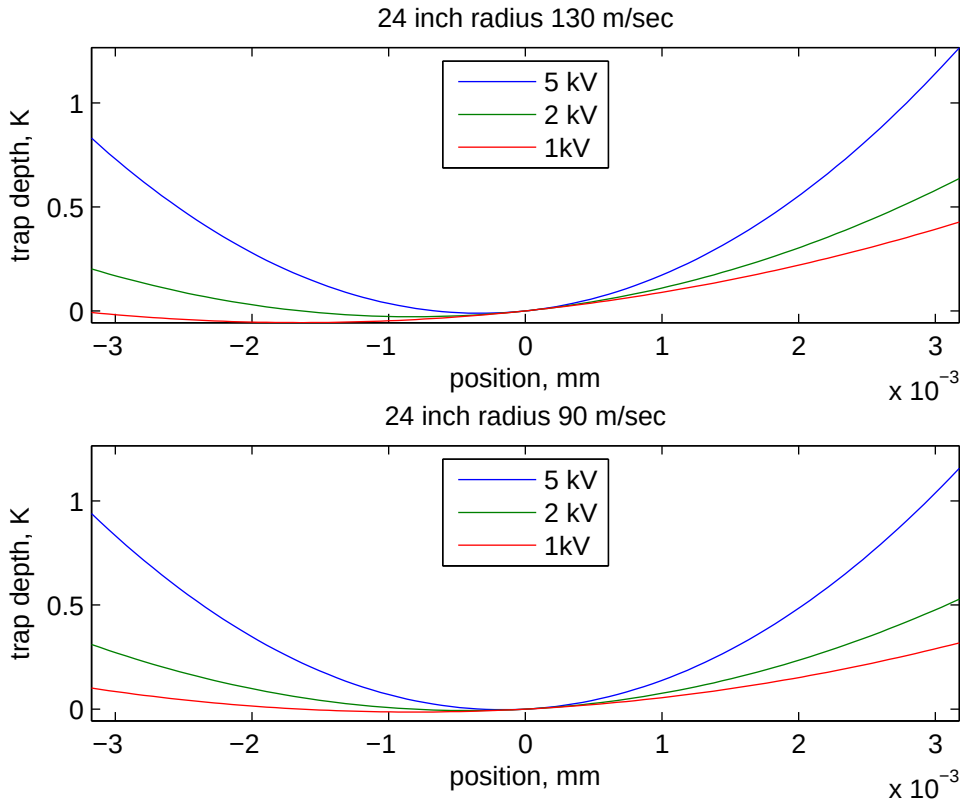

Figure 3.9: Effective pseudopotential for various voltages on 24 cm radius guide. At low voltages, the effective guide depth - and thus the guided flux - is strongly dependent on the velocity of the beam. Essentially no guiding should be possible for 130 m/sec molecules with 1 kV on the guide; the existance of the signal at this voltage was an early indication that slow molecules (< 130 m s^{-1}) were in the beam. This was later confirmed with the gatable, more sharply bent guide (figure 3.6), although more slow molecules were found using neon buffer gas.

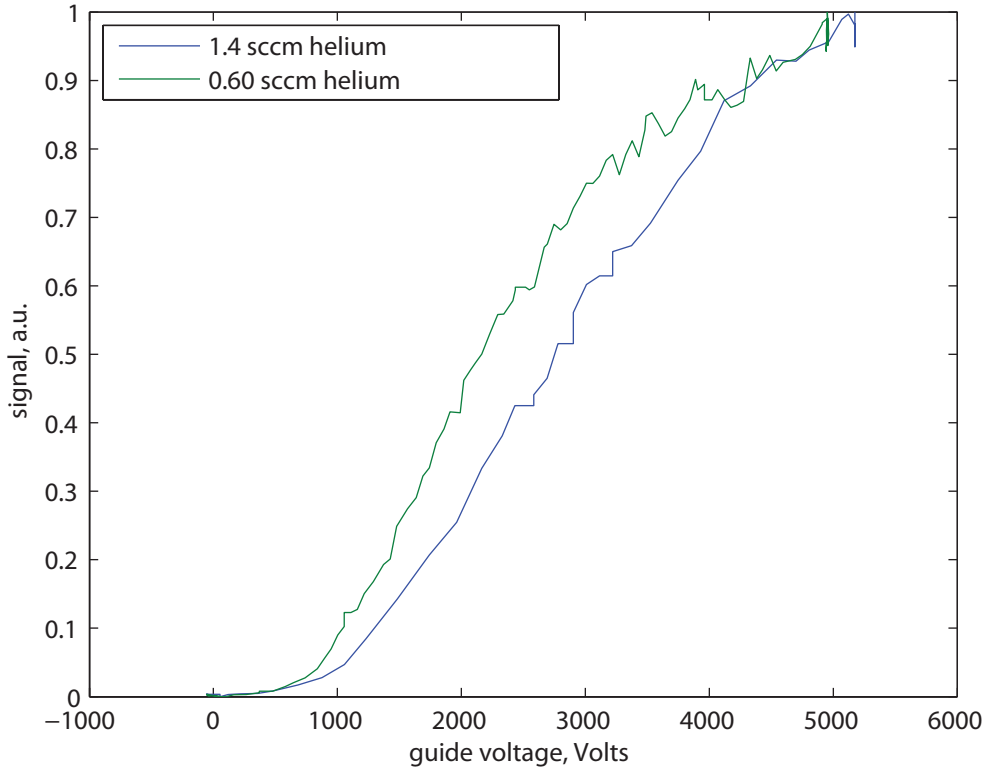

Figure 3.10: Flux as a function of guide voltage. The green trace represents 0.6 sccm of helium flow; the blue trace 1.4 sccm. The later turn-on of the guide for the higher flow is consistent with a moderately boosted beam, similar to the one simulated in figure 2.4.3. The flattening of these curves at high V $>$ 4000 volts is consistent with a model where the flux in this regime is geometry limited. At these high voltages, every molecule which hits the front face of the guide is guided.

Chapter 4

Buffer Gas Cell Loading Methods

Before we can buffer gas cool we need to introduce the species to be cooled into the cell. The perfect loading method for species A would have the following characteristics:

- **High Flux:** We want to be able to load as much of A as we like - at least until $A - A$ interactions become a self-limiting factor
- **Clean:** We want to load A and *only* A. This is especially important in cell experiments looking at collisions, where the role of spectroscopically invisible "partners" can easily confound the data; in trap and guided beam experiments, the trap itself often acts as a cleaning filter.
- **General:** We want to be able to load a wide range of species, and ideally any combination of these species.
- **Controllable:** Many experiments can be done with pulsed sources, but the ideal source - especially for the continuous trap loading techniques outlined in

section 6.5.2 - would be continuous and switchable

- **Low thermal footprint:** Cryogenic systems at 4 K generally have a modest thermal budget of ≈ 1 watt; this drops rapidly at lower temperatures. More critically, the buffer gas itself typically has a *very* low tolerance for excess heat. For example, a 1 cm^3 cell filled with $n = 10^{16}$ helium atoms will heat up 10 K if as little as 2 μJoules of energy is deposited. Thermal budgets often end up limiting fluxes.

Table 4 summarizes demonstrated methods of loading buffer gas cells. It is in general much harder to produce a clean beam of molecules than of atoms - this is because with atoms, it is impossible to be too violent in production; atoms are already "as ripped apart as they can get." With molecules, and especially radicals, it is very easy to accidentally disassociate the molecule of interest while attempting to simply vaporize it, and the experimenter ends up being forced to work with a mixture of atomic and molecular species. One of the main advantages of direct flow loading (section 4.2) is that it allows the specialized tools of modern room temperature chemical synthesis to be brought to bear on this problem.

Method	demonstrated species	flux	clean?	continuous?	thermal footprint
ablation	metals, CaF, ThO	$10^{11} - 10^{14}$/pulse	Y for some atoms, N in general	N	2-20 mJ/pulse
loading from a molecular beam	NH, N, Rb	10^{10} s^{-1}	as beam source	Y	excellent
cryogenic discharge	H,He*	varies, $n \approx 10^{10}$	Y	Y	medium
capillary fill	O_2, Rb, ND_3	10^{16} s^{-1}	Y	Y	excellent for O_2; poor for others
direct gas flow	Naphthalene, K, Rb	10^{16} s^{-1}	Y	Y	moderate

Table 4.1: Summary of the performance of various buffer gas cell loading methods

4.1 Previously Demonstrated Methods

4.1.1 Ablation

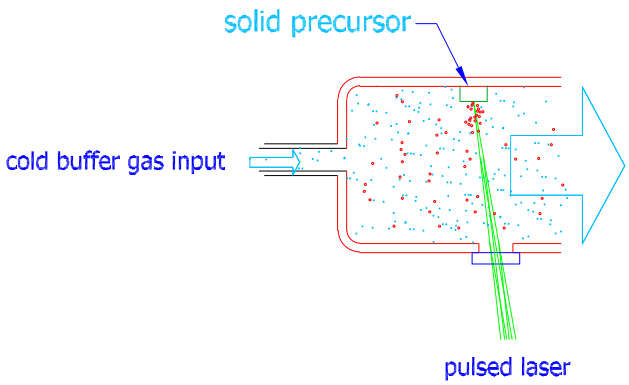

Figure 4.1: Buffer gas cell loading via laser ablation

Laser ablation - vaporizing a sample of a solid precursor with a pulsed laser - is to date the most widely applied method of loading buffer gas cells. The pulsed laser typically delivers 2-20 mJ in $\approx$ 5 nsec; in our work, we use frequency doubled Nd-YaG lasers with $\lambda = 532$ nm, but wavelengths from UV to IR have been used. A hot gas sample, typically with $N = 10^{11} - 10^{13}$ atoms or molecules, is ejected from the precursor into the buffer gas, where it rapidly cools.

Ablation has been widely used with atoms and has also been used to produce diatomic molecules, including radicals; almost certainly in these latter cases it is simultaneously producing large fluxes of atoms and other molecules. The method is

very general; although yields are hard to predict, it is almost guaranteed to produce a detectable flux of any atomic species. The moderate heat loads of 1-20 mJ/pulse are compatible with dilution refrigerators.

Ablation in general requires a moderate to high buffer gas density ($n_{He} \approx 10^{16}$) to produce good yields. Heating of the buffer gas can be a problem, especially in small cells; see section 2.5, and especially figure 2.15.

In some cases - most notably with rubidium, but also with bismuth, gold, and other metals - it appears to also produce 'dust', some substance or disturbance which consumes the rubidium metal much faster than can be explained by diffusion to the cell walls[55][45]. This "dust" has been observed by other groups as well[96][47], and is at present unexplained; theories include Rb_n clusters, droplets, metal·He clusters, and thermally excited vortices in the cell. One of the hopes - at present unconfirmed - is that direct flow loading of rubidium and other alkali species will circumvent this poorly understood but troublesome phenomenon.

Ablation is also notoriously unrepeatable.

4.1.2 Capillary injection

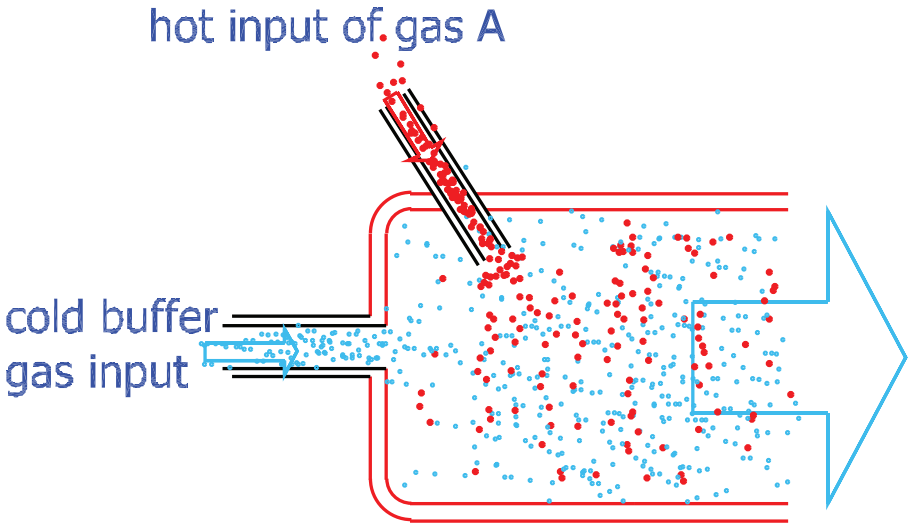

Figure 4.2: Buffer gas cell loading via capillary injection

In capillary injection method, the gas A to be studied is injected through a thin capillary that is heated to a temperature at which there is a significant vapor pressure of A. This gas flow then mixes with cold helium or neon gas that is concurrently flowed into a cell. A major drawback of this method is that it lacks generality; the thermal requirement that the capillary temperature be $\lesssim 400$ K limits the technique to species with a boiling point $\lesssim 600$ K; as such it is a poor choice for most atoms, but is applicable to many small and medium sized molecules. The method cannot be used with radicals, which would not survive in the capillary regardless of temperature. Capillary injection is the method used to inject ND_3 and O_2 in chapter 3.

Capillary injection has been used to load buffer gas cells in a number of microwave and NIR spectroscopy experiments, including experiments studying cluster formation with small molecules[4], high resolution IR and microwave spectroscopy with both

small[2] and larger[91] molecules at $\sim$ 100 K, and collisional broadening of the inversion transition in NH_3 colliding with cold helium, H_2, and D_2 buffer gasses[111]. Reference [4] contains an excellent summary of the early history of this technique, which can be traced back to Herzberg et. al. in 1952[49][1] . Much of this work came to our attention after our own experimental work was completed.

The injection method used in the above work is almost universally described as a variant on what is described here as "capillary injection", although this language is not used. It is in fact clear in hindsight that both this work and much of the earlier work in our lab has relied on the same collisional physics as described in the direct-flow loading section below (see section 4.2.3.

Fundamental limits

In an (unrealistic) ideal system, the only heat load delivered to the gas in the cell would be from the hot species A itself. In this case the gas mixture will come to a temperature intermediate between the hot input gas and the cold buffer gas. If the two inputs have temperatures and flows T_{hot}, T_{cold}, ϕ_{hot}, and ϕ_{cold} respectively, the

[1]Two separate, but rather similar sets of buffer gas cooling experiments have been performed in the last two decades. One set of experiments, pursued by physicists (spearheaded by Doyle, but also furthered by Ye, Rempe, and others), has referred to the technique as "buffer gas cooling"; this work inherits from early experiments where atomic vapors were introduced into static, non-flowing buffer gas cells, typically by laser ablation or RF discharge. The other set of experiments, performed by both chemists and physicists (F. De Lucia, D. Willey, H. Cammenga and others) call the technique "collisional cooling". These experiments inherit from room temperature gas-phase absorbtion spectrometry experiments, which have been adapted to capillary-injection buffer gas cells at both 77 K and 4.2 K. The species studied are typically small, polar molecules that are gas-phase at 300 K, such as NO, NO_2, and NH_3. Communication and cross-fertilization of ideas between these two sets of experiments has generally been poor; in more than one case similar technical improvements have been unknowingly developed in parallel. The work presented in this thesis of course inherits from the earlier "buffer gas cooling" work of Professor Doyle, but really should represent a merging of these two "families"

final temperature will be

$$T_{final} = \frac{\phi_A C_A T_A + \phi_{He} C_{He} T_{He}}{C_A \phi_A + C_{He} \phi_{He}} \tag{4.1}$$

where C_A and C_{He} are the heat capacities of species A and helium respectively. In fact, $C_A \leq 2C_{He}$ for any reasonable case, so these capacities can be ignored in reasonable approximation.

Equation 4.1 implies that there will be "unacceptable" heating ($\Delta T \gtrsim T$) if

$$\phi_A > \phi_{He} \frac{T_{cold}}{T_{hot}} \tag{4.2}$$

This limit can be quite high; for the case of 60 K O_2 injected into 5 sccm of 4 K helium, this limit would correspond to a flux of 0.4 sccm, or 1.6 $\times 10^{17}$ O_2 s^{-1}.

Thermal conduction into the buffer gas

In practice the heat load on the buffer gas can be much higher than the 'ideal mixing' case presented in section 4.1.2. Heat is also deposited in the gas by conduction: Helium atoms touch the hot capillary, heat up, and diffuse back into the cell. This heat load is especially problematic since it is deposited directly into the low heat capacity buffer gas, rather than the walls of the cell. If we estimate a buffer gas density of $n_{He} = 10^{16}$ at 4 K, and a rather optimistically small outside area of the capillary of .01 cm^2, this heat load is 10 times the maximum load estimated in section 4.1.2.

Capillaries at low pressure

The need to limit thermal loads drives the experimenter towards tiny hypodermic input capillaries; but these in turn are problematic, due to their low conductances.

These limits can be illustrated by a numerical example. Consider the case of trying to load a cell with an alkali metal (potassium in this example) via capillary injection. The low vapor pressure of potassium requires one to heat the capillary rather aggressively. Although it presents substantial engineering challenges, for now we assume that we can construct a (small) fill line heated to 600 K without unduly thermally loading the cell. Initially this seems like it will be warm enough - the saturated vapor pressure of potassium at 600 K is 0.2 Torr [86], which corresponds to a significant density of about $n_K = 10^{16}$ cm^3.

The conductance, C, in liters s^{-1}, for a short tube, Diameter D [cm], Length L, [cm] in molecular flow regime, is $C_{molecular} = 12.1D^3/L$[86]. A hypodermic capillary, with an inner diameter of .01 cm, and length of 0.1 cm, gives $C \approx 10^{-4}$ L s^{-1}, or 0.1 cm^3 s^{-1}. This implies $\phi = 10^{15}$ atoms s^{-1}. In this example the tube is in fact in an intermediate regime between molecular and viscous flow. In the viscous flow regime, the conductance is $C_{viscous} = 182\bar{P}D^4/L$, with P in torr. This is about 2×10^{-6} liter s^{-1}, or 50 times lower than the molecular flow regime. The actual conductance is likely to be between these two values. We therefore have a predicted final input flux of a rather modest $\phi \approx 10^{14}$ for potassium and other species with comparable vapor pressures, and we are driven towards other technologies.

Experimental realizations

Despite the worrisome calculations of sections 4.1.2 and 4.1.2, capillary injection with the capillary heated to temperatures of $\lesssim 300$ K works moderately well. Section 3.2.2 describes an implementation of such a system; photos of injector capillaries used

in this work are in appendix C.8. The capillary tip was set several mm back from the main body of the cell in an effort to avoid the conductive heating described above. In fact the system was found to produce a cold beam even with substantially higher input flows than equation 4.2 would allow; this suggests, in retrospect, that thermalization with the walls was playing a significant role in cell dynamics (see section 4.2.3).

Ice buildup and heat 'pulsing'

Both our group and the group of Jun Ye[87] have seen "pulses" of bad vacuum when operating these capillary nozzles. These pulses, which remain to some degree unexplained, occur spontaneously, but never in the first five minutes or so of operations; as can be seen in figure 4.3, the pulses at times seem to be semi-periodic.

These pulses have occurred in several different systems where large amounts of 'freezable' gas is flowing into a cold cell. The current leading theory is that icicles of frozen ammonia or oxygen are forming on the cold cell surface near the hot tip of the capillary. When the tip of an icicle reaches the hot inner tube it rapidly boils, dumping a massive heat load, and in turn a massive gas load from desorbed helium, into the system. There also seems to be a correlation between this pulsing behavior and large amounts of superinsulation in places where it can get covered in ice; the superinsulation has very low thermal conductivity and very small heat capacity, and so it becomes the perfect substrate for a thermally floating "bomb" of vaporizable ice.

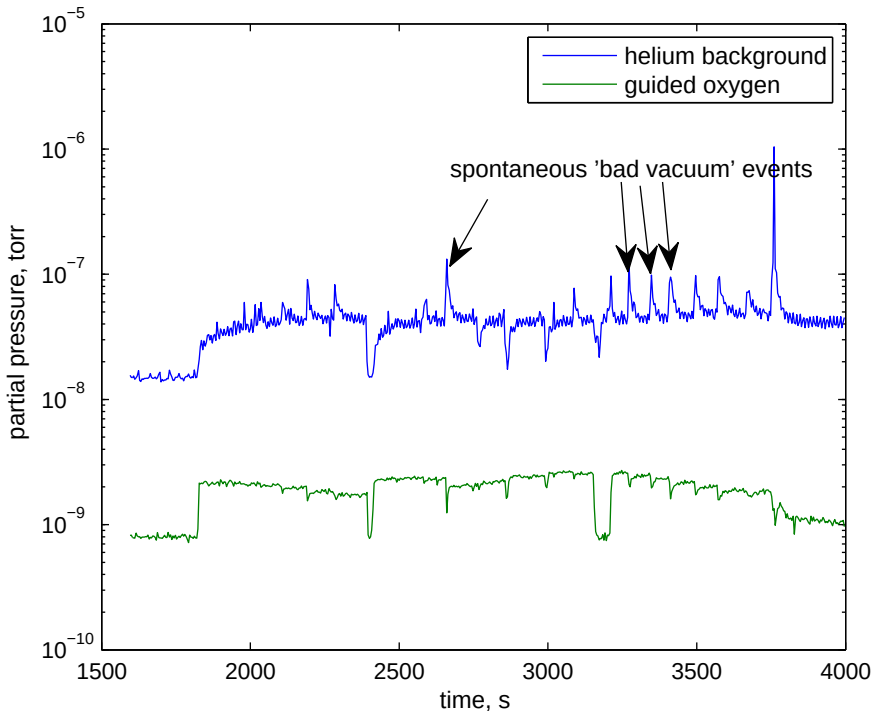

Figure 4.3: Magnetically guided O_2 signal (green) and helium background (blue), showing heat "pulsing" in typical capillary fill. The marked "bad vacuum" events, with spikes in the helium background pressure and corresponding drops in the guided O_2 signal, are spontaneous and remain unexplained.

4.1.3 Beam loading

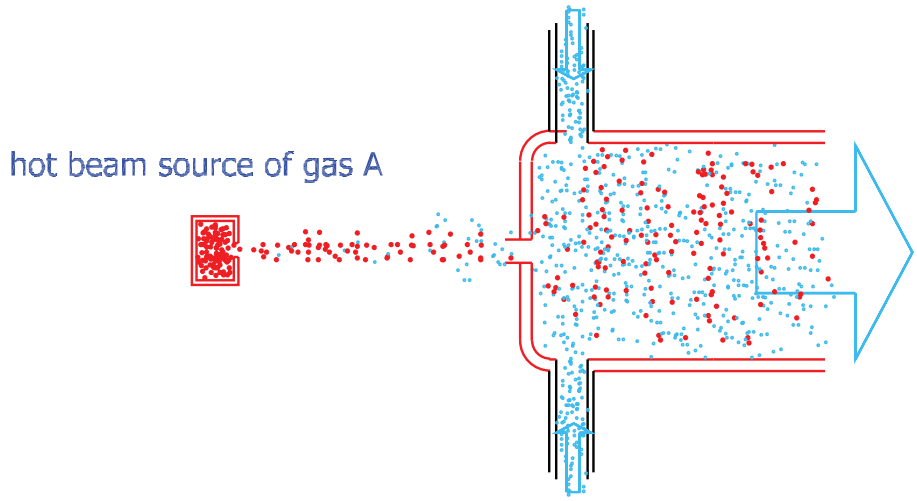

Figure 4.4: Buffer gas cell loading via molecular beam loading

Atoms or molecules can also be loaded from a beam, which is injected into the cell via a small hole[20]. The molecules must "swim upstream" for a short distance to make it into the cell. This method has many advantages:

- Enormous generality - the beam source can be at any temperature, and techniques to produce molecular beams of radical species are well developed
- The problem of thermal conduction directly from the source to the buffer gas is completely eliminated
- Unlike the capillary injection or direct gas flow methods, fast shutters in the input beam make this method rapidly switchable.

These advantages are offset by generally low input fluxes, and an additional - often quite strict - constraint on cell conditions, which must find just the right "happy

medium" of helium density: low enough to allow the molecular beam to get in, but high enough to thermalize the molecules once they are in the cell. These cells tend to be have the lowest buffer gas helium densities our group has worked with, which can be a blessing in itself - once the cold beam is back outside of the cell, high helium flux becomes a problem, since it leads to a poor background vacuum. The "magic plate" proposed in figure 2.8 is a proposed implementation of a "hot beam to cold beam converter".

An early version of the ND_3 beam discussed in section 3.2.2 used this technique to load the cell. Although a cold beam of ND_3 was produced, this approach was later dropped because the capillary injection, being developed in parallel, delivered higher fluxes.

4.2 Loading cells via direct gas flow

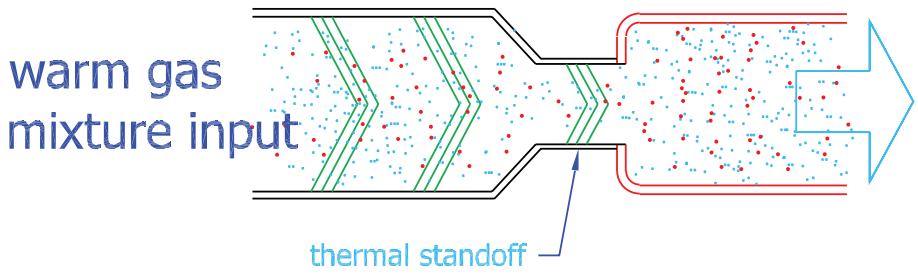

Figure 4.5: Buffer gas cell loading via direct gas flow

Direct gas flow loading is a new method of loading buffer gas cells, although it is many ways it is a grandchild of "smoke chambers" that have been in use for studies of particulates and clusters since at least 1913[80]. This is the technique used in references [77] and [79]; implementations are shown in figures 2.18 with potassium and chapter 5 with naphthalene.

Direct gas flow loading appears on the surface to be very similar to capillary injection, but in fact relies on substantially different physics. In direct flow loading, a hot mixture of species A and the buffer gas is prepared at a "warm" temperature, warm enough that A has a significant vapor pressure. This mixture is injected as rapidly as possible into a cold (≈ 4 K) cell; in some realizations[77] it is first (and also rapidly) heat sunk at 300 and 77 K, but in the most recent work it is simply injected directly from 300 K. Unlike capillary injection, this method relies heavily upon thermalization with the cell walls. Because this technique has not been published elsewhere outside of references[77] and [79], it is presented here in greater detail than the above methods.

The essential processes of loading cryogenic cells via gas entrainment are as follows: At time $t = 0$, a warm mixture of helium buffer gas, of density n_{he}, and species A, of mass M and density $n_A << n_H e$, is introduced into the cold cell, at temperature T_{cell}. The two species interact only via elastic scattering, with cross sections σ_{he-he} and σ_{he-A}. It is assumed that any helium atom coming in contact with the wall is immediately cooled to T_{cell}, and any molecule of species A which touches the wall remains frozen on the wall forever.

As soon as the mixture enters the cell, two processes immediately begin to happen: the gas mixture begins to cool, and species A begins to diffuse to and stick to the walls. We are interested in the race between these processes: can the gas cool before all of species A sticks to the wall? Both of these processes depend only on geometry and elastic scattering, but it is not initially clear which will run faster.

4.2.1 Hard Sphere Theory

We are interested in comparing the thermalization time τ_{therm}, defined as the time it takes the gas to lose e^{-1} of its energy to the wall, with the time it takes a typical impurity molecule to diffuse to the wall, $\tau_{diffuse}$

Case 1: $M = m$

For the case of hard sphere interactions, and assuming local thermal equilibrium, ($\Delta T << T$), and $m = M$ the problem has been solved exactly.

The thermal conductivity of an ideal gas is given by

$$\kappa = \frac{n\bar{v}\lambda c_v}{3} \tag{4.3}$$

which leads to

$$\frac{\partial T}{\partial t} = -\frac{n\bar{v}\lambda}{3}\frac{\partial T}{\partial x} \tag{4.4}$$

For hard spheres, the equivalent to equation 4.3 is

$$D = .420\bar{v}\lambda c_v \tag{4.5}$$

[24]

where D is the diffusion constant. Just as in equation 4.4, we get

$$\frac{\partial n}{\partial t} = -.420n\bar{v}\lambda\frac{\partial n}{\partial x} \tag{4.6}$$

In other words, if all masses and cross sections are equal, heat diffuses 1.26 times faster than mass. This is slightly bad news from an experimental point of view - we want to keep the mass but lose the heat.

Case 2: $M >> m$

M, the mass of A, cannot effect the thermal conductivity of the gas, as the vast majority of the heat is carried by helium atoms that rarely encounter anything except another helium.

It is initially unclear whether the ideal gas diffusivity defined in equation 4.5 applies in the common case of $M >> m$. In this approximation, the impurity molecule is barely moving, but being bombarded from all sides by buffer gas atoms with momentum $P_m = \sqrt{2k_bTm}$. For $M = m$, it could be assumed that each collision would randomize the momentum of A, but this is no longer the case. The new typical momentum of a molecule of A is

$$P_M = \sqrt{2k_bTM}$$

while a typical collision still imparts a momentum kick of order

$$P_m = \sqrt{2k_bTm}$$

in a random direction.

After N such collisions, the total change in momentum imparted is

$$\Delta P = \sqrt{N2k_bTm}$$

which leads immediately to $N = M/m$. These factors combine to make the momentum-randomizing mean free time for the species A

$$\tau_{randomize} = \frac{M}{m}\tau_0$$

and the momentum randomizing mean free path becomes

$$\lambda_{randonmize} = \sqrt{\frac{M}{m}}\lambda_0 \tag{4.7}$$

Where τ_0 and λ_0 are defined as the mean free time and mean free path respectively in the $m = M$ case.

As M/m increases, molecules of the heavier species travel slightly further, but for substantially longer, than the helium atoms before having their momentum randomized.

What does this all add up to? We arrive back where we started:

The number of steps to reach the edge of the cell goes down:

$$N \propto \frac{R^2}{\lambda^2} \propto \frac{m}{M} \tag{4.8}$$

But each step takes $\frac{M}{m}$ longer - so the final diffusion time remains unchanged

$$\tau_M = \tau_0 \tag{4.9}$$

This slightly counterintuitive result - that the diffusion of a particle in a buffer gas is independent of it mass - can also be confirmed by looking at the theory of Brownian motion. Reif, page 567[84], explicity derives the mean square displacement $\langle x^2 \rangle$ for a particle of radius a, mass m, diffusing in a medium of viscosity η for time t to be

$$< x^2 >= \frac{k_b T}{3\pi\eta a} t \tag{4.10}$$

which is explicitly independent of mass.

Cooling rate and loss rate

Putting together equations 4.4,4.6, and 4.10, we get the general expression:

$$\tau_{therm} = 1.26 \frac{\sigma_{he-he}}{\sigma_{he-A}} \tau_{loss} \tag{4.11}$$

regardless of the mass of species A.

Equation 4.11 suggests that an important figure of merit for entraining a species A into a cold buffer gas cell is

$$\beta \equiv \frac{\tau_{loss}}{\tau_t herm} = .79 \frac{\sigma_{he-A}}{\sigma_{he-he}}.$$

$\beta > 1$ means that the density of species A drops faster than the temperature; $\beta < 1$ means the temperature drops faster than the density. Figure 4.6 shows the

time evolution of the temperature and density of a typical buffer gas cell for various values of β. It is clear that $\beta > 1$ is enormously helpful for achieving high densities at low temperatures.

It is worth noting that even for $\beta = 1$ the *phase space density* increases as the species cools. For a non-vibrating rigid-rotor molecule, the phase space density scales as nT^{-3}; for $\beta = 1$, $n \propto T$, so in this case the phase space density increases as T^{-2}. This can be thought of as taking advantage of the fact that momentum perpendicular to the wall, and other degrees of freedom, such as rotation, are "along for the ride"; these degrees of freedom cool with the helium buffer gas but do not contribute to transport towards the wall.

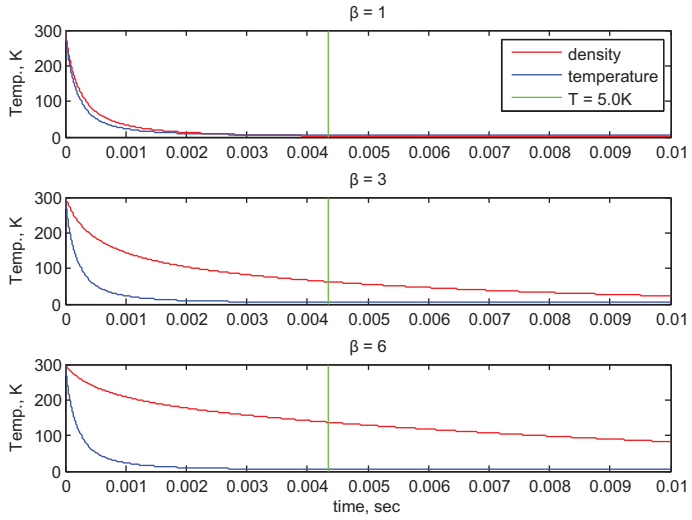

Figure 4.6: The relative density n_A and temperature T of a 4.2 K buffer gas cell loaded with a hot (300 K) mixture of helium and A. Three different values of $\beta \equiv \frac{\sigma_{he-A}}{1.26\sigma_{he-he}}$ are shown. It is clear that if one desires high densities of cold A, it is extremely helpful to have $\beta > 2$.

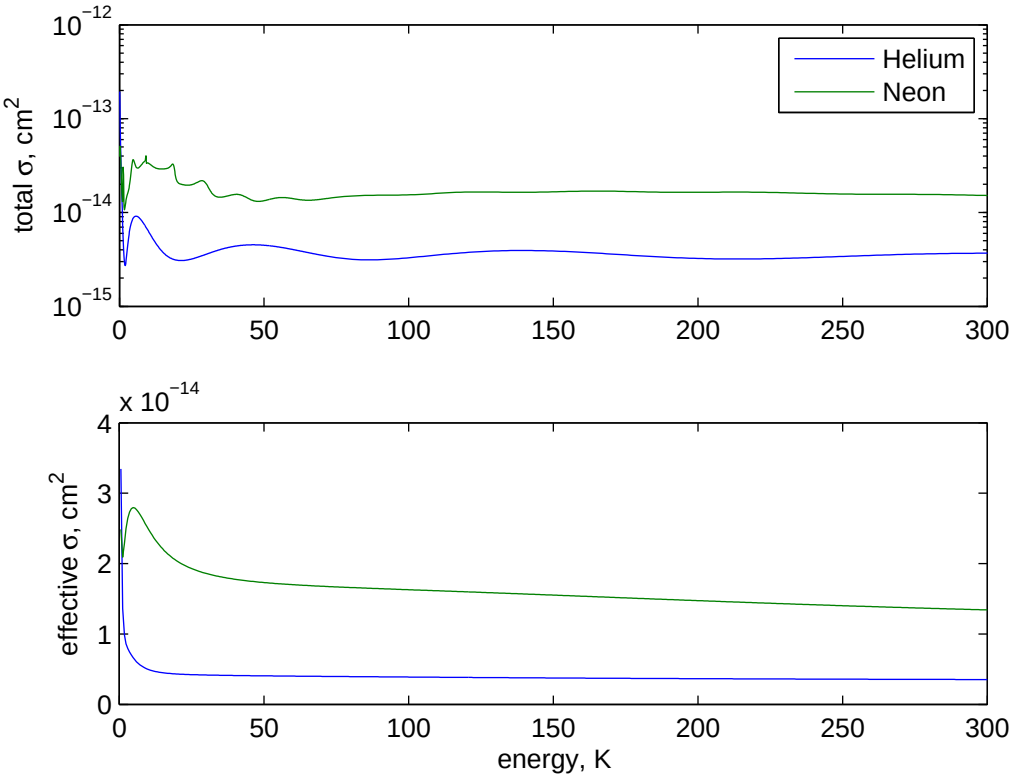

Figure 4.7: a) The mono-energetic elastic scattering cross sections σ_{He-He} and σ_{Ne-Ne}. b) The thermally averaged cross sections. Most collisions happen at comparatively high energies, minimizing the effect of the abnormally large σ_{He-He} at low temperatures. The helium cross section is accurate to at least 1 %; the neon potential is not as well known. Thank you to Timur Tscherbul for this simulation.

Numerical simulations

Some of the assumptions used in the "exact" hard-sphere model of section - in particular the assumption of local thermal equilibrium - are questionable. This uncertainty motivated us to simulate the system. This simulation is done with a one dimensional geometry; that is, the geometry is assumed to be an infinite planar cell, with hot gas ($T = 300$ K) introduced in between two infinite cold plates ($T = 10$ K). Figure 4.8 shows the results of such a simulation with $\sigma_{He-N} = 5\sigma_{He-He}$.

The gas can either be assumed to be at a constant density (as is appropriate in a sealed buffer gas cell, where V and N_{He} are fixed), or constant pressure, appropriate in a flow tube, where P is approximately fixed. In the latter case (which reflects reality for the experiments described in chapter 5, the density of naphthalene increases by an additional factor of T_0/T, as the gas compresses according to the ideal gas law. As can be seen in figure 4.8, the phase space density for this case increases by four orders of magnitude in the simulation.

Which buffer Gas?

The vast majority of buffer gas cooling experiments use either ^{3}He or ^{4}He as the buffer gas; primarily because helium has a usable vapor pressure at very low temperatures. Below 10 K helium is really the only choice; but for some experiments, in particular beam experiments, neon has both technical merits (it can be cryopumped exceedingly fast) and fundamental advantages (see section 2.4.7).

In general, for most species the potential and cross section with helium and neon is not known; it is therefore impossible to say for certain which buffer gas will yield the most advantageous value of β. Figure 4.7 shows the mono-energetic and thermally averaged elastic cross sections for σ_{he-he} and σ_{ne-ne}. σ_{he-he} is enormous for very low energies, due to the He_2 molecular bound state at very low energies; however, when averaged over a thermal ensemble, this effect is relatively small even at temperatures as low as 500 mK. Figure 4.7 suggests that helium is likely to be the better buffer gas for flow-tube experiments, but this remains to be, seen; there is substantial evidence, for example, that flow tubes with rubidium entrained in neon work than rubidium in

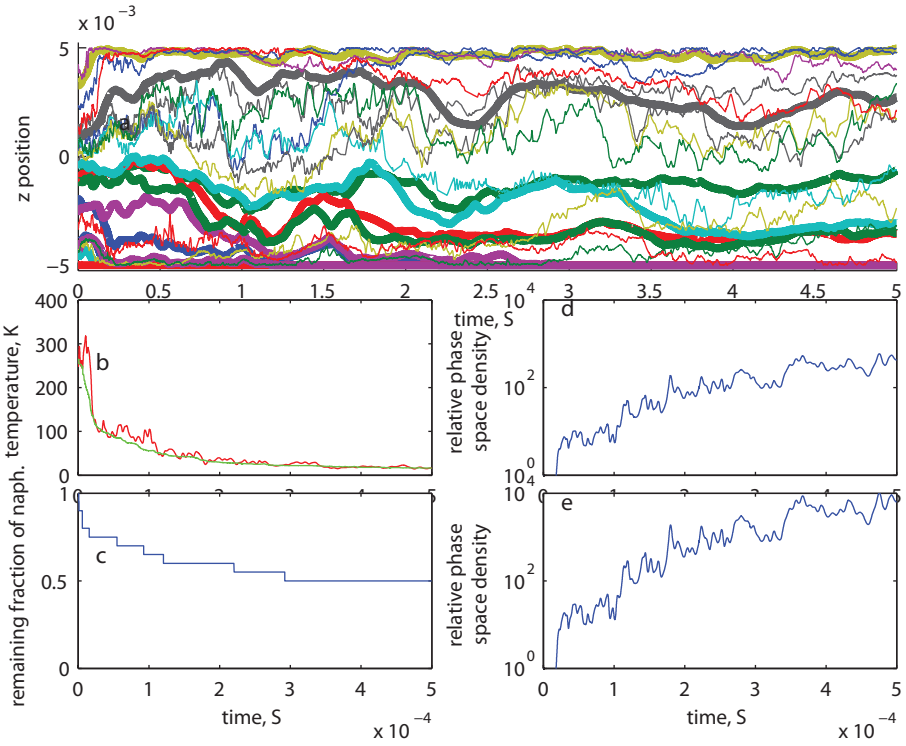

Figure 4.8: Results of numerical simulations of naphthalene imbedded in a helium buffer gas. Any helium atom which touches the wall is assumed to thermalize to $T_{cell} = 10$ K; any naphthalene molecule which touches the wall is assumed to stick and be lost. In this simulation, the elastic scattering cross section $\sigma_{He-N} = 5\sigma_{He-He}$. (a) the simulated trajectories of naphthalene (bold lines) and helium. (b) the simulated temperature of naphthalene and helium as a function of time. (c) the remaining fraction of naphthalene as a function of time. About half of the naphthalene ends up frozen to the walls. (d): the phase space density enhancement assuming a constant *density* of helium; this is appropriate for situations where N_{He} is fixed, such as an ablation cell. (e) the phase space density enhancement assuming a constant *pressure* of helium; this is appropriate for flow tubes. Note that despite a modest (50%) loss in absolute naphthalene number (subplot c), the phase space density in the flow tube increases by 4 orders of magnitude as the mixture cools. This simulation agrees quite well with figure 4.6c, which represents a simple analytical model with $\beta = 6$.

helium, suggesting that $\beta_{Rb-He}\beta_{Rb-Ne}$.

Figure 4.9 shows a classical picture of a helium atom and a naphthalene molecule to scale. The size of the helium atom is picked to agree with the measured helium-

helium elastic scattering cross section, while the bond lengths in the naphthalene are taken from x-ray diffraction experiments. Although these classical pictures can be deceiving, they are reasonably defensible in this case, where many partial waves and many rotational states will average out any quantum scattering effects. Figure 4.9 perhaps justifies our intuition that helium is a small atom, and naphthalene is a large molecule.

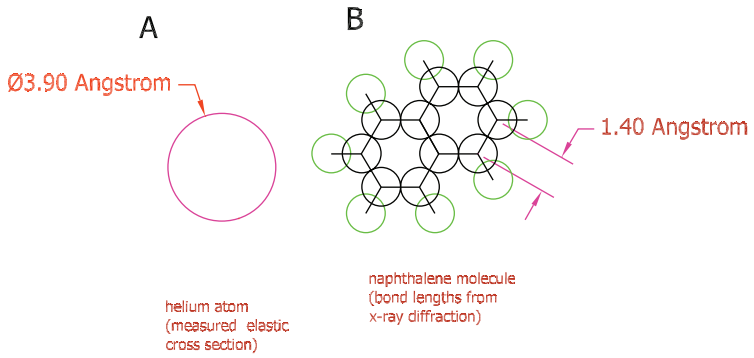

Figure 4.9: A "classical" picture of a helium atom and a naphthalene molecule. In A), a helium atom is represented as a hard sphere with the appropriate radius to match the measured elastic scattering cross section of 5×10^{-15} cm^2. In B), a naphthalene molecule drawn to scale, with bond lengths as measured by x-ray diffraction experiments. The green circles could be taken as a very conservative lower bound for the area which a helium atom must scatter off. It is unsurprising that $\sigma_{He-N} > \sigma_{He-He}$.

4.2.2 $\beta \lesssim 1$

Figure 4.6 would seem to imply that the flow tube method can only be used with species where $\beta > 2$. This is perhaps not the case. The typical figures of merit for buffer gas loading experiments are n, the final density, and T^{-1}. Direct flow loading must be compared to "cryogenically compatible" production methods such as discharges or ablation, which apply large parasitic heat loads to the cryogenic cell.

In the naphthalene experiment described in chapter 5, the final density seems to be limited by naphthalene-naphthalene interactions at low temperatures; in many other experiments, the final density is limited by the cooling power of the final cryogenic stage. In both these cases, it is imaginable that a higher final density could be achieved by producing an enormous flux at room temperature, where energy budgets and vapor pressures are favorable, despite the fact that several orders of magnitude will be lost on the way down the flow tube.

4.2.3 Have we been doing direct flow cooling all along?

This chapter has so far considered direct flow loading in the context of a flow tube, where warm gas is being physically injected into a cold 'cell tube', but it is worth noting that very similar physical processes are almost certainly happening in the first few moments after an ablation pulse in conventional buffer gas cooling. We have substantial evidence (see for example, section 2.15) that ablation pulses can heat the gas in buffer gas cells by 10s of kelvin at least, yet we have an enormous volume of data on ablation experiments which were subsequently reliably measured to have low temperatures. Either the ablation in these many cases is orders of magnitude more efficient than the data shown in section 2.5.2, or we have for years been cooling hot helium gas to cold cell walls. If this is the case, it suggests that the cross section criteria $\sigma_{He-X} > \sigma_{He-He}$ might be satisfied not only by classically "large" molecules such as naphthalene, but also by many atoms.

Chapter 5

Buffer Gas Cooling of Naphthalene

Prior to the work presented in this chapter, buffer gas cooling had only been demonstrated with small ((< 6 atoms) molecules. The work presented here demonstrates efficient cooling of naphthalene ($C_{10}H_8$), and includes analysis suggesting that the same technique will succeed with most molecules of comparable structure. This greatly increases the generality and applicability of the direct flow buffer gas cooling method.

5.1 Background: other work with cold, large molecules

Driven by a variety of new science, including cold chemistry and dipolar quantum gases, several methods are now being pursued to produce cold and ultracold samples of molecules. The cold molecules in these studies are generally diatomic but also include few-atom molecules such as ND_3.[23]. Extending this work to the cooling of larger molecules is of high interest, as reviewed by Meijer et. al.[63] and references

therein. For example, chemical reaction rates at low temperatures are of great current interest, and extending these studies to important large molecules is essential. Ultraprecise spectroscopy experiments could make use of new continuous cryogenic molecular beams to test fundamental symmetries[27] There is great interest in field mediated chemistry, and a general source of high density, highly polarizable ground state molecules is an excellent testbed for observing field mediated chemical reactions. These and other applications of a general source of larger, cold molecules are examined in greater detail in chapter 6.

In previous work with buffer gas cooling, cold, guided beams of molecules as large as trifluoromethane (CF_3H) have been produced.[92][77]. In related work, a beam of slow (11 m s^{-1}), but rotationally and vibrationally warm (300 K), PerfluoroC_{60} (mass $>$ 6000 amu) was produced by filtering slow molecules from a warm sample[29]. However, the only demonstrated technique for producing samples of cold molecules with atom number higher than five is the seeded supersonic jet. Seeded supersonic beams have a rich history and have found great utility in spectroscopic studies[65], as sources for molecular trapping experiments[63], and in cold chemistry experiments using the CRESU technique[90]. They are limited, however, because although they produce translationally and rotationally cold molecules, these molecules are moving at very high velocity (300 m s^{-1} or higher). Furthermore, the beam evolves spatially with a rapidly decreasing density as the molecules move away from the beam orifice.

New cold beam methods (some mentioned just above) are part of a renaissance in molecular beams. Part of this renaissance is the use of electric and magnetic fields to manipulate and decelerate polar and magnetic molecules. In many cases, these meth-

ods are applied to molecules in metastable states, such as low-field seeking electric dipole states. Extending these slowing and trapping methods to larger molecules is inherently problematic because, unlike diatomics and few-atom molecules, polyatomic molecules effectively have only high field seeking states due to their small rotational splittings. This nearly eliminates low-field seeking electric guides and decelerators from applicability. To overcome these constraints, ingenious techniques have been fielded to align [18] [37], separate[36], and decelerate[63] larger molecules. Great progress has been made manipulating these molecules, but producing samples of very large, cold molecules at rest in the laboratory frame has remained elusive.

5.2 Buffer gas cooling of naphthalene

We create gas-phase naphthalene at 6 K through direct flow cooling, a novel rapid helium gas cooling method. Prior to this work, it was an open question whether larger molecules in a cryogenic helium gas would rapidly accumulate a layer of bound helium atoms or instead remain "naked". In the latter case the naphthalene would cool to the helium temperature but remaining free of adsorbed helium atoms. It is easy to see why clustering could be expected – the high binding energy of a helium atom to the molecule, in combination with the rich vibrational mode structure of larger molecules and the low temperature of the helium gas, could lead to the creation of long lived excited molecule-helium dimers, which would initiate clustering. The creation of 6 K naphthalene described in this work demonstrates that this is not the case, and thus greatly increases the potential scope of buffer gas cooling as a production method for cold, gas phase molecules. To our knowledge, this work represents the

first observation of cold (< 10 K), larger (> 5 atoms) molecules that are moving slowly in the laboratory rest frame. As we will describe in detail, in addition to cooling naphthalene and placing limits on the He-naphthalene clustering rate, we were also able to observe the loss of naked naphthalene due to cluster initiation from two body naphthalene-naphthalene collisions. Our studies offer evidence that rapid clustering in a cryogenic gas depends critically on the vibrational properties of the cluster constituents. A simple model suggests that our cooling methodology will be applicable to a wide variety of molecules of size comparable to (or smaller than) naphthalene.

5.2.1 Apparatus

A cold mixture of naphthalene ($C_{10}H_8$, denoted $\mathcal{N}$ in this chapter) and helium is produced by injecting a hot (300 K) mixture into a cold cell tube via a short (1 cm), thermally isolating transition tube. Our apparatus, shown in figure 5.1, is a qualitative change from the cooling system described in chapters 2 and 3. In that work, cold beams of potassium and ammonia were produced by cooling entrained mixtures with neon buffer gas and flowing the mixture through an aperture into vacuum. In this work, the beam aperture was replaced by a pumping line. The lower oven temperature and design improvements allow us to use a significantly shorter transition tube in comparison with earlier work, reducing input losses and allowing us to run with substantially lower buffer gas flows, leading to lower in-cell helium densities. These crucial changes allowed for the success of these experiments.

As described in section 4.2, the mixture begins to cool as soon as it enters the

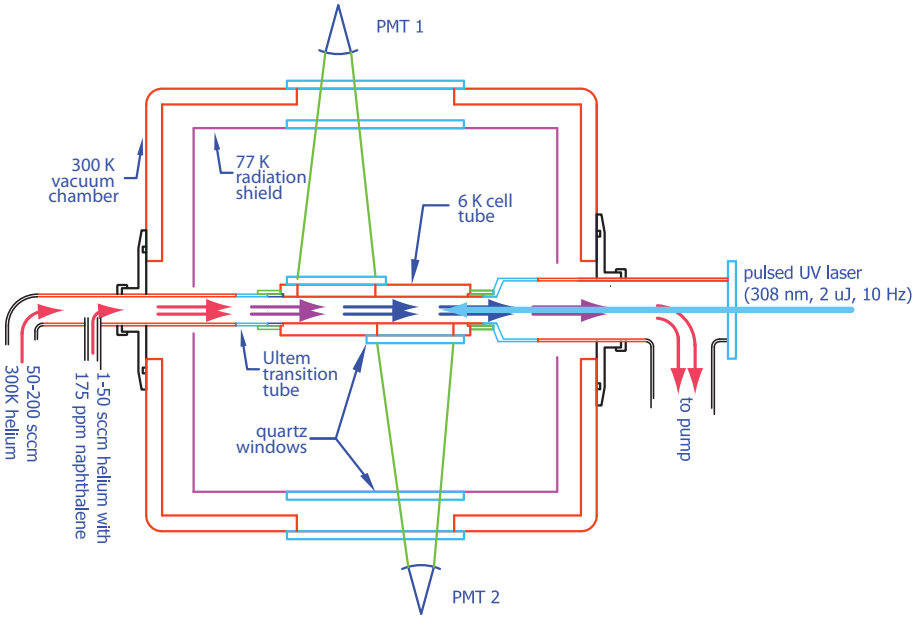

Figure 5.1: A mixture of helium buffer gas and naphthalene flows down a tube from 300 K, where the naphthalene has significant vapor pressure, to a cryogenic cell anchored to a liquid helium bath. Considerable care is taken to keep the transition region as short as possible while maintaining an adequate thermal disconnect. This is achieved by an Ultem tube, length 10 mm, wall thickness 0.5 mm, between the 300 K input tube and the cold cell tube. The cell tube is thermally anchored to the helium bath of a small cryostat; it is then connnected via a second Ultem tube to a 2 cm diameter pumping line. The total heat load on the helium bath with no buffer gas flowing is $\approx$ 500 mW, probably dominated by blackbody from the 300 K pumpout line; with a typical flow of 100 sccm of helium, this heat load increases to $\approx$ 900 mW. The helium pressure is 2 Torr at the tube input and 150 mTorr at the tube output.

cold cell tube. Any molecule which diffuses to a cold wall sticks and is lost from the gas. A species A entrained in the buffer gas will cool with little loss as long as the elastic scattering cross section $\sigma_{A-He} > \sigma_{He-He}$. Although the low temperature cross section $\sigma_{\mathcal{N}-He}$ is not known, the success of this experiment indicates that this criteria appears to be met for naphthalene, in agreement with the basic expectation that a naphthalene molecule is physically larger than a helium atom (see figure 4.9 for a more quantitative justification of this "basic expectation". As the mixture enters

the cell and thermalizes, the phase space density of naphthalene increases by more than 5 orders of magnitude. This is due to the combination of rotational cooling, translational cooling, and physical compression that takes place within the cold cell. Section 4.2 contains a detailed description of the dynamics of this system.

Cold naphthalene is detected using laser induced fluorescence, excited by a pulsed laser (10 Hz, 2 μJ, 308.0 nm) that is fired along the tube axis. The laser can be tuned across the strong 8_0^1 transition or the weaker 8_0^0 origin transition of neutral naphthalene. Fluorescence is collected through quartz windows by PMTs on each side of the cell. One PMT collects light from the upstream half of the cell, while the other only collects from the downstream half; comparison of these two spectra allows for direct measurements of loss and cooling as the gas mixture passes through the cell.

5.3 Results

A typical LIF spectrum of cold naphthalene ($n = 2 \times 10^{11}$ cm^{-3}, $T_{cell} = 6.2$ K) is shown in figure 5.2, along with a theoretical curve fit to 6.2 K $\pm$ 1.5 K. The absolute density of the naphthalene is calibrated as follows: under certain, set conditions, it is found that naphthalene loss from one end of the cell tube to the other is small. The cell tube is longer than the transition tube, and so the assumption is made that loss in the transition tube is also small. This allows us to estimate the cold density from the known input density, and the fluorescence is calibrated using this value. This calibration is checked to be consistent with a second calibration made at room temperature. In this case, the naphthalene density is known because naphthalene

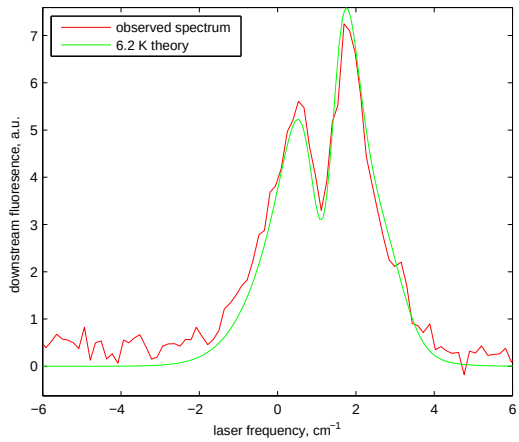

Figure 5.2: Laser induced fluorescence from cold naphthalene ($n \approx 2\times10^{11}$ cm^{-3}, $T =$ 6.2 K). Fluorescence was collected by the photomultiplier observing only the downstream (colder) half of the flow tube. The naphthalene observed here has cooled from 300 K to 6 K with minimal ($<$ factor 5) loss to the cell walls. A curve fit to $T = 6.2$ K is shown.

will not accumulate on the walls at 300 K. The helium density is calculated from the pressure, which is bounded by the measured pressures at the input and output of the flow tube.

The theory curve is a sum over many (hundreds) of asymmetric top rotational lines; hyperfine structure is ignored, but would be undetectable at this resolution. The theory is convolved with a 10 GHz laser linewidth, rendering individual rotational lines invisible. Details on this theory are found in appendix A.

We are thus able to determine the density of naphthalene and helium separately, through calibrated LIF and direct pressure measurement, respectively. We find that under typical conditions, the cell contains helium at a density of $n_{He} = 4 \times 10^{17}$ cm^{-3} and naphthalene at a density of $n_{\mathcal{N}} = 5 \times 10^{11}$ cm^{-3}, at a temperature of $T = 6.2$ K. Uncertainties in our understanding of naphthalene loss mechanisms and

of the helium pressure within the cold cell tube limit the certainty of the absolute naphthalene density measurement to an order of magnitude. The cold naphthalene is entrained in the moving helium flow, with flow velocity is $v_{flow} \approx 1.5$ m s^{-1}, compared to a microscopic thermal velocity $c = \sqrt{2k_bT/m} = 30$ m s^{-1} and typical seeded supersonic beam velocities of > 300 m s^{-1}. Figure 5.2 therefore represents $n_{\mathcal{N}}$ molecules which are effectively at rest in the lab frame.

5.3.1 Loss mechanisms

We are able to study the effects of naphthalene collisions by measuring the loss of naphthalene as it is transported through the flow tube at low velocity. Under typical running conditions, a substantial order of unity fraction of the naphthalene disappears as it is swept from the first half of the tube (upstream signal) into the second half (downstream signal). Figure 5.3 shows these signals as a function of naphthalene input flux. The loss rate rises with increasing naphthalene flux; at high input fluxes, increasing the naphthalene input actually results in a smaller downstream signal. As will be explained in detail below, this trend strongly suggests that the cold naphthalene is being consumed at low temperatures by reactions of the form

$$\mathcal{N} + \mathcal{N} \Rightarrow \mathcal{N} \cdot \mathcal{N}$$

or

$$\mathcal{N} + \mathcal{N}_n \Rightarrow \mathcal{N}_{n+1}$$

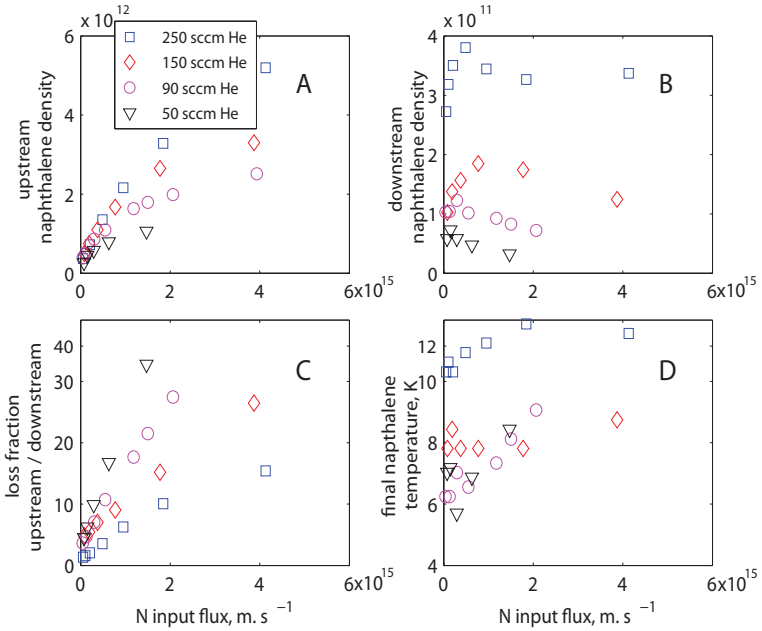

Figure 5.3: Densities and temperatures of cold naphthalene under various conditions. Most of the cold naphthalene is lost as it is swept from the tube input ('upstream', subplot A) to the tube center ('downstream', subplot B) Loss in the tube (subplot C) clearly rises with increasing naphthalene input flux. The fownstream temperature (subplot D) is in reasonable thermodynamic equilibrium with the cold (≈ 6.5 K) cell for all but the highest helium flow rates.

5.4 $\mathcal{N}$·He and $\mathcal{N} \cdot \mathcal{N}$ dimerization

Two key mechanisms for $n_{\mathcal{N}}$ loss are $\mathcal{N}$-He and $\mathcal{N}$-$\mathcal{N}$ dimerization. We see substantial evidence that $\mathcal{N}$-$\mathcal{N}$ dimerization occurs rapidly while $\mathcal{N}$-He is not observed. The different binding energies for $\mathcal{N}_2$ compared to $\mathcal{N}$-He means that substantially different physics is involved in the recombination processes, as present below.

5.4.1 $\mathcal{N}$·He

Equilibrium

The binding energy of a helium atom to $\mathcal{N}$ ($E_{He-\mathcal{N}}$) of 77 cm^{-1} [26] is much higher than the 6 K (4.2 cm^{-1}) cell temperature. In complete thermal equilibrium, the fraction of naphthalene calculated to be naked (as opposed to dressed with one or more helium atoms) is only 10^{-4} (see figure 5.5).

5.4.2 Equilibrium

Consider a gas of temperature T, with a density n_A of an impurity A and a density n_{He} of helium. Let the binding energy for $A \cdot He$ be E_{A-He}, and we will for now ignore the existence of larger complexes, $A \cdot He_n$. What fraction of the molecules A are naked?

The law of mass action [61] gives us

$$[A][He][A \cdot He]^{-1} = K(\tau) = n_{Q_A} n_{Q_{He}} n_{Q_{A \cdot He}}^{-1} e^{-(F_A + F_{He} - F_{A \cdot He})/k_b T}$$

Where $[x]$ is the concentration of species x, n_{Q_x} is the quantum density degeneracy for species x defined as

$$n_{Q_x} \equiv \left(\frac{m_x k_b T}{2\pi\hbar^2} \right)^{3/2}$$

and F_x is the internal free energy of species x. If we ignore internal degrees of freedom in the $A \cdot He$ molecule, then we have

$$F_{A \cdot He} = F_A + E_{A-He}$$

Approximating $n_{Q_A} \approx n_{Q_{A \cdot He}}$, and ignoring internal degrees of freedom in the $N \cdot He$ complex, we get

$$\frac{[A \cdot He]}{[A]} = \frac{[He]}{n_{Q_{He}}} e^{E_{A-He}/k_b T} \tag{5.1}$$

from this, we can calculate the naked fraction of species A

$$f = \frac{[A]}{[A] + [A \cdot He]} = \frac{1}{1 + \frac{[A \cdot He]}{[A]}} \tag{5.2}$$

Figure 5.4 shows this fraction plotted for naphthalene in helium at $n_{He} = 10^{17}$ cm^{-3}, using $E_{Naph-He} = 77$ cm^{-1} [110 K]. It is immediately striking that even at fairly low temperatures ($T < 10$ K), the majority of the naphthalene molecules are expected to be naked.

This initially surprising result can be most easily understood from a microscopic perspective. Imagine a 'mini-cell' containing one naphthalene molecule and one helium atom; the volume of the cell is $V = 1/n_{He}$. At 10 K, a helium atom is much more likely ($e^{k_b T/E_{Naph-He}} = e^{11} = 6 \times 10^4$ times more likely) to be bound to the naphthalene molecule than to be in any given free state. This large ratio, however, is more than offset by the even larger number of free states; for $T = 10$ K the quantum density is $n_{Q_{He}} = 4.5 \times 10^{22}$, so the number of available quantum states per helium atom is $n_{Q_{He}}/n_{He} = 4.5 \times 10^5$ for $n_{He} = 2 \times 10^{17}$ cm^{-3}. Under these conditions, most of the naphthalene at 10 K is therefore naked.

Figure 5.5 shows this fraction plotted for slightly more realistic conditions. Each naphthalene has at least 2 (one on each side), and probably 4 (one on each side of each ring), equivalent bonding sites for the helium atom[26]; this degree of freedom increases the probability of the molecule being 'dressed' by a factor of 4. In addition, figure 5.5 uses a value of $n_{He} = 4 \times 10^{17}$ cm^{-3}, which is realistic for our higher helium

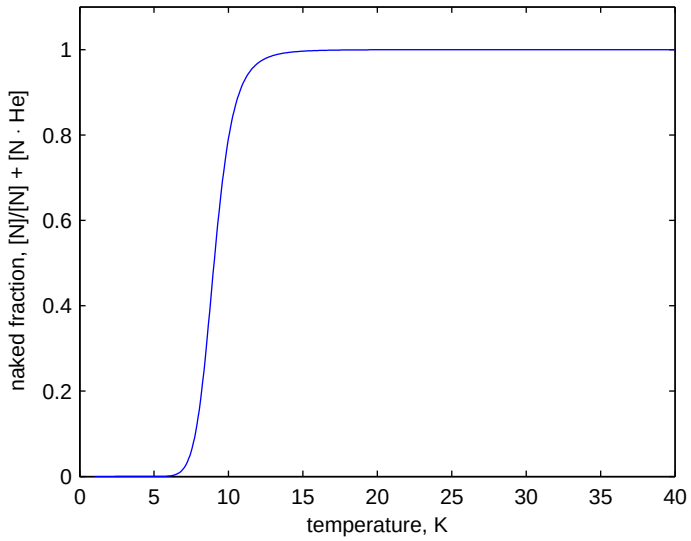

Figure 5.4: The fraction of naked naphthalene in equilibrium as a function of temperature, for a simple model with no degrees of freedom in the $N \cdot He$ complex. $n_{He} = 2 \times 10^{17}$ cm^{-3}

flows of ≈ 100 sccm.

$\mathcal{N}$·He results: the $\mathcal{N}$ is naked

We undertook a careful spectroscopic search and observed no $\mathcal{N}$·He complexes in our system. Two independent observations confirm that the naphthalene we are observing is naked. The spectroscopy of these dimers ($\mathcal{N}$·He .. $\mathcal{N}$·He$_n$, for $n = 1..15$), is known both experimentally [35] and studied theoretically [26]. The center of the 8_0^0 line in $\mathcal{N}$-He was measured in reference [35] to be shifted by 1.6 cm^{-1} to the blue (from naked $\mathcal{N}$). We recorded spectra on the origin transition and observed no peak for $\mathcal{N}$·He, putting an upper bound of 10^{-2} on the [$\mathcal{N}$·He]/[$\mathcal{N}$] fraction. Furthermore, when the helium buffer gas is replaced with neon (which binds even more strongly to naphthalene, $E_{Ne-\mathcal{N}} = 215\text{cm}^{-1}$[64]), no change in the spectrum is observed. The

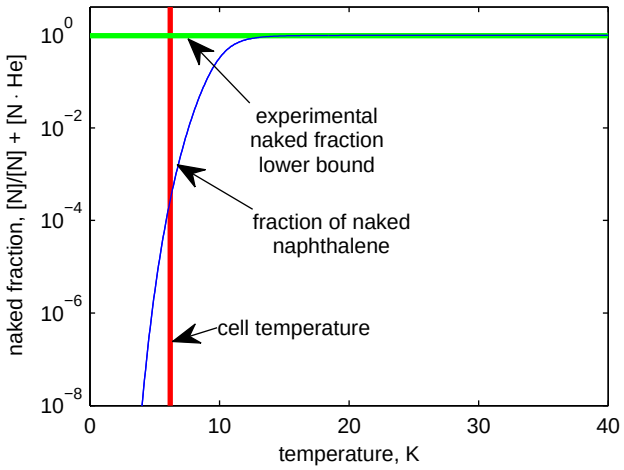

Figure 5.5: The fraction of naked naphthalene in equilibrium as a function of temperature, for a model with 4 binding sites per naphthalene molecule, for a helium density of $n_{He} = 4 \times 10^{17}$ cm^{-3} (blue curve). The vertical line shows our experimental cell temperature of $T = 6.2$ K, and the green line shows the experimental dimer fraction lower bound. No $\mathcal{N} \cdot He$ dimers were observed.

expected shift of the 8_0^1 line for adsorbed neon is about 8 cm^{-1} and would also be easily observable [105]. Due to technical constraints, experiments with neon were carried out at $T \approx 25$ K. We conclude that although we are in translational and rotational equilibrium (in both the neon and helium buffer gases), we are evidently collision rate limited in regards to $\mathcal{N}$·He cluster formation. This allows us to determine a bound on the three body formation rate of these molecules of $R_{\mathcal{N}-He-He} < 5 \times 10^{-35}\text{cm}^6 s^{-1}$

5.4.3 $\mathcal{N}$-He collisions

Conservation of energy and momentum precludes the reaction $\mathcal{N}$ + He $\Rightarrow$ $\mathcal{N}$·He from proceeding without the involvement of a third body.

Thus, the reaction must proceed either via a direct three body collision,

$\mathcal{N}$ + He + He $\Rightarrow$ He$\mathcal{N}$ + He

or via the Lindemann mechanism[75], where the reaction proceeds in two steps, each a two body collision:

$He + \mathcal{N} \Rightarrow He\mathcal{N}^*$

$He\mathcal{N}^* + He \Rightarrow He\mathcal{N} + He$

Where $He\mathcal{N}^*$ represents a quasibound complex. We consider the Lindemann mechanism first. If the complex $He\mathcal{N}^*$ lives long enough to collide with a second helium atom before it dissociates, it is possible that one of the helium atoms will remain bound to the molecule, with the second helium atom carrying away the requisite energy and momentum to drive the reaction to completion. The effective three body recombination rate is therefore expected to be proportional to the lifetime of the $He\mathcal{N}^*$ complex. This lifetime is expected, in turn, to be a strong function of the number of internal degrees of freedom available for excitation in the system.

Vibrational degrees of freedom

Figure 5.6 shows the relevant energy scales for several small and medium sized molecules. In general, three energy 'scales' are relevant when considering the reaction pathway

$He + \mathcal{N} \Rightarrow He\mathcal{N}^*$

$He\mathcal{N}^* + He \Rightarrow He\mathcal{N} + He$

where $\mathcal{N}$ could be replaced by any molecule.

These scales are:

$E_{therm} \approx k_b T$

E_{vib}, the energy of the lowest available vibrational transition in $\mathcal{N}$

$E_{\mathcal{N}-He}$, the binding energy of the first helium to $\mathcal{N}$. In order for vibrations to play a role in the formation of $\mathcal{N}$He complexes, the criteria

$$E_{vib} \lesssim E_{therm} + E_{\mathcal{N}-He} \tag{5.3}$$

must be satisfied; otherwise, there is not enough energy available in the exothermic collision to excite even the lowest vibrational level.

The binding energy $E_{X-He} \approx 100$ cm^{-1} for many molecules above a certain size; for example, the binding energy is 100 and 102 cm^{-1} for helium-tetracene and helium-pentacene complexes respectively[113]. Binding energies for various polyaromatic species with helium are listed in table 5.2. The universal energy scale is not surprising; the potential for such complexes is calculated by summing over pairwise atom-atom 12-6 Lennard-Jones potentials between the helium atom and each carbon or hydrogen of the 'substrate' molecule. The short range of the Lennard-Jones potential means that the interaction potential is dominated by the interaction with 'nearest neighbor' atoms in the substrate; this suggests, correctly, that the binding energy does not substantially increase as the substrate molecule gets larger. Helium-aromatic compounds in fact behave rather similarly to helium-graphene binding, which exhibits a similar binding energy.

Since buffer gas experiments are generally run at temperatures substantially below 100 K, $E_{therm} \ll E_{N-He}$ and equation 5.4.3 can be replaced by

$$E_{vib} \lesssim E_{N-He} \lesssim 100 \text{ cm}^{-1} \tag{5.4}$$

Chemical	Formula	Lowest vib. level (cm^{-1})	comment	reference
Benzene	C_6H_6	398		[70]
Naphthalene	$C_{10}H_8$	176		[70]
Anthracene	$C_{14}H_{10}$	89		[70]
Azulene	$C_{10}H_8$	167	Isomer of Naph; 0.8 Debye	[70]
Benzonitrile	C_6H_5CN	147	4.2 Debye	[19]
Acetamide	CH_3CONH_2	147	3.8 Debye non-aromatic	[41]
Fullerene	C_{60}	232		[60]
Fullerene	C_{70}	210		[60]
Tryptophan	$C_{11}H_{12}N_2O_2$	46		[115]

Table 5.1: The lowest vibrational level of various 'larger' molecules. All except tryptophan satisfy the approximate criteria of 5.4, although anthracene is an intermediate case that barely passes this litmus test. It is also notable that of the ≈ 200 'small' ($N_{atom} \leq 5$) molecules with vibrational spectra listed in the *Handbook of Chemistry and Physics*[28], only 5 have vibrational modes of less than 100 cm^{-1}, and none have modes below 70 cm^{-1} (100 K) Tryptophan has a long, floppy "string" of atoms that exhibits floppy, low-frequency torsional modes.

Chemical	formula	Helium	Neon	Argon	Krypton	Dipole (D)	cite
Benzene	C_6H_6	64	200	400	440	0	[73][73]
Naphthalene	$C_{10}H_8$	77	215	–	–	0	[26]
Anthracene	$C_{14}H_{10}$	–	220	460	620	0	[64]
Tetracene	$C_{18}H_{12}$	100	248	–	–	0	[66]
Azulene	$C_{10}H_8$	–	265	567	683	0.8 Debye	[1]

Table 5.2: The binding energies in cm^{-1} of various aromatic molecules to nobel gas atoms. In some cases the helium binding energy is not known, but as can be seen from the data, in these cases the neon binding energy is a good indicator of the expected helium binding energy. For comparison, the helium binding energy to an infinite graphene sheet is about 104 cm^{-1}[43]; graphene could be thought of as the end point of the Benzine-Naphthalene-Anthracene-Tetracene series.

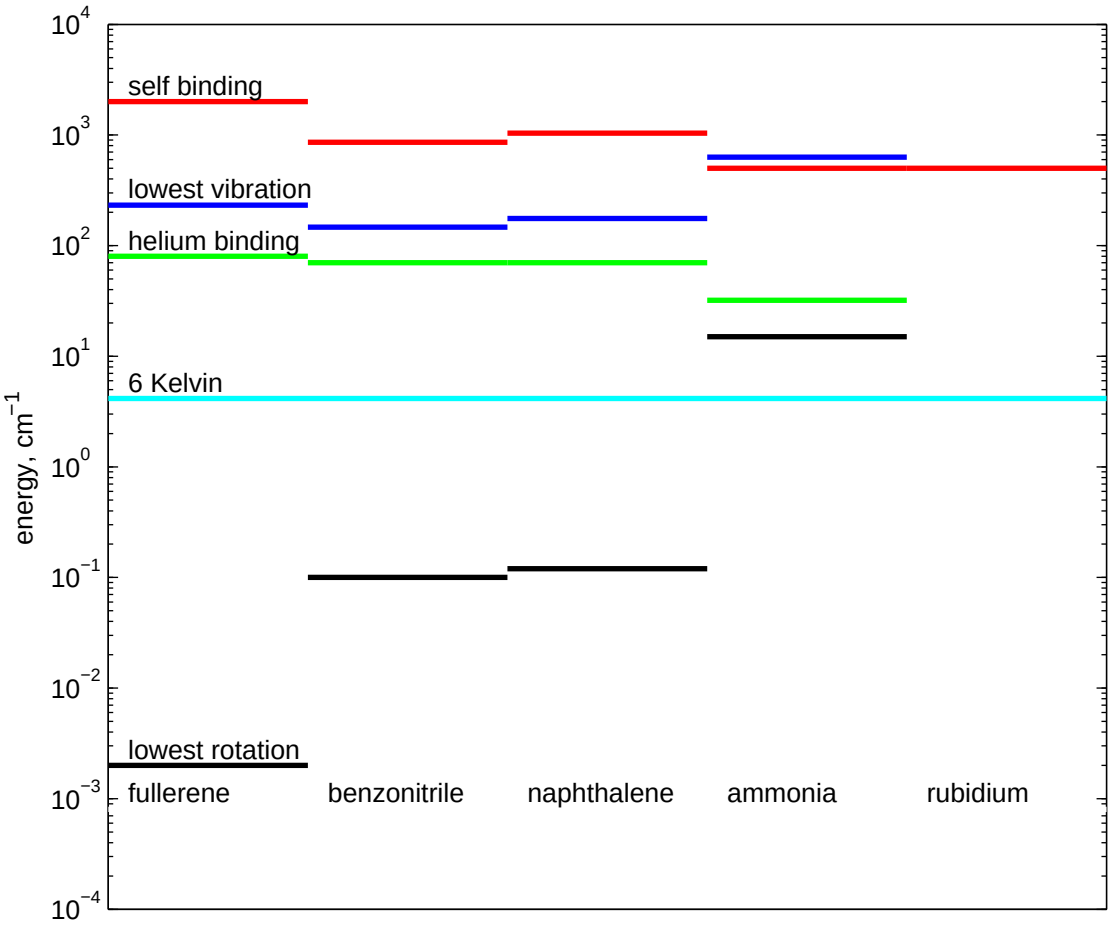

Figure 5.6: Relevant energy scales for various candidates for direct flow buffer gas cooling. The criteria of equation 5.4.3 requires that the helium binding energy (green line) summed with the temperature (cyan line) is lower than the lowest vibrational level (red line). Binding energies for C_{60}-helium are not known, but are unlikely to differ greatly from graphene ($\approx$ 150 K). Note that for every large molecule, the self-binding energy (red line) is substantially larger than the lowest vibration level, suggesting that the $\mathcal{N} \Rightarrow \mathcal{N}_2$ reaction is likely to proceed rapidly via effectively two body processes. References are listed in tables 5.1 and 5.2.

As illustrated in figure 5.6, this criteria is not met even for moderately large molecules. Vibrational degrees of freedom *within* the molecule are therefore generally

irrelevant for 'small' aromatic molecules in a cold helium buffer gas.

Rotational degrees of Freedom

Figure 5.6 clearly shows that there is sufficient energy available in a collision to excite many *rotational* degrees of freedom in the $\mathcal{N}$He* complex. Are these degrees of freedom relevant in the reaction He + $\mathcal{N} \Rightarrow$ He$\mathcal{N}$*?

Consider the situation immediately prior to the collision. The system of He + $\mathcal{N}$ has a certain J and m_J in the laboratory frame. After the collision, the quasibound complex He$\mathcal{N}$* must have the same J and m_J due to conservation of angular momentum. There is therefore only one available rotational channel for the reaction. The value of J will set the height of the centrifugal pseudopotential in the collision, but the degeneracy of the channel is no greater than it would be if $\mathcal{N}$ were an atom. The J and m_J degrees of freedom are therefore also not relevant in the Lindemann process. [1]

Generality of the process

Our model suggests that it is the lowest vibrational mode v_{min} and the helium binding energy E_{He-X}, that are relevant when estimating Lindemann mechanism three body rates. For example, C_{60} is a large but exceptionally stiff molecule (v_{min} = 232 cm^{-1}), while the amino acid tryptophan ($C_{11}H_{12}N_2O_2$) is not much larger than

[1] 'Rotational degrees of freedom are not relevant'...: This is *not* true if the He atom and the N molecule are allowed to rotate *independently* of each other; in this case, the relative rotation would provide an additional unconstrained degree of freedom. Such an exciplex is difficult to visualize - the helium atom would be orbiting the molecule - but is not entirely unreasonable; indeed, for large clusters $\mathcal{N}$·He$_n$ for $n > 15$, such 'superfluid' behavior has indeed been observed. Nevertheless, to our knowledge such exotic complexes have never been observed.

naphthalene, but contains low frequency torsional modes ($v_{min} = 46$ cm^{-1})[115]. Our model would therefore suggest that C_{60} and other "stiff" molecules listed in table 5.1 could be cooled using this technique, but tryptophan could not.

Direct three body recombination

The conclusions above suggest that helium dimerization will proceed slowly in the $\mathcal{N}$-He system are based on the Lindemann model of dimerization. We now turn to direct three body recombination processes that produce $\mathcal{N}\cdot\mathrm{He}_n$ clusters. In general, this mechanism in van der Waals complexes are poorly understood. In particular, for neutral particles these reactions have been observed only in the relatively uncontrolled conditions of a seeded supersonic jet. Simulations of these jets (see section 5.4.4 below) suggest that the $\mathcal{N}$-He-He rate is on the order of $R_{\mathcal{N}-He-He} = 3 \times 10^{-35} cm^6 s^{-1}$. We can compare this rate constant to other systems. For example, the strong chemical oxygen reaction O + O + O $\Rightarrow$ O_2 + O) at 300 K has a much higher rate constant of sim 10^{-33}cm$^6 s^{-1}$.

The group of Kaneko et al [62] have observed the formation of rare gas ion - helium clusters (for example, $Ar^+\cdot He_n$), in cold helium gas ($n_{He} = 8 \times 10^{16}$ cm^{-3} $T = 4.4K$), via the Lindemann mechanism. They conclude that the net reaction Ar^+He_n + He + He $\Rightarrow$ Ar^+He_{n+1} + He is suppressed in small clusters due to the short lifetime of the intermediate state Ne^+He_{n+1}*. This is one of the few studies of three body recombination processes done at low temperature, but the 170 cm^{-1} binding energy of $Ar^+\cdot$He and the lack of vibrational modes in this atomic system makes the applicability to the $\mathcal{N}$-He system questionable.

In our study, we observe no helium dimers even at our lowest temperatures (T = 6 K $n_{He} = 4 \times 10^{17}\text{cm}^{-3}$), putting an experimental upper bound on the rate at $R_{\mathcal{N}-He-He} < 5\times10^{-35}\text{cm}^6 s^{-1}$, consistent with the results of experiments in supersonic jets.

5.4.4 Three body rates from supersonic nozzles

Three body recombination rates for van der waals complex formation such as

$$\mathcal{N} + He + He => \mathcal{N} \cdot He + He$$

are in general rather poorly quantified. To my knowledge, these reactions have only been observed in supersonic jets; such systems are not ideal for quantitative rate measurements, as both helium density and temperature drop rapidly as the mixture expands away from the nozzle.

Figure 5.7 shows the results of a rather simple simulation of a supersonic nozzle, with simulated conditions set to those of reference [35] where "as much as 15% of the bare molecules were dressed with helium atoms". The stagnation pressure of helium in these experiments is quite high at 120 bar; at 'typical' supersonic jet stagnation pressures of a few bar, no $\mathcal{N}\cdot$He complexes are observed. The conditions in reference [35], which was specifically studying $\mathcal{N}\cdot\text{He}_n$, are typical of supersonic jet experiments looking at van der waals complexes of helium with larger molecules; this is not surprising, since the van der waals binding energy E_{he-X} in general does not greatly vary. The nozzle diameter in these experiments is 200 microns.

For this simulation, the density in the supersonic expansion is assumed to follow

$$n = n_0 \frac{r_{noz}^2}{1 + r^2}$$

Where n_0 is the stagnation helium density, r is the distance 'downstream' from the nozzle, and r_{noz} is the nozzle diameter. The temperature is assumed to follow a perfect adiabatic expansion for a monatomic gas,

$$T = T_0 \left(\frac{n}{n_0} \right)^{\frac{2}{3}}$$

This assumption is invalid at very low densities, where the expansion 'freezes out', and there are not enough collisions to provide further cooling. Typically this freeze-out temperature is on the order of a few K; by this point, the three body recombination rate is effectively zero in any case, as can be seen in figure 5.7d. The temperature at the end of this simulation is 9 K.

As the mixture expands and cools, the fraction of naphthalene molecules that would be naked in equilibrium (equation 5.2) drops. This fraction is shown in figure 5.7c. At some point (1.1 mm from the nozzle in the simulation), the mixture becomes supersaturated - that is, the equilibrium fraction $\frac{[N \cdot He]}{[N]}$ becomes non-negligible. Three body recombination at a constant rate ($k = 4.5 \times 10^{-35}$ cm^{6}s^{-1}) is assumed to begin at this point. Note that the mixture has been "supersaturated" from the point of $\mathcal{N}$-$\mathcal{N}$ collisions for most of the expansion - certainly for all temperatures < 50 K ($E_{\mathcal{N}-\mathcal{N}} = 1400$ K).

The calculated three body rate as a function of helium density is shown in figure 5.7d. The rate drops rapidly as the beam continues to expand away from the nozzle.

This rate is integrated to calculate the ultimate fraction of naphthalene that ends up in $\mathcal{N}$·He dimers (figure 5.8).

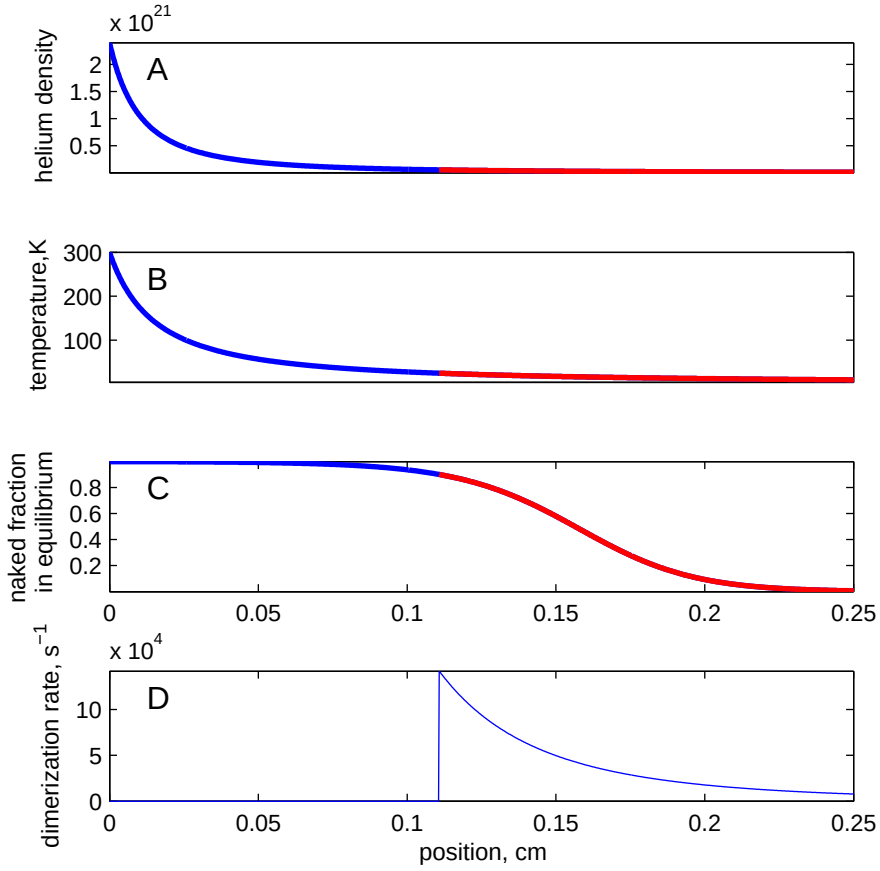

Figure 5.7: Simulation of a simple supersonic nozzle, with conditions taken from reference [35]. The x axis shows distance from the 200 μm diameter nozzle. (A) helium density, cm^{-3}. (B) helium temperature (C) the fraction of entrained naphthalene that would be naked if the beam were in perfect equilibrium (equation 5.2). In (A), (B), and (C), the portion of the expansion that is supersaturated (where the naphthalene "wants" to be dressed with helium atoms) is shown in red. (D) shows the dimerization rate, in s^{-1}, somewhat naively assuming a threebody recombination rate of 4.5 $\times 10^{-35}$ cm^{6}s^{-1} that is independent of temperature. This rate is "turned on" once the mixture is supersaturated (red portion of curves).

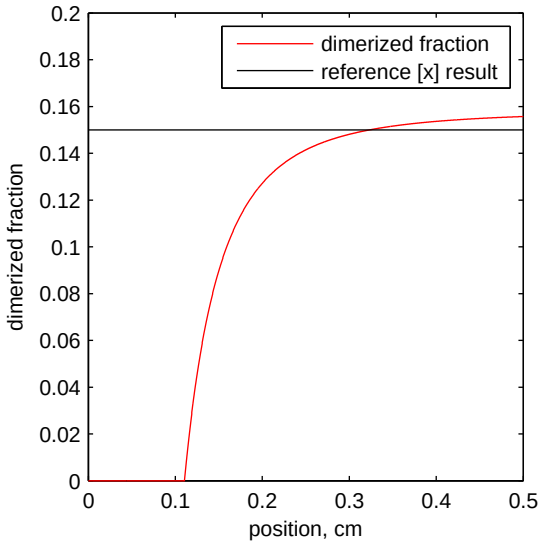

Figure 5.8: Integrated dimerization rate from figure 5.7D. The extracted three body recombination rate r is found by adjusting r until the final dimerized fraction agrees with the '15 %' measured in reference [35]

Limitations of the model

The extracted rate of $R_{\mathcal{N}-He-He} = 4.5 \times 10^{-35}$ cm^{6}s^{-1} should be viewed with significant skepticism. The assumption of perfect adiabatic expansion in the nozzle is impossible to verify, and the assumption that R is independent of temperature once the mixture is supersaturated is dubious at best. In addition, in the simulation the three body rate is arbitrarily "turned on" when 10% of the naphthalene would be dressed with helium atoms. If this is changed to 50% - perhaps an equally plausible estimate - the extracted rate $R_{\mathcal{N}-He-He}$ increases by a factor of 3. These limitations in fact highlight the fundamental difficulties encountered when attempting to measure three body recombination rates in an expanding supersonic jet.

5.4.5 $\mathcal{N}$-$\mathcal{N}$ collisions

Unlike $\mathcal{N}$·He collisions, the binding energy of $E_{\mathcal{N}-\mathcal{N}}$, 1008 cm^{-1} [39], is much larger than a typical naphthalene vibrational mode spacing of ~ 300 cm^{-1}. In addition, the $\mathcal{N}_2$ dimer has a rich internal vibrational spectrum[110], with a typical mode spacing for the complex of ~ 20 cm^{-1}. This suggests that the $\mathcal{N} + \mathcal{N} + \mathrm{He} \rightarrow \mathcal{N}_2 + \mathrm{He}$ reaction is likely to proceed via effective two body processes:

$\mathcal{N} + \mathcal{N} \Rightarrow \mathcal{N}_2{}^*$

$\mathcal{N}_2{}^* + \mathrm{He} \Rightarrow \mathcal{N}_2{}^* + \mathrm{He}$

We see strong evidence of this proposed two body loss from the cold sample. We further observe that this loss does not depend helium density and thus conclude that the lifetime of a $\mathcal{N}_2{}^*$ is substantially longer than the $\sim 10^{-8}$ seconds between helium collisions. Although direct observation of the expected $\mathcal{N}_2$ would be an ideal diagnostic of this process, The $\mathcal{N}_2$ dimer exhibits many geometrically distinct isomers and has an extremely broad spectral signal. In the future, detection of the $\mathcal{N}_3$ trimer, which has narrow lines, should be possible.

A simple model of loss initiatied by $\mathcal{N}$-$\mathcal{N}$ dimerization neatly explains all of our data on $\mathcal{N}$ loss. This model contains a single inelastic two body rate constant k_2, which characterizes all inelastic two body processes, and a single one body loss rate k_1 which characterizes one body diffusion to the cell wall. If $[\mathcal{N}]$ is the density of naphthalene and $[\mathcal{M}]$ is the density of all dimers $\mathcal{N}_n$, this model can be written

$$[\dot{\mathcal{N}}] = -k_2[\mathcal{N}]^2 - k_2[\mathcal{N}][\mathcal{M}] - k_1[\mathcal{N}]$$

$$[\dot{\mathcal{M}}] = k_2[\mathcal{N}]^2 - k_2[\mathcal{M}]^2 - k_1[\mathcal{M}]$$

Although this model fits our data well, each reaction $\mathcal{N}_x + \mathcal{N}_y \Rightarrow \mathcal{N}_{x+y}$ must proceed at a unique rate, and the diffusion cross sections of $\mathcal{N}_x$ in helium will also vary. Nevertheless, the qualitative fit to the data, shown in figure 5.9, is good over a wide range of naphthalene and helium input fluxes. Our model suggests that under typical conditions, about 25% of the naphthalene input flux remains in gas phase at the point in the flow where the mixture has thermalized with the cold cell. The rest is lost, frozen on the cell and transition tube walls. This high efficiency of cooling is very likely not unique, as it depends only on the general cross section criteria $\sigma_{\mathcal{N}-He} > \sigma_{He-He}$ outlined in section 4.2.

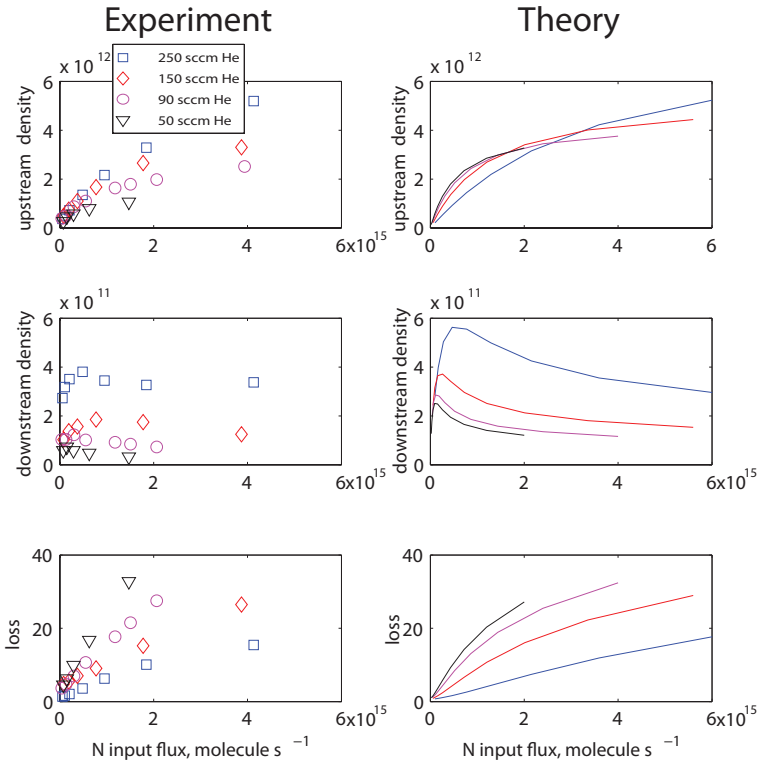

Figure 5.9: The data from figure 5.3 (left hand plots) fit to a model that includes both two body loss and diffusion to the cell walls before and during the cell tube (right hand plots). This model has two free parameters, $\sigma_{\mathcal{N}-\mathcal{N}}$ and $\sigma_{\mathcal{N}-He}$.

5.5 Conclusion

Cold naphthalene has been produced in a 6 K vapor cell by rapidly cooling a warm mixture of helium and naphthalene. As the mixture cools, the phase space density of the naphthalene increases by more than five orders of magnitude, producing naphthalene at a 2×10^{11} cm^{-3} density, 6.2 K, and moving at a flow velocity of 1.5 m s^{-1}. The samples remain in the cell for ≈ 50 msec, with typical loss dominated by the naphthalene-naphthalene dimerization reaction. The method is expected to be applicable to a wide class of molecules.

Chapter 6

Applications

Great effort has been taken to keep the techniques demonstrated in this thesis as general as possible. In the abstract, a system has been demonstrated that can bring high fluxes of an almost arbitrary species to temperatures of a few kelvin; and most critically, to temperatures where the interaction energy $\mu \cdot B$ or $E \cdot D \gtrsim k_b T$.

In this final chapter, I outline several possible experiments that could be done using the techniques from chapters 2-5. These experiments access hitherto unrealizable physical systems and in some cases have potentially important applications outside of AMO physics. Of particular note are section 6.1, describing a general, broad spectrum "nose" that rapidly resolves complex gas mixtures at an unprecedented level, and section 6.5.2, presenting a synthesis of many of the techniques demonstrated in this thesis to continuously load a high flux of molecules into a trap.

6.1 Mixture analysis

6.1.1 Background

The accurate and sensitive analysis of complicated gas mixtures has many applications in industry, biology, medicine, and environmental science. Examples of unsolved, or imperfectly solved, problems are easy to find: over 1000 compounds are known to exist in human breath, including compounds which are markers of health risks, cancer, and environmental hazards[98]; a wide variety and organic amines and carboxylic acids, present in nanomolar concentrations in seawater, are important intermediates in decomposition processes and provide a quantitative measure of marine ecosystem metabolic cycles[114]; the pheromones of butterflies and moths consist of (at least) hundreds of different compounds, many of them isomers differing only by the position of a double bond[17]; and human blood and urine contain at least dozens and likely hundreds of biologically important hormones. Each of these mixtures is at best partially resolved by current state of the art gas chromotography/mass spectrometry methods.

As an example, figure 6.1 shows an analysis of volatile chemicals found in mouse urine. Although dozens of chemicals were identified and measured, a glance at this figure strongly suggests that there are probably many more unidentified chemicals unresolved in this GC/MS experiment.

The current state of the art techniques for analyzing complex gas mixtures are ion mobility spectrometry, gas chromatography, and gas chromatography mass spectrometry (GS/MS). In gas chromatography (which is also an essential part of the

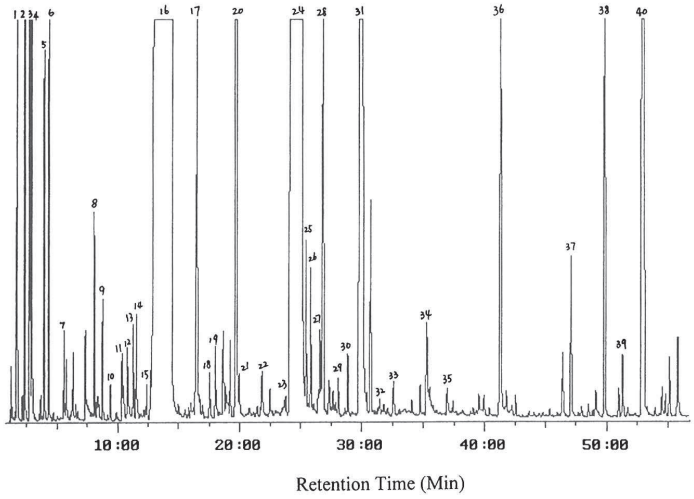

Figure 6.1: A gas chromotography/mass spectrometry analysis of mouse urine. Each of the labeled peaks was identified via mass spectrometry. The identity of each of the peaks shown was identified using ionization mass spectrometry. These peaks represent volatile chemicals of both known and unknown biological significance. The trace strongly suggests that unidentified chemicals exist at lower concentrations.

technique proposed here), a gas sample to be analyzed is mixed with an inert carrier gas - typically helium or nitrogen - and flowed through a capillary containing a liquid or polymer coated substrate. Different contaminants elute at different times, effectively sorting the contaminants by time as they come out the end of the capillary "column" [1]. Gas chromatography alone can resolve mixture components with fraction as low as 10^{-9} (ppb range) in specialized cases, but generally operates in the 10^{-6} range or lower. For this reason, it is often combined with mass spectrometry (GS/MS) to further resolve mixture components. In this case the molecules are ionized as they elute from the column and detected by a mass spectrometer; the combination of elution time and charge to mass ratio often serves to uniquely identify the

[1] named for historical reasons, derived from the fractioning column used in distillation

mixture component. Ion mobility spectrometry, where the sample is ionized and then drifted through a stationary gas in an electric field, is significantly more sensitive, and is the industry standard when there are a small number of very dilute targets of interest (as is the case, for example, in bomb sniffing)

These technologies are attractive solutions for analyzing even very dilute "simple" mixtures with a few components, but struggle when analyzing a complex, unknown solution with hundreds or thousands of components. GS/MS struggles especially to resolve mixtures of chemically similar isomers. In this case the mass spectrometer cannot discriminate between species, and this is compounded by the fact that the gas chromotography column tends to elute similar species at nearly the same rate. As an additional disadvantage, each type of chromatography column needs to be calibrated for each analyte being studied - an acceptable practice for 10 or even 100 possibilities, but unworkable when studying unidentified goo.

Direct spectroscopic analysis of gas-phase samples in the UV is ineffective at resolving complex mixtures. Nearly all molecules have strong transitions between 200 and 400 nm; however, distinguishing between trace impurities in gas samples using these transitions at room temperature is all but impossible, since the spectra, typically made up of thousands of unresolved rotational lines[2], are typically broadened by 100s or 1000s of wavenumbers; the "confusion limit", where the spectrum of one mixture component overlaps another, is reached almost immediately. This is especially true in the common case when several components have very different partial pressures; in

[2]These lines *can* be resolved in UV at room temperature for small species with large rotational splittings, such as hydrides and NH_3, but this is impossible for all but the most trivial organic compounds

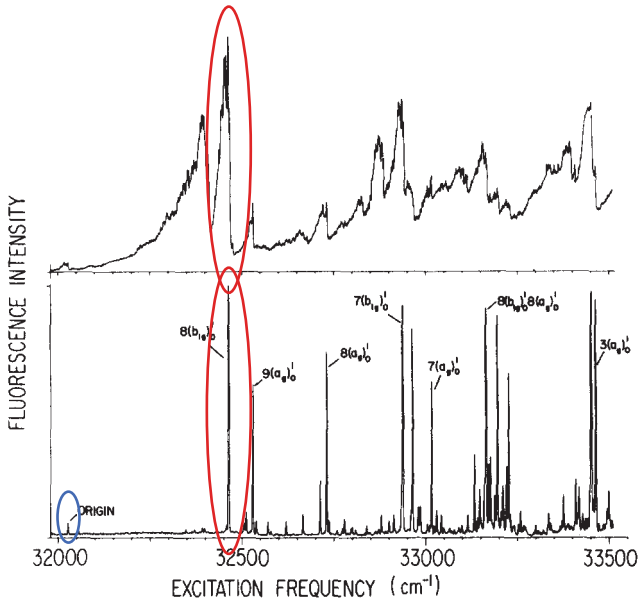

Figure 6.2: Reprinted from reference [5]. Experimental naphthalene spectra taken at 300 K (top) and in a supersonic jet at 2 K (bottom). Even the narrow features in the lower trace are in fact resolvable into individual rotational lines, as shown in figure 6.3. The spectrum shown in figure 5.2 is taken on the strong 8_0^1 transition (circled in orange); data was also taken on the weaker 8_0^0 transition (circled in blue). The advantage of cooling from the point of view of mixture analysis is obvious.

this case the spectrum of a trace component can easily be lost in the tail of another, more common component.

This "confusion limit" is radically suppressed at low temperatures, where not only are rotational manifolds much narrower and hot vibrational bands suppressed, but in many cases individual rotational lines can be resolved. Figure 6.2 shows experimental naphthalene spectra at 300 and 2 K, from reference [5]. Figure 6.3 shows theoretical spectra for the 8_0^1 line of neutral naphthalene (circled in figure 6.2) at 300, 77 and 4K; only at the lowest temperature can rotational lines be resolved.

This problem is reduced in the near-IR, where doppler broadening is significantly smaller. At these wavelengths, individual rotational lines of moderately sized

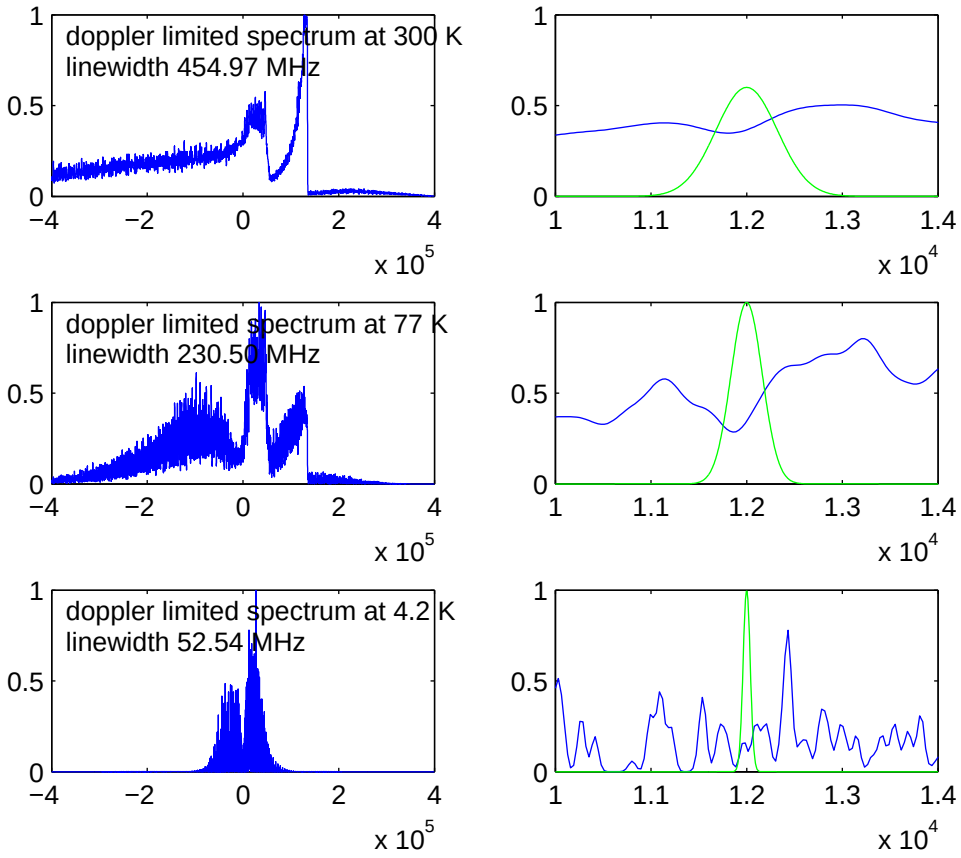

Figure 6.3: theoretical 8_0^1 spectra naphthalene at 300, 77 and 4 K; the left hand plots show the entire vibrational line, while the right hand plots show a central region 15 GHz wide. A doppler-limited single line is shown in green on each plot for comparison. Only in the 4 K spectra are the majority of the rotational lines resolved; at higher temperatures, the spectral structure is composed of manifolds of rotational lines. The advantages of cooling, both for signal size and spectrum simplicity, are self evident.

molecules can be resolved even at room temperature, which at least in principle allows for the resolution of complex, overlapping spectra. Thorpe and Ye [98] have developed extremely sensitive, accurate, and broadband absorbtion spectrometers in this spectral region, using a frequency comb to probe the region between 1.5 and 1.7 microns. Figure 6.4 shows a typical absorbtion spectrum of human breath taken on

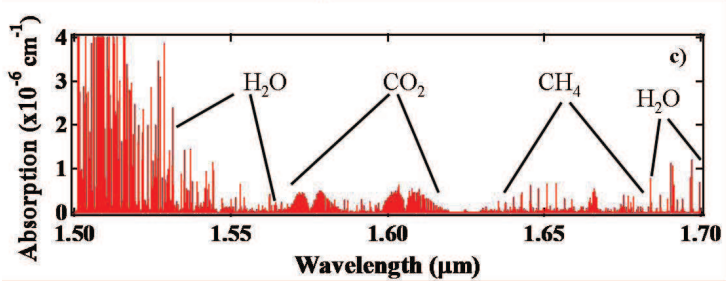

Figure 6.4: reprinted from [98]. The rotationally resolved IR spectrum of a complex gas mixture - in this case human breath at 300 K and atmospheric pressure. The concentrations of polar mixture components are resolved at the ten parts per billion level.

this device. This detection method can detect mixture components in the 10^{-8} range, and has the advantage over gas chromatography of analyzing thousands of channels simultaneously.

Working in the IR reduces doppler broadening, but comes with significant disadvantages. Near IR transitions tend to be high harmonics of vibrational transitions, and as such are rather weak; they only exist for polar molecules; and they tend to exist only for rather small molecules with high vibrational frequencies.

Seeded supersonic jets, combined with capillary gas chromatography, have already been demonstrated as powerful tools for analyzing mixtures; an excellent review is found in reference [57]. In reference [93], a gas chromatography capillary is inserted directly into a supersonic nozzle; the cooled output in the beam is detected via laser

induced fluorescence 50 nozzle diameters (1 cm) downstream from the nozzle. Despite the low density and short interaction times in the jet, this work could resolve as little as 50 pg (3×10^{11} molecules) of naphthalene as a contaminant in unleaded gasoline, corresponding to an input fraction in the 10 ppb range. However, the low densities and short interaction times in supersonic jets severely limit the sensitivities of these experiments. This is especially true if rotational lines need to be resolved; in this case, the high forward velocity ($\approx$ 300 m s^{-1}) of the beam requires the beam to be severely collimated[68].

6.1.2 Direct flow loading as a mixture analyzer

Figure 6.5 shows a proposed combination of a capillary gas chromatograph and a direct flow buffer gas cell. The mixture is first separated into coarse components by a chromatography stack at room temperature or higher, and then loaded into a cold cell via direct gas flow. When the principle components (e.g. N_2 or O_2 in an air mixture) are eluted from the stack, they can be partially or completely redirected into a dump, preventing the system from being overloaded and icing up. Typical gas chromatographs can completely resolve a 1 cm^3 gas sample in a few minutes, and elute the entire gas fraction of a given chemical in about 10 seconds. Given a few second elution time and an in-cell residence time of 0.5 seconds, the density of a given component at 4 K is about one order of magnitude lower than the corresponding density in the 300 K sample, with dramatically (10^4 times) higher phase space density. Helium is routinely used as the moving phase carrier in gas chromatography, at flow rates (20 sccm typical) entirely compatible with direct gas flow loading. It is worth

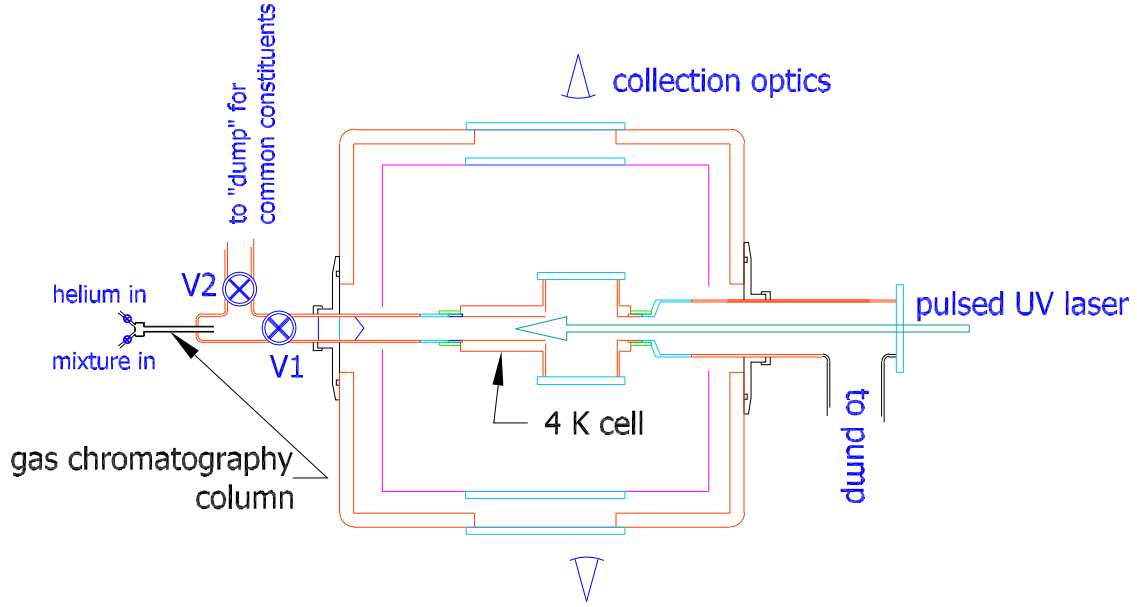

Figure 6.5: A proposed mixture analyzer based on a synthesis of this work and reference [93], which demonstrates mixture analysis via seeded supersonic jets. An unknown mixture M is loaded at atmospheric pressure and 300 K or above into the input headspace of a chromatography column. Ultrapure helium is used as the moving phase in the column, bleeding the mixture over the course of a few minutes into the main apparatus. This coarsely separates the mixture into several dozen time "channels", and critically separates trace components from bulk components, e.g. N_2 or or O_2 in an air sample. Judicious timing of valves V1 and V2 can be used to redirect bulk components into a dump. The mixture is then loaded via direct gas flow into a cold cell, and detected via LIF as in chapter 5. The longer interaction times and higher density in the cell, as compared to a supersonic jet, suggest that this method is as much as 10^4 times more sensitive than [93], and could detect mixture components at the 10^{-13} level.

noting that these experiments can be done with the chromatography stack as hot as 500 K, greatly increasing the range of possible analytes[3].

As in reference [93], this technique is taking maximal advantage of the generality of the direct flow cooling technique; we are relying on the technique working on

[3]gas chromatography stacks typically run at about 500 K; this is entirely compatible with the existing apparatus.

every resolvable mixture component. Section 6.1.4 below discusses the limitations and possible workarounds this will put on the technique.

A numerical example further illustrates this proposal. Consider the breath of a graduate student who has recently returned from lunch, comprised predominantly of N_2, O_2 and CO_2, but also containing a 10^{-11} fraction of monosodium glutamate, $C_5H_8NNaO_4$. 1 cm^3 of this breath is loaded into the device, and allowed to elute through the chromatography column. Over the $\sim$ 1 second that the MSG is emerging from the column, it is accompanied by about 1 ppm air, due to imperfect separation in the column; during this second, 10^8 MSG molecules and 10^{13} air molecules emerge from the column. This mixture is loaded via direct gas flow into a cold cell, with a volume of $\sim$ 10 cm^3 and a temperature of $\sim$ 5 K. The densities in this cell are $n_{MSG} = 10^7$ cm^{-3}, $n_{air} = 10^{12}$ cm^{-3}, and $n_{He} = 10^{17}$ cm^{-3}. This mixture will (barely) not precipitate, due to the low overall contaminant density, but the MSG can be detected via LIF: a 10 GHz wide 1 μJ laser pulse will excite $\sim$30% of the MSG molecules; total collection optics efficiencies of a modest 10^{-3} still lead to $\sim$3000 PMT counts.

6.1.3 Proposed synthesis with a broadband absorbtion spectrometer

Figure 6.6 shows a proposed synthesis of this system with a UV version of the spectrometer developed by Ye et. al. and Mbele et. al.[98][31]. The fluorescence spectroscopy has now been replaced by high-Q cavity absorbtion setup, with low dispersion supermirrors as described in [98]. Each tooth of the frequency comb is im-

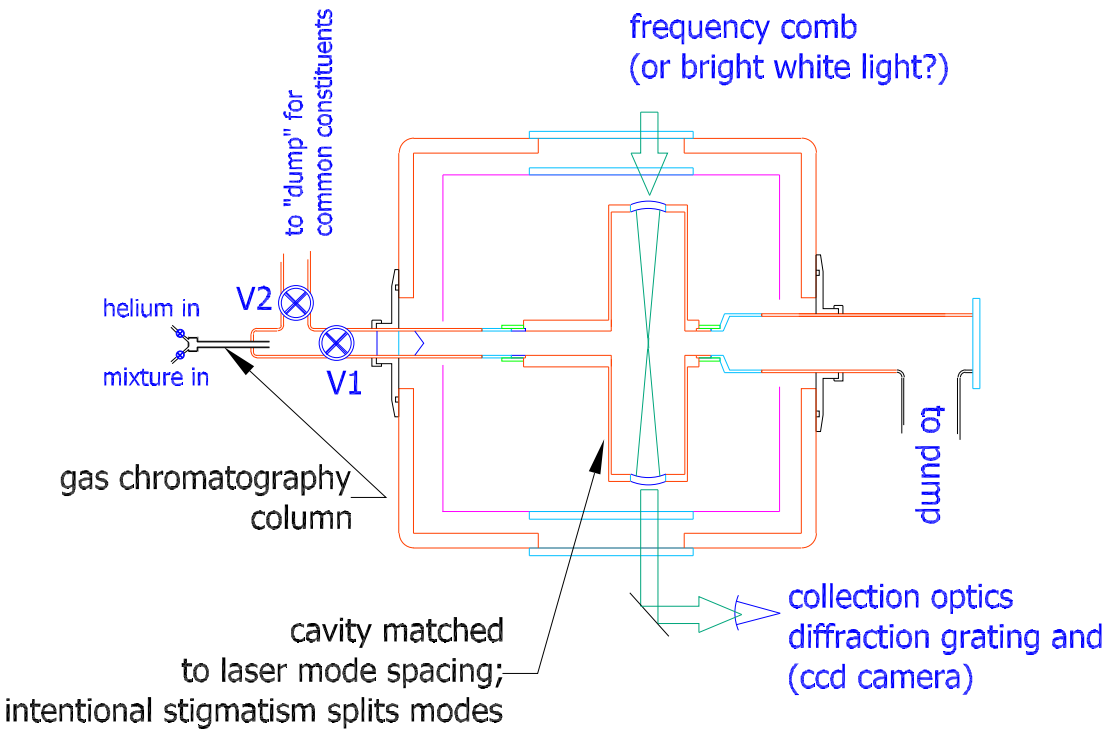

Figure 6.6: The proposal of figure 6.5 with the fluorescence spectroscopy replaced with a wideband absorbtion spectrometer, following reference [98]. A large portion of the near UV spectrum could now be recorded at once, effectively resolving complex mixtures at the ppb level in a few minutes.

aged onto a separate area of a two dimensional CCD array via a virtual phased array (VIPA) disperser, following references [31] and [89]. This allows the experimenter to take full advantage of high-bandwidth off the shelf data acquisition systems developed for video acquisition. The absorbtion of each tooth of the comb can be independently and simultaneously recorded. This system will be less sensitive than an ideal fluorescence setup as in figure 6.5, but can analyze the entire spectrum of the mixture in a single shot, simultaneously resolving and identifying thousands of components of an unknown mixture. This would be especially important when large quantities of the mixture are unavailable, as might easily be the case for biological samples.

The sensitivity of this system will be comparable or slightly better than the 300 K, 1 bar version demonstrated by Ye et. al.[4]; the principal advantages are a far lower "confusion limit", and the sensitivity to essentially all molecular species rather than small, polar species.

The complete system would be able to rapidly resolve fractional densities down to the 100 part per trillion range of thousands of chemicals at once. [5] The "confusion limit" that plagues complex mixture analysis would be virtually eliminated.

White light sources

It is notable that the frequency comb in figure 6.6 and reference [98] is being applied in a very crude way - coherence between the teeth of the comb is not being used at all. This raises the possibility of using an incoherent, bright white light source in the place of the expensive UV frequency comb. The cavity itself would now "select" the frequency components of the light source, which would still be imaged onto a CCD array via a VIPA (virtual phased array) spectral disperser[31]. Mixtures in supersonic jets have in fact been effectively analyzed using a bright xenon lamp as the excitation light source[56], although to my knowledge cavity enhanced absorbtion spectroscopy coupled with a VIPA disperser has not been demonstrated with white light.

---

[4] "..the sensitivity of this system will be comparable..": A number of factors cancel in this calculation: compared to Ye's work in reference [98], this system has 10 times smaller n and 100 times smaller L; this is offset by 100 times lower T (resulting in perhaps $\sim$ 40 times lower spectral width) and transition matrix elements 10-100 times stronger. Imaging detectors in the UV are substantially better than IR-sensitive detectors

[5] For comparison, the current LIF system, with far from ideal optical access, is about 1000 times less sensitive than this, and can analyze only one component at once

The light source in this proposal would need to be extremely bright; only a single spatial mode is usable, and, unlike comb-based spectrometers, the majority of the light would be wasted, as it would not couple to a mode of the cavity. A typical 100 watt xenon arc lamp (e.g. Hamamatsu L10878), with an arc length of 1 mm, would result in only a tiny fraction - 10^{-8} or 1 microwatt - being coupled to the cavity, as opposed to 40 mWatt in the case of Ye et. al.[98]. The minimal detectable absorbtion in the shot-noise limit scales as $\phi^{-1/2}$, so degradation this would result 100 times lower sensitivity than the ideal frequency comb case based on Ye's 40 mWatt comb. Nevertheless, the enormous reduction in system complexity makes this a tempting option. With a white light source, the entire system contains no component more expensive than the dewar itself, and could be assembled for less than $50 K.

A white light source also significantly lightens the constraints on the cavity performance. Most importantly, a slight chromaticity in the cavity can now be tolerated - even if the frequencies of the cavity modes are not exactly evenly spaced, they can be expected to be stable, and can be compensated for. In contrast, the exact modes of the cavity are constrained to match exactly with *every* tooth of the comb - a feat the demands both exceptionally achromatic optics and extremely precise *absolute* positioning of the cavity mirrors. The constraint on Q is also lightened - with a white light source, the number of photons in each cavity mode scales as Q^{-1}, while the number of passes, and hence the absorbtion signal, scales as Q. Assuming a shot noise limit, this means that the SNR scales as $Q^{1/2}$, compared with Q for the case of a coupled frequency comb.

Other light sources that are "intermediate" between thermal lamps and lasers,

such as superradiant lasers and UV LEDS, are also worth investigating[**?**]. Rapid progress in high power UV solid-state light sources has been made recently[88], including the development of COTS fiber-coupled LED based light sources with more than 40 mW output power. It should be noted that these fibers are very much multimode (1000μm diameter typ.), so the efficiency of coupling this source to a cavity will also be low. These sources typically have much narrower spectra (10 nm FWHM typical) than thermal sources that better overlaps with the spectral region of interest; ultimately, broadband detection system might contain several light source-cavity pairs, each probing a different region of the UV.

With an incoherent white light source, absolute knowledge of the frequency components - equivalent to accurate knowledge of the cavity geometry - would have to extracted somehow, either by monitoring a trace species with a known spectrum in the mixture, or by adding a component of well characterized light, such as a stabilized laser, to the white light source.

6.1.4 Extension to larger molecules

The size of the largest molecules that could be uniquely resolved via this technique is at present unclear. Certainly there is interest in being able to accurately resolve mixtures of larger molecules, especially in biological applications. Two examples are pheromones and hormones[6], which are both important biological signals, and have typical molecular weights in the 200-800 amu range, about twice that of naphthalene (for example, Androstenol, a sex pheromone in pigs, is $C_{19}H_{30}O$, molecular weight

[6]pheromones are signals from one individual to another; hormones are signals within an individual

274).

The direct flow loading technique presented in chapter 5 applies to molecules that satisfy two criteria. First, in order to cool efficiently molecules must be larger than helium; we need $\sigma_{X-He} > \sigma_{He-He}$, which seems likely to be satisfied for almost any molecules as large or larger than naphthalene (see, for example, figure 4.9. Second, it is greatly preferable if the species remains free of adsorbed helium atoms. The criteria for this is believed to be $E_{vib} \gtrsim E_{X-He}$ (equation 5.4), which is in general violated for molecules of more than 40 atoms, although geometry plays an important role. Pheromones, with several carbon rings and additional attached groups, are certainly pushing this limit, and anything much larger or floppier would violate it.

It is possible that this limit could simply be ignored. The spectrometer described above could be useful even if every analyte was covered with a layer of adsorbed helium atoms. The random configurations of these atoms would broaden each transition by a few cm^{-1} [99], effectively precluding the resolution of rotational lines[7] ; this spectrometer would nevertheless resolve the UV spectrum from 200-400 nm into over 25000 channels, allowing for excellent discrimination between even rather large molecules. This type of broadening would be barely detectable (and invisible on the figure) in the narrow-featured cold naphthalene spectrum of figure 6.2. As a second alternative, the spectrometer could be run at higher temperatures; operating at 15-20 K would produce enormous narrowing of spectral features compared to a 300 K vapor, but even in equilibrium almost no helium would be adsorbed onto the molecules.

[7] "..effectively precluding the resolution of rotational lines..": this would not be true of adbsorbed helium atoms were attached in only a few ways; that is, the possibility exists that various isomers of X·He could be individually rotationally resolved.

6.2 Chemistry at 6 K

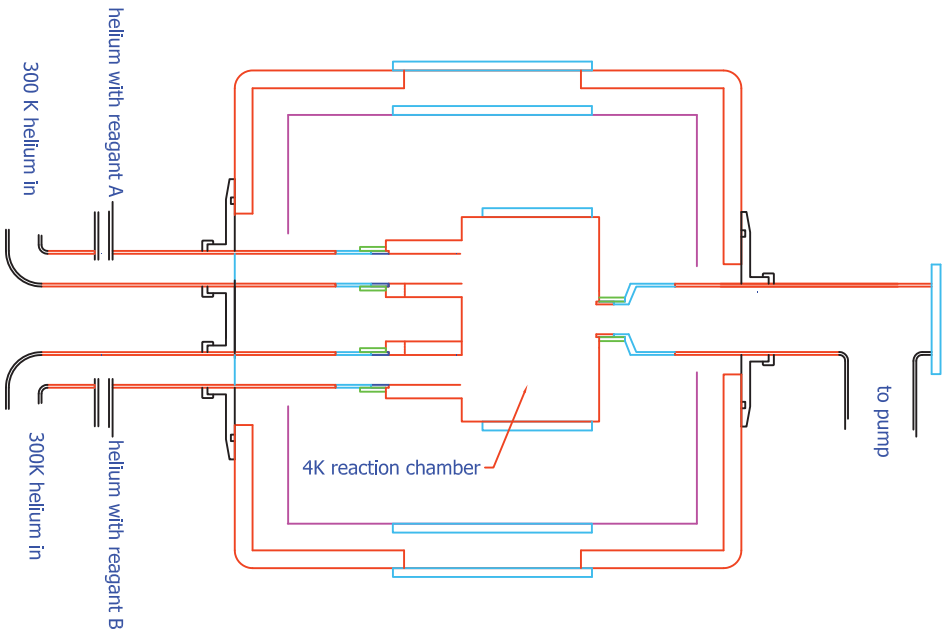

Figure 6.7: A straightforward modification of the apparatus presented in chapter 5 would allow low temperature mixing to study reactions in binary mixtures. This apparatus could be built in the current dewar and would operate under conditions very similar to those presented in chapter 5. The ability to sensitively detect even small quantities of reaction product, combined with the long diffusion limited interaction times in the large (10 cm) reaction chamber, would allow the detection of cold gas phase reactions several orders of magnitude slower than with the current apparatus or in CRESU experiments. Note that the reagents only mix *after* they are cold.

There has been much recent interest in cold gas-phase chemical reactions, including interest in chemistry in the interstellar medium[90], spin-mediated chemical reactions[108], and field mediated reactions.

The CRESU (Cinetique de Reaction en Ecoulement Supersonique Uniforme) technique, developed by Smith and Rowe in the 1990s [90], has been used to observe a number of reactions in conditions rather similar to those found in direct flow loaded buffer gas cells. These conditions are found in the fast flowing isentropic kernel of a

Laval nozzle supersonic jet, with T = 1-25 K, and $n_{he} = 10^{16} - 10^{17}$. The main limitation of this technique is that the flow remains uniform for only 100-500 microseconds, requiring that any observed reaction occur rather rapidly. This disadvantage carries a silver lining: the density of reagents can in fact be quite high - up to 1% of the total flow - because even at these high densities the molecules do not have time to aggregate. The CRESU technique can measure reaction rate constants down to 10^{-12} cm^3 molecule^{-1} s^{-1}, comparable to those measured in chapter 5 with naphthalene dimerization.

Cold chemical reactions have also been observed using other techniques. The group of Willitsch et. al. [6] has recently observed chemical reactions between cold trapped ions and translationally cold but rotationally warm neutral polar molecules, and numerous studies with crossed molecular beams, at comparatively high (200 K) but accurately determined (± 1%) energy have shed great light on the physical processes leading to gas-phase chemical reactions, including state-specific cross sections[67][?].

The high sample densities and generality of the cooling technique demonstrated in chapter 5 allow for a large variety of cold chemistry experiments, ranging from exploration of three body recombination as outlined in section 5.4 to possible electric field mediated reactions of aligned polar molecules.

Current reaction rate detection limits in our experiment are $\sim 10^{-12}$ cm^3 molecule^{-1} s^{-1}, but straightforward improvements in our apparatus could result in significant improvements in this sensitivity. Figure 6.7 shows a hypothetical apparatus in which the second half of the flow tube has been replaced by a larger "reaction chamber".

The diffusion limited lifetime in a buffer gas cell scales as r^2:

$$\tau_{diff} = \frac{n}{\dot{n}} = \frac{n_{He}\sigma_{A-He}r^2}{\bar{v}}$$

Adding a chamber 10 cm on a side but leaving conditions otherwise unchanged would result in a diffusion limited lifetime of ≈ 3 seconds. In addition, as shown in figure 6.7, it would be straightforward add multiple input channels, so independently controlled amounts of various reagents could be mixed at low temperatures. It of course remains true that any reaction between reagents A and B would have to 'compete' with the natural aggregation of A+A $\Rightarrow$ A·A, but even a small amount of a reaction product, e.g. A·B or the product of a "harpooning reaction" could be detected amid other, less interesting aggregates.

Improvements to our fluorescence detection therefore translate directly into improved sensitivity to slow chemical reactions. Straightforward improvements in optics should allow for a dramatic increase in sensitivity. This is especially true when searching for reaction products that are absent in the incoming beams; such experiments operate at a large advantage, because the background density of these products can be extremely low.

Field mediated reactions

Field mediated "reactions", in the form of feschbach resonances, have become a workhorse in the formation of ultracold molecules from precooled samples of ultracold atoms[81]. These techniques work in the single-channel regime, where the atoms are interacting via S-wave collisions only, and the reaction is mediated by precise control of

the last bound state between the atoms in this channel. The cold molecules presented here are very far from this regime, not only scattering via many partial waves but in fact occupying many rotational states. Typical field interaction energies of a few cm^{-1} are dwarfed by the thermal energy k_bT at room temperature, so at best very slight levels of direct field mediated control of reaction rates can seen in a warm thermal bath. This is no longer true below 10 K.

If samples of highly polar molecules such as benzonitrile or ICN can be prepared at temperatures of $\sim$ 2K, they can be strongly oriented even in modest fields of 20 kV/cm despite being 'classically' spread over many rotational levels.[38] This orientation would have a dramatic effect on the molecules' long range dipole-dipole interaction, and suggests that field mediated chemistry in a classical regime could be possible. Similar or even stronger field interactions can be induced with magnetic fields; most the magnetic molecular species will rapidly thermalize with the buffer gas, resulting in a large (order unity) polarization for high fields.

Fullerenes and exotic molecules

Figure 5.6 and table 5.1 indicate that direct flow cooling should work with the macromolecules C_{60} and C_{70}; despite their large size, these molecules are extraordinarily stiff, allowing them to satisfy the criteria of equation 5.4. These molecules have been cooled in supersonic jets, both as monomers and in clusters [48].

Even more exotic is the prospect of cooling C_{60} molecules with metals trapped inside of them. Such molecules of course exhibit large numbers of degrees of freedom, violating equation 5.4, but they are also known to be remarkably stable, suggesting

that the trapped species within is effectively shielded from the environment by the fullerene cage.

6.3 Non-linear optics and magnetometers

There is substantial interest in extending a wide range of room temperature vapor cell optical experiments to cryogenic temperatures; for an excellent overview see reference [15]. Theoretical estimates of spin relaxation rates in alkali-helium collisions suggest that decoherence rates will be substantially lower at cryogenic temperatures, and Hatakeyama et.al. have measured spin relaxation times of minutes in samples of rubidium loaded into ^{4}He buffer gas cells at 2 K.[47]. Room temperature vapor cells are current competitors for the world's most sensitive magnetometers [16], and have been applied in this capacity in fields as diverse as medical imaging and geophysics. The limiting factors in the sensitivity of these magnetometers are complex, but they are in general limited by either Rb-Rb or Rb-He inelastic collisions; these processes are dramatically reduced at low temperatures.

A major challenge in these experiments is the production of long-lived, high density samples of cold alkali vapor. In a spinoff experiment from the work presented in this thesis, high optical densities (≈ 50) of atomic rubidium, and correspondingly narrow EIT features[55] were observed. Figure 6.8 shows this optical density and EIT signal.

In this work, we observed a very significant and to date unexplained loss mechanism in ablated samples of atomic rubidium; similar unexplained results have also been observed by others[96][47]. Direct flow loading begins with a clean vapor, in

contrast with ablation, which produces a complex and poorly understood plasma containing atoms, clusters, and ions; it therefore seems highly probable that this loss would be dramatically reduced with direct flow loading. This hypothesis is supported by the fact that Hatakeyama et. al. observed very long lifetimes for rubidium samples introduced into cold helium via the very clean, non-thermal process of laser induced atomic desorbtion (LIAD)[47]. This suggests that it is unknown contaminants, rather than atomic rubidium vapor, that causes the "dust" problem. Further discussion of the "dust" effect appears in section 4.1.1. Both rubidium and potassium have been loaded into cryogenic cells via direct flow loading, but measurements of rubidium lifetimes have not been made.

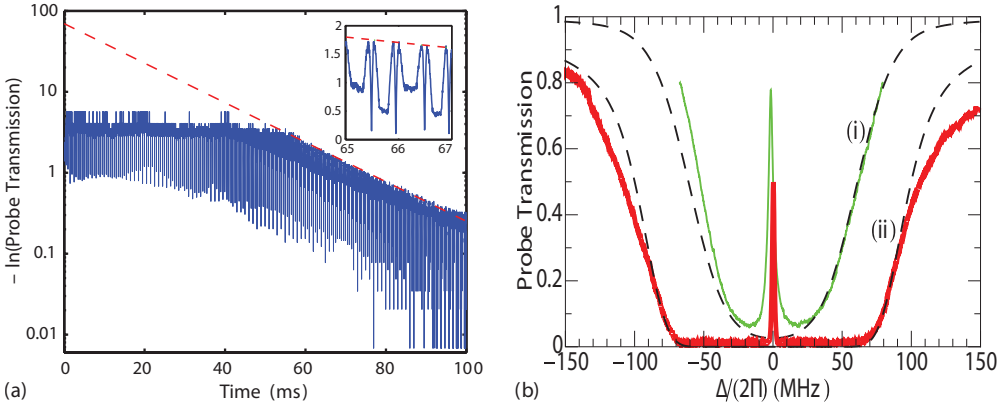

Figure 6.8: High optical density and EIT observed in 7 K rubidium. a). Optical density D; the fine structure (see inset) is the individual sweeps over the EIT dips. b) Probe transmission at two different optical depths D, showing the sharp EIT dip on the background of a doppler-broadened single-photon absorbtion line. The dashed lines are 7K theory. Reprinted from reference [55]

6.4 Into a trap

The techniques outlined so far in this thesis can provide high fluxes of slow, cold, and state selected molecules. Many of the experiments listed in table 1.1 become possible only when the sample is trapped; this allows not only much longer interaction times, but opens up a whole host of additional cooling and manipulation tools. It is therefore worthwhile to consider the problem of this "final" step: loading the molecules into a trap.

6.4.1 Prelude: traps for neutral molecules

The absolute ground state $|0\rangle$ of any atom or molecule is always low field seeking, for both electric and magnetic fields. This is because the applied field couples states of the unperturbed molecule, causing these states to repel. The absolute ground state is by definition below any other state, so "repelling" in this case means the energy of $|0\rangle$ drops with increasing field - thus it is a high field seeking state.

The ideal trap would therefore have a field maximum in free space. Maxwell's equations unfortunately preclude this from happening with static fields[33]. This limitation can be evaded in two ways. Deep, low field seeking traps, both magnetic and electric, can be made that trap metastable polarized samples that are antialigned with the field; and shallow, absolute ground state traps can be constructed using AC fields in a variety of ways. Nonconservative optical "traps"(e.g. magneto-optical traps and optical molasses) are also routinely made for cold atoms; although proposals exist to extend these to a select class of molecules[94], such traps are not considered in this work.

Absolute ground state traps have the important advantage that at low enough energy, two body collisions between trapped molecules *must* be elastic[8]; there is by definition no other degree of freedom to exothermically absorb the energy. These elastic collisions allow for the possibility of further evaporative cooling.

300 K blackbody radiation limits the lifetime of trapped polar molecules to a few seconds[51]. It is convenient side effect for cryogenic trap loading experiments that this loss mechanism scales as T, and is substantially reduced in a cryogenic environment.

Table 6.1 lists several demonstrated and proposed traps, along with their limitations. Both trap volume V and trap depth D are important figures of merit when considering a trap design. Ideally, the phase space acceptance of the trap should overlap well with the phase space occupied by the beam. In most realistic situations, the beam will occupy both more physical space (10s of cm^3) and have a higher temperature (several K) than the trap[9]. Under these conditions, the molecule loading rate is proportional to $VD^{3/2}$; the final trap phase space density is in general *independent* of both V and D, but is proportional to the beam phase space density.[10]

[8]this excludes the possibility of exothermic chemical reactions, such as harpooning reactions - a possibly important exception when dealing with molecular radicals and reactive atoms such as alkali atoms

[9]this criteria is perhaps not met for large, deep superconducting magnetic traps; see section 6.5.2

[10]In cases where trap loss in limited by two body collisions, a deeper trap can actually lead to *lower* phase space density in the trap, as additional "hot" molecules knock out the cold molecules

Trap type	trappable species	depth D [K]	volume V [cm^3]	absolute ground state?	comment	
super-conducting magnet	paramagnetic atoms and molecules	up to 5 K (4 K/μB)	$\sim$50	No	requires 4K cryo-genics	[46]
permanent magnet, ferromag-net	paramagnetic atoms and molecules	up to 1 K (4 K/μB)	10^{-10} - 100	No	inexpensive, often in-flexible	[106]
electrostatic	polarizable molecules	$\lesssim$ 0.8 K for 1 Debye molecules (10 mK/ kV D)	on-chip - $\sim$.1	No	switchable	[11]
alternating gradient	polarizable molecules	up to 5 mK	2×10^{-2}	Yes	mixtures problem-atic?	[104]
Optical off-resonant	any species, including nobel gasses	$<$ 1 mK	10^{-5}	Yes		[97]
microwave	polarizable molecules	1-1000 mK	λ^3 = 0.5-10	Yes	not yet demon-strated	[30]

Table 6.1: Various demonstrated and proposed traps for neutral molecules

6.4.2 Phase space manipulation

In the final section of this chapter, a "recipe", using ingredients from chapters 2,3,4, and 5, for continuously loading a high flux beam of molecules into a trap is presented. Before the beam can be allowed to enter a trap region, it must be separated from the buffer gas that threatens to ruin the cryogenically pumped trap volume. This

can be done with a beam guide, as demonstrated in chapter 3, or with a simple field gradient "mirror" that diverts the species of interest.

Magnetic mirrors

A simple but effective mirror can be created simply by arranging an array of permanent magnets with alternating orientation; A simulation and realization of such a mirror is shown in figure 6.9, and a similar mirror is included in the complete proposal of figure refpumpload1. This mirror has a calculated 'reflection depth' of 350 mK for a 1 μB species; assuming the incoming beam is collimated by 10:1 $v_{forward}$:$v_{transverse}$, this implies that the mirror reflects atoms or molecules with a forward energy of $mv_z^2/2 < 35$ K; for potassium, this is 100 m s^{-1}; in fact atoms or molecules moving faster than this are likely untrappable in any case.

The fluxes from the combination source/mirror shown in figure 6.9 were substantially lower than expected. At the time (2009) this was unexplained, and the experiment was temporarily laid aside, but later work with very similar neon-cooled rubidium beams in the same apparatus strongly suggests that the problem was poor vacuum (due to imperfectly pumped neon). This problem could be easily remedied, for example with the modified two-stage nozzle described in figure 2.23.

High field seeking "mirrors"

The magnetic mirror shown in figure 6.9 is designed to reflect only low magnetic field seeking molecules. A similar electrostatic mirror could reflect low electric field seeking polar molecules, but larger polar molecules effectively have only high field seeking states. There is therefore a need for a device which can separate a beam

of high field seeking molecules from a carrier gas. This has been done, for example in the case of iodobenzene[54], and in general is only slightly more difficult than deflecting low field seekers. Figure 6.10 shows a simulation of a simple electrostatic beam deflector for the case of ND_3, separating the beam into low field seekers, non-field seekers, and high field seekers. Note that the high field seekers (blue traces) are significantly more dispersed than the low field seekers (red traces). This is a common feature of working with high field seeking molecules; the positive second derivative of the electric field means that the more a beam gets deflected, the more it will continue to get deflected - the beam disperses. Careful electrode geometry can minimize this effect[7].

Halbach mirrors

It came to our attention after we had produced the mirror shown in figure 6.9 and the guides of chapter 3 that an alternative geometry known as a Halbach array produces a "one sided flux structure" that can increase - and in the ideal case double - the mirror depth [69]. This technology can similarly significantly increase the available depth of permanent magnetic traps. Halbach arrays are commercially available and widely used in fields as divergent as refrigerator magnets, free electron laser wigglers, and levitating trains, but to my knowledge are unknown in the AMO community. Figure 6.11 shows a typical configuration.

6.5 Trap loading mechanisms

In order to load molecules into a conservative potential, energy must somehow be dissipated within the trap volume - otherwise molecules simply enter one side of the potential and leave the other.

6.5.1 Trapdoor loading

Figure 6.12 shows the simplest trap loading scenario - molecules are allowed to enter a trap region, and then the trap is "turned on" behind it, leaving the molecules trapped. This mechanism is extremely general - it can be used with any trap that can be switched rapidly compared to molecule transit times. The main drawback is that it is reversible, and as such is constrained by Louisville's theorem - phase space density is conserved. Even in high flux beams, particle densities are rather low, and so trap door loading tends to lead to modest trap densities. Stark deceleration into a trap[9] can be thought of as efficient phase space manipulation followed by trap door loading.

It is worth noting that a large *number* of molecules can be "trapped" without dissipation in a conservative potential if the entrance is small compared to the size of the trap. A molecule that enters the trap will eventually find its way out again, but perhaps only after many orbits of the trap. This strategy was successfully employed by Rempe et. al. in reference [85], and can be combined with trapdoor loading if the narrow entrance channel is eventually - potentially quite slowly - closed. Again, phase space density in the trap is constrained to be equal or lower to the phase space density in the beam.

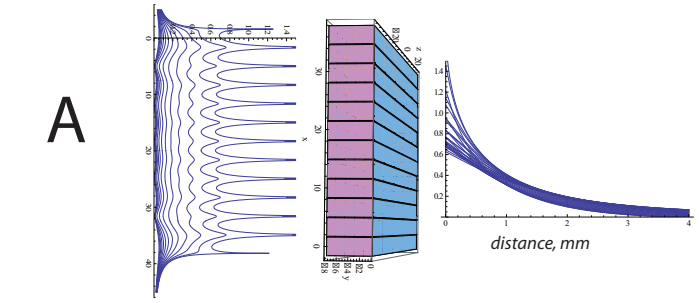

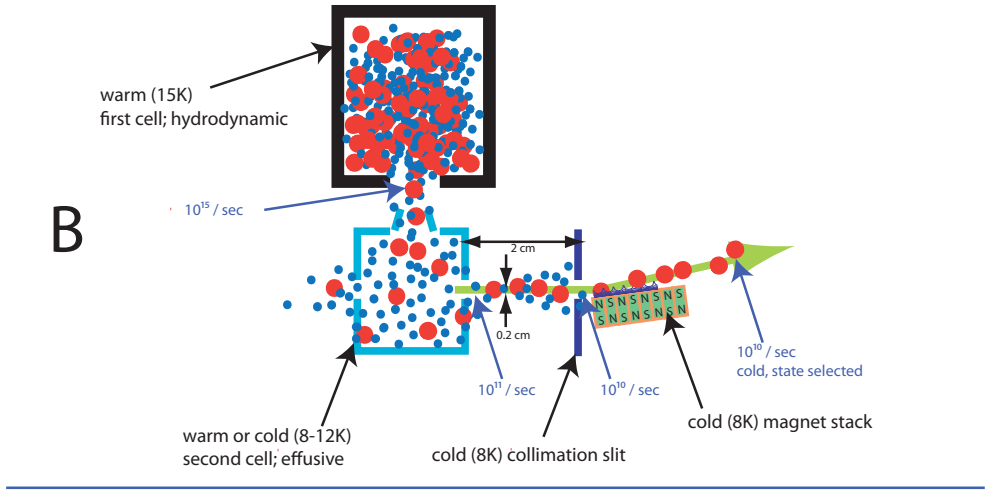

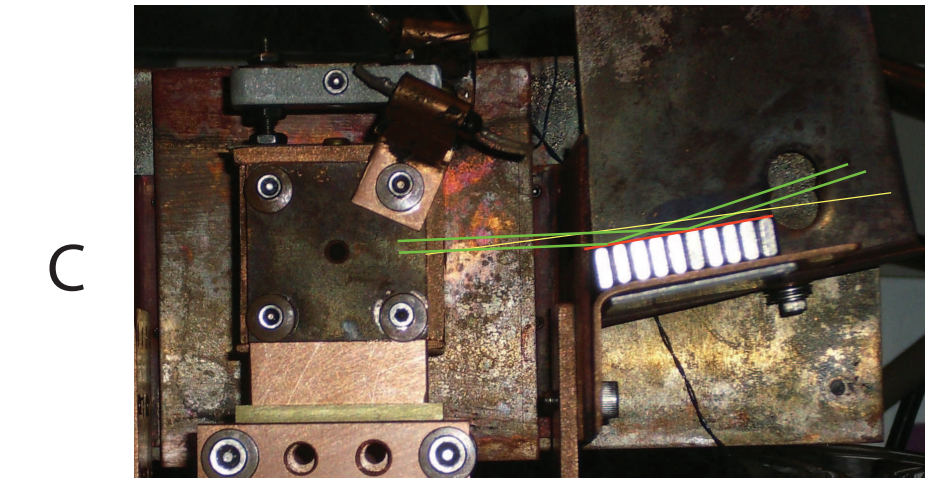

Figure 6.9: A realization of a simple magnetic mirror, composed of alternating NdFeB magnets. A). Simulation of the magnetic field. The mirror has a depth $D \approx 7000$ gauss, implying a depth for a one bohr magneton species of ≈ 350 mK. B) Layout of an experiment incorporating this mirror. The source in this experiment is a modified form of the two stage nozzle presented in section 2.4.6, where the beam bends through 90 degrees in the second stage. Measured (via LIF and absorbtion spectroscopy) fluxes of potassium at various stages are shown. C) implementation. The mirror is simply an array of bar magnets held together by their own magnetic attraction; they are held in place via magentic forces from a steel plate, visible below them in the figure.

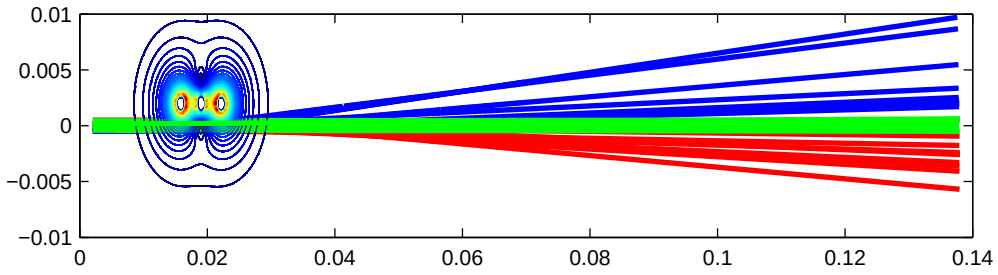

Figure 6.10: A simulation of a simple electrostatic beam separator, simulated for 10 K ND_3 boosted to 50 m s^{-1}. The separation between the high field seeking (blue), non-field seeking (green), and low field seeking (red) tracks is evident. Buffer gas copropagating with the beam would follow the green tracks. Dimensions (x and y axis) are in meters.

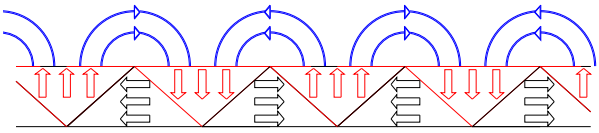

Figure 6.11: A Halbach array, which produces a magnetic flux (shown in blue) on only one side.

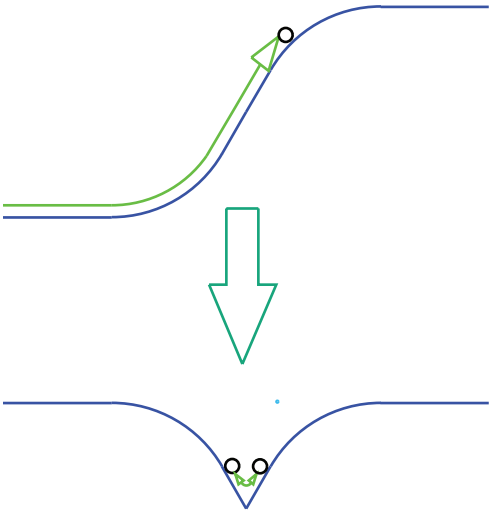

Figure 6.12: A simplified version of trapdoor loading. In (A), molecules from the beam run uphill into what will eventually be the trap region. In (B), the other side of the trap is turned on, leaving the sample trapped

6.5.2 Optical pumping loading

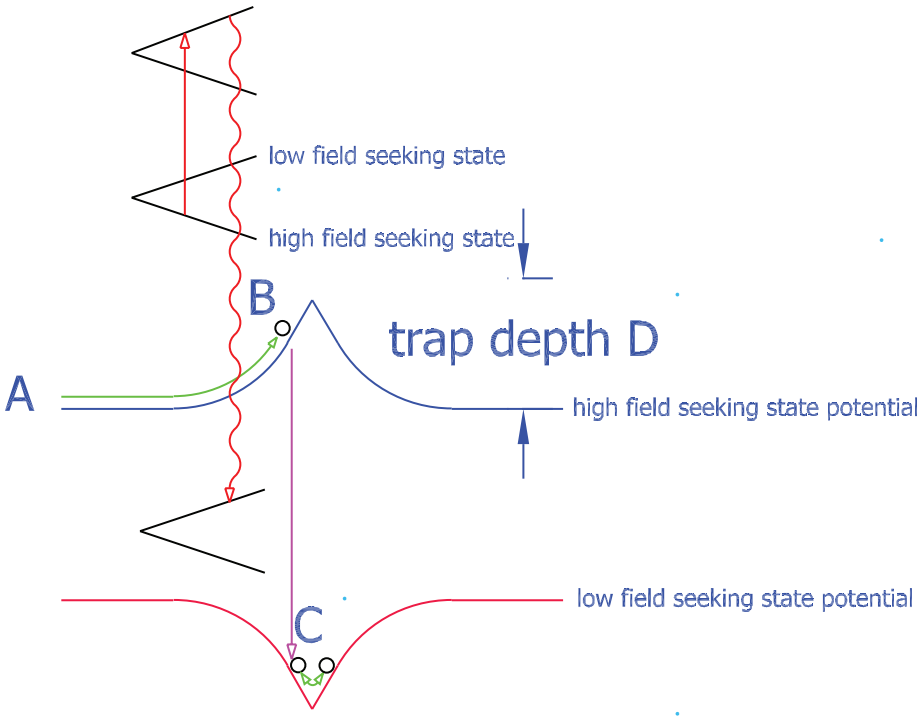

Figure 6.13: A "one photon" continuous trap loading mechanism, for a hypothetical two state system and a low field seeking trap. The blue curve represents the "trap" potential as seen by a cold incoming molecule in a high field seeking state (A). At (B), the molecule has lost about half of its energy and is pumped into the low field seeking, trapped state (red curve). The molecule is now trapped, and dark to the laser. Exact efficiencies depend on geometry, but the scheme loads most molecules of energy initial energy E_0 such that $D/4 \lesssim E_0 \lesssim 3D/4$, where D is the trap depth.

Figures 6.13 and 6.14 show an irreversible trap loading scheme based on optical pumping that will continuously load a trap from a beam of slow molecules. Molecules in untrapped states are allowed to "run uphill" into the trap volume, and are then optically pumped into a trapped state. This scheme can work for loading both electric and magnetic traps.

Direct irreversable loading of molecules from a cold beam has not been demon-

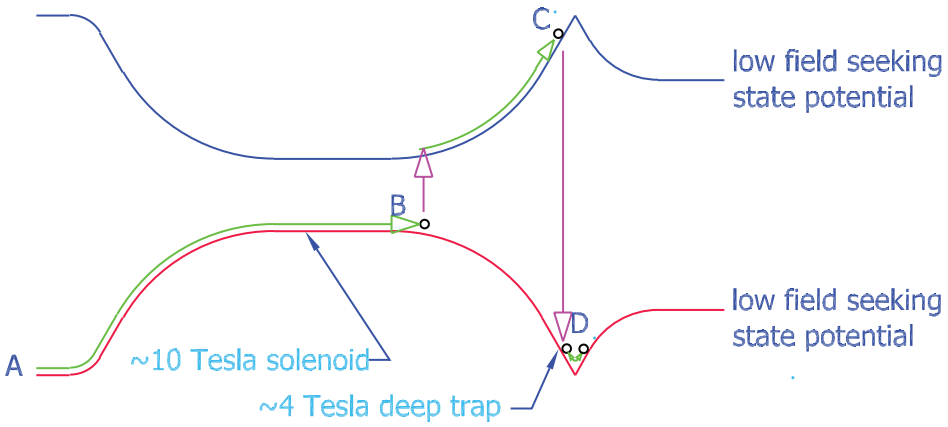

Figure 6.14: An extension of the scheme shown in figure 6.13. The potential now represents a low field seeking magnetic trap, with a moderately large (10 Tesla) solenoid on one side. The cold molecular beam now enters in a low field seeking state (A), and climbs a steep hill into the solenoid (B), where it is pumped into a high field seeking state. It continues to climb into the "trap" (C), and is finally pumped into a trapped state. For $B_{max} = 10$ Tesla, this scheme removes about 12 K of energy per bohr magneton. A direct analogy using electric traps for polar molecules is possible. A simulation of this scheme is shown in figure 6.16.

strated to date, although Pfau et. al.[95] have demonstrated a similar mechanism with cold atomic chromium, and Meijer et. al. have made great progress towards demonstrating a very similar scheme with stark-decelerated NH[103][52]. Related techniques have been proposed in several forms for more exotic traps.[30][82].

The fact that this mechanism is *irreversible* is of critical importance. The "ratchet" of the spontaneous emission allows us to escape from Louisville's theorem, and can in principle lead to far higher densities and phase space densities in the trap than exist in the beam. The final density limit depends on the dominant trap loss mechanism, and could even be set by molecule-molecule collisions within the trap.

Figure 6.14 shows the same scheme with an added "hill" included to further decelerate the beam before it enters the trap region. Appropriate placement of the optical

pumping laser can reap a double deceleration from this hill - uphill on the way in, and uphill again on the way out. This is related to sisyphus cooling, and could be thought of a one-stage static magnetic decelerator[72]. This loading mechanism is in fact quite straightforward, and is perhaps a "solution waiting for a problem"; that is, it relies on a continuous, slow, cold source such as those presented in this thesis, which to date have not been available.

Figure 6.16 shows a simulation of the entire system, assuming a starting beam of NH with the same parameters as the demonstrated beam of potassium shown in figure 2.21. Assuming 10:1 collimation in both x and y, perfect optical pumping, and perfect input state selection, about 10% of this beam ends up trapped. Including a more realistic 50% loss per optical pumping stage, and a 80% hit for incorrect initial state distribution, this implies a 1 $\times 10^{-4}$ net efficiency from buffer gas cell to trap. If NH beam production is comparable to potassium, this represents a clean loading rate of 2 $\times 10^{12}$ molecules s^{-1}. There is no helium anywhere in the dewar in this proposal, effectively eliminating the helium film problem that has plagued many buffer gas trapping and cooling experiments[45].

The same mechanism could be used with potassium[11], to load immense numbers of alkali atoms into a the trap. Ideally, enough alkali gas could be loaded to use this trapped (and potentially laser cooled) gas as a buffer gas itself to load other species into the same or a coexisting trap. The details of these proposals, however, are "two steps into the future," and are beyond the scope of this thesis.

[11] or perhaps sodium or lithium, which would have a lower forward energy at the same velocity

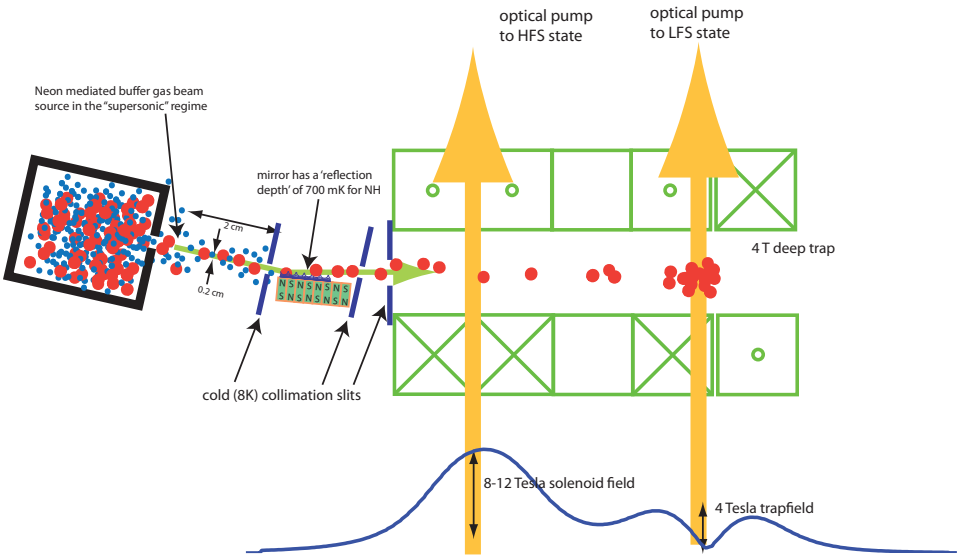

Figure 6.15: An overview of the entire proposal. A neon mediated high flux source of NH is filtered by a low field seeking magnetic mirror, as discussed in section 6.9. The beam is then directed into the bore of a combination solenoid/anti-helmholtz trap, and is loaded into the trap via the scheme presented in figure 6.14.

6.5.3 Scaling for weak traps

Straightforward variations of this scheme can adapt it for high field seeking AC traps as well, but scaling laws cut heavily into the expected flux. ND_3 would be the ideal candidate except the optical pumping transition is at 158 nm, solidly into the vacuum ultraviolet. Rigid rotor molecules such as CaF or CaBr have accessible transitions, but are difficult to decelerate due to their low rotational constants. This constrains these the scheme to work with "almost effusive" sources, such as the ytterbium beam demonstrated in figure 2.17. This, combined with the low expected trap depth (< 50 mK), dramatically cuts the loading rates in these scenarios. Using $\dot{N} \propto S^{-3/2}$, and a realistic factor of 100 drop in beam flux from moving to an effusive source, the net estimated loading rate for CaF into a 15 GHz, 5 cm^3, 30 mK deep,

2 MW circulating power microwave trap is $\sim 2 \times 10^6$ s^{-1}, or $\sim 10^6$ times lower than figure 6.16.

It is also possible that a weak, absolute ground state trap can be most efficiently loaded via a deep, low field seeking traps; there is evidence that the phase space manipulation that can be done with a trapped sample is much more likely to be ideal than that done in a beam, where increasingly divergent beams tend to "trumpet" at low velocities. A trapped environment also allows for the phase space to be manipulated slowly with rather gentle tools, such as weak, AC fields or collisions even at rather low (< 1 Hz) rates.

6.6 The future

In summary, the optimal path from a ~ 10 K beam to a ~ 10 mK trap remains unknown, but necessarily involves at least one irreversible step, such as spontaneous emission. It seems very probable that a combination of both strong, metastable traps and weaker fields for manipulating absolute ground state particles will be required. The techniques developed in this thesis have increased the available flux of cold molecules by many orders of magnitude from previous sources; we are therefore hopeful that extensions of these techniques will soon lead to a general method for trapping high densities of neutral molecules.

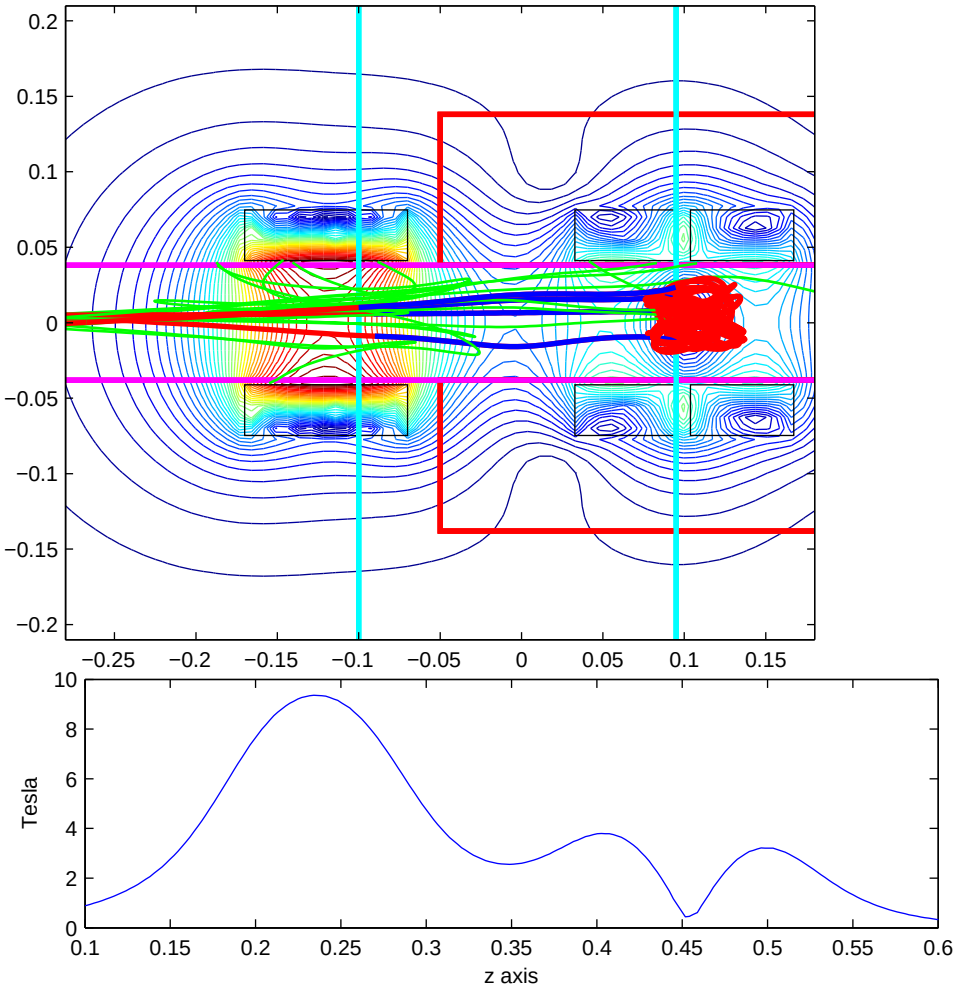

Figure 6.16: A simulation of the scheme of figures 6.14 and 6.15. The upper trace shows the simulated field for the existing Mark VII magnet used in [22] and described in [46], attached to a simple solenoid. The red rectangle on the right hand side of the plot shows the location of the Mark VII titanium cask. The entire geometry is cylindrically symmetric about the central axis. The heavy red and blue curves represent trajectories that result in trapped molecules; the lighter green tracks are trajectories that result in untrapped molecules. The beam assumed here has $v_{forward}$ = 160 m s^{-1} with a spread of 40 m s^{-1} - extremely similar to the beam of cold potassium shown in figure 2.21. The beam is assumed to be collimated to 10:1 in both transverse directions. About 10% of this beam ends up trapped.

Appendix A

Theoretical Spectrum of Naphthalene

Naphthalene is an asymmetric top; that is, it has three distinct rotational constants around the x, y and z axes of the molecule. This is the most general case of a rigid rotor, and is not exactly soluble. The constants for the ground state are, [68]

$$A = 3105.1 \text{ MHz}$$

$$B = 1231.4 \text{ MHz}$$

$$C = 883.9 \text{ MHz}$$

The hamiltonian for this system is

$$H = AJ_x^2 + BJ_y^2 + CJ_z^2 \tag{A.1}$$

Since no two of $[J_x^2, J_y^2, J_z^2]$ commute, it is unsurprising that this system has no

physically transparent good quantum numbers beyond j. It is traditional [50] to identify the states by four quantum numbers: j,m_j,k_+, and k_-. j is the total angular momentum and m_j is the projection of j on the z axis. k_+ is the projection of the angular momentum along the top axis *if the molecule was adiabatically changed into a prolate ($B = C$) symmetric top*, and k_- is the projection of the angular momentum along the top axis *if the molecule was adiabatically changed into an oblate ($A = B$) symmetric top*. Identifying the states in this way is extremely useful, as it allows selection rules and Honl-London factors that hold exactly for symmetric tops to be used. Both k_- and k_+ range from $[0..j]$, and $k_+ + k_- = j$ or $j + 1$

For an exact symmetric prolate top, the energy the states $|jk_+\rangle$ is doubly degenerate for $k_+ \neq 0$; since $k_+ + k_- = j$ or $j + 1$, these two degenerate states can be associated with $k_- = j - k$ and $k_- = j - k + 1$.

Figure A.1 shows the exact solution for the $j = 3$ manifold of an asymmetric top. Figure A.2 shows the exact solution for the $j = 10$ manifold of naphthalene for a variety of asymmetry parameters b_r. b_r is defined as

$$b_r = \frac{(C - B)}{2[A - \frac{1}{2}(B + C)]}$$

and has a value of 0.085 for naphthalene. Numerous approximations exist for expressing the levels of asymmetric tops in Taylor series about $b_r = 0$, but with the easy availability of numerical diagonalization, the exact solution is readily calculated. Figure A.2 shows that our initial approximation of $b_r = 0$ is invalid.

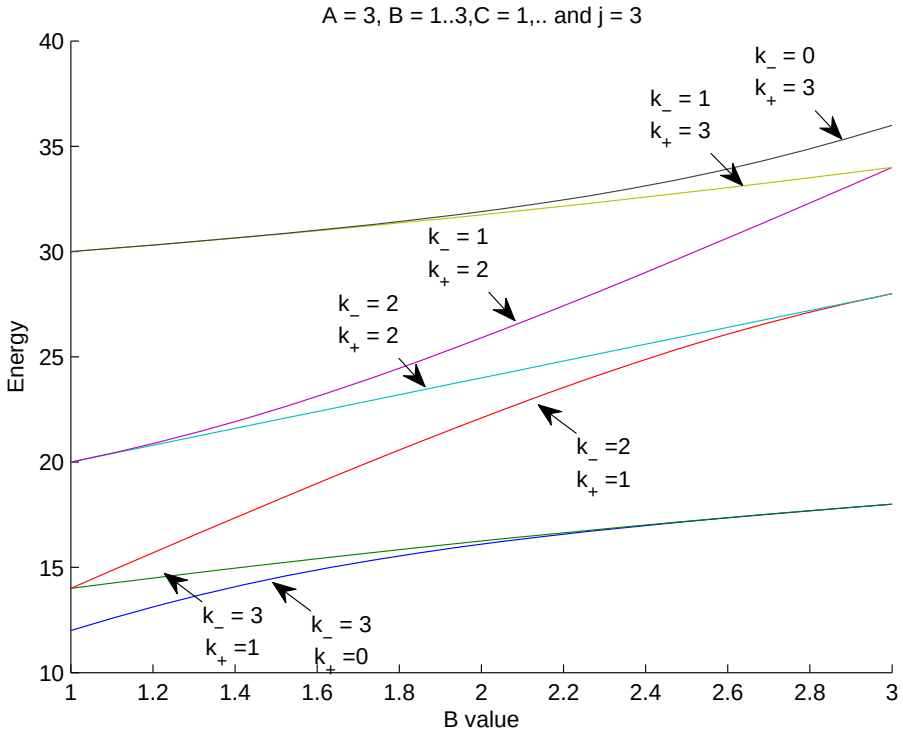

Figure A.1: the exact solution to the $j = 3$ manifold of an asymmetric top with rotational constants $A = 1$, $B = 1..3$, and $C = 3$. The left hand side, with $B = C$, corresponds to an exact prolate symmetric top with $k = k_+$; the right hand side corresponds to an exact oblate top, with $k = k_-$. k_+ and k_- for an intermediate state are in fact defined as the endpoints of the state's line on this figure.

A.1 Numerical methods

The spectrum is calculated as follows: The energies for all rotational levels up to J = 150 (the lowest level in the J = 150 manifold has an energy of $\approx$ 1000 K.) are calculated. All possible spectral lines are then calculated, according to the following

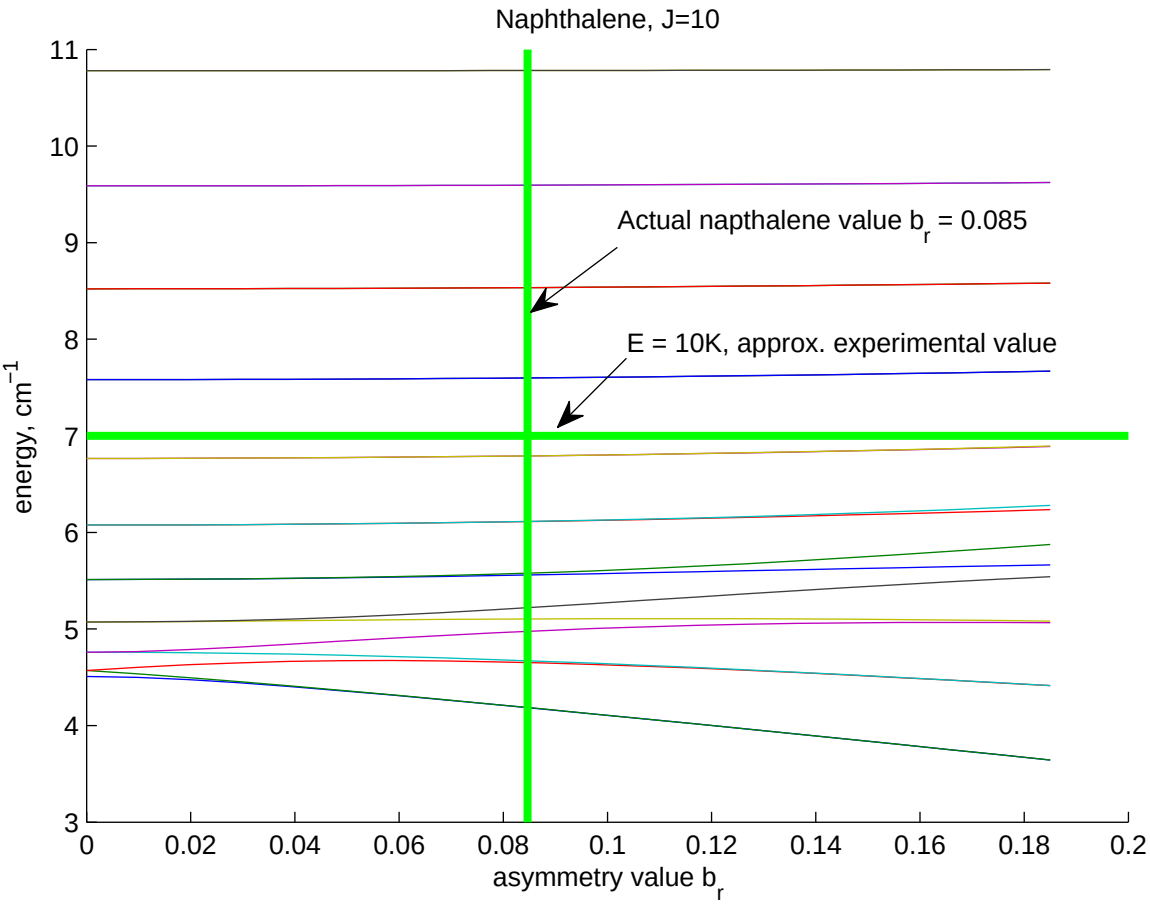

Figure A.2: the exact solution to the $j = 10$ manifold of naphthalene. The left hand side of the plot corresponds to the best approximation prolate symmetric top. The vertical green line represents the actual naphthalene asymmetry parameter, and the horizantal green line, at $T = 10K$, represents a reasonable 'thermal cutoff'; that is, levels below this line will all be substantially populated.

selection rules for a perpendicular b-type transition:[68][100]

$$\Delta j = 0, \pm 1$$

$$\Delta k_+ = \pm 1$$

$$\Delta k_- = \pm 1$$

Each line is then assigned a line strength, based upon the lower state thermal population $e^{-E/k_b T}$, the lower state degeneracy $g = 2j+1$, and a Honl-London factor, that describes the overlap of the spherical portion of the respective wavefunctions. Following [68], the Honl-London factors are taken to be identical to the symmetric top case. These states are described by J and K of the lower state, and are: [**?**]

$$A_{KJ} = \begin{cases} \frac{(J+2\pm K)(J+1\pm K)}{(J+1)(2J+1)} & \text{for } \Delta J = +1\,, \\ \frac{(J+1\pm K)(J\mp K)}{J(J+1)} & \text{for } \Delta J = 0,\,, \\ \frac{(J-1\mp K)(J\mp K)}{J(2J+1)} & \text{for } \Delta J = -1 \end{cases} \tag{A.2}$$

The resulting manifold of lines is then summed. Figure A.3 shows calculated spectra for 300,77, and 4K respectively, convolved with the effective power broadened spectrum expected for excitation from our pulsed laser (2 microjoule, 5 nsec, 308 nm). This broadening is far too much to resolve individual rotational lines; a simulated spectrum limited by doppler broadening is shown in figure A.3. Figure A.4 shows the same three spectra with an unrealistic 50 MHz linewidth; the huge number of rotational lines is evident.

The largest matrix that is diagonalized in this example is $(2J_{max}+1)\times(2J_{max}+1)$, or about 300×300; this is done in Matlab and takes less than 1 second per matrix.

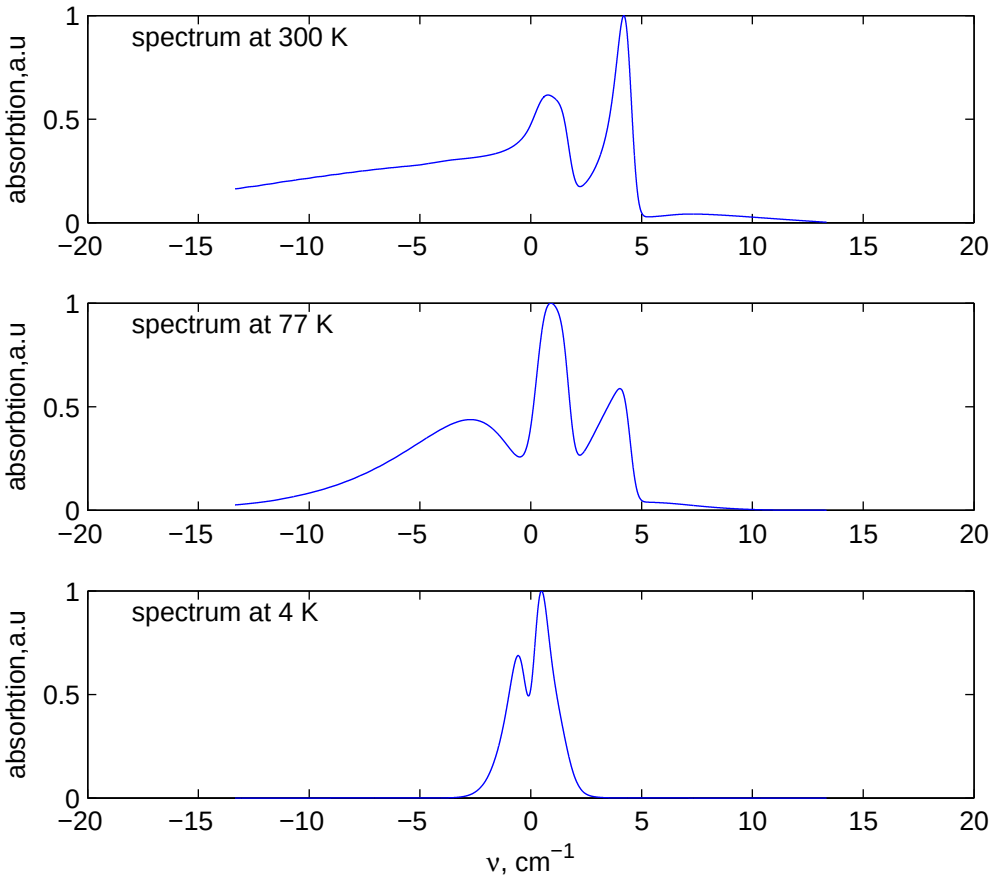

Figure A.3: Simulated spectra for naphthalene at 300, 77 and 4 K. For this simulation, the linewidth of the transition was assumed to be the power broadened linewidth of $\approx$ 10 GHz.

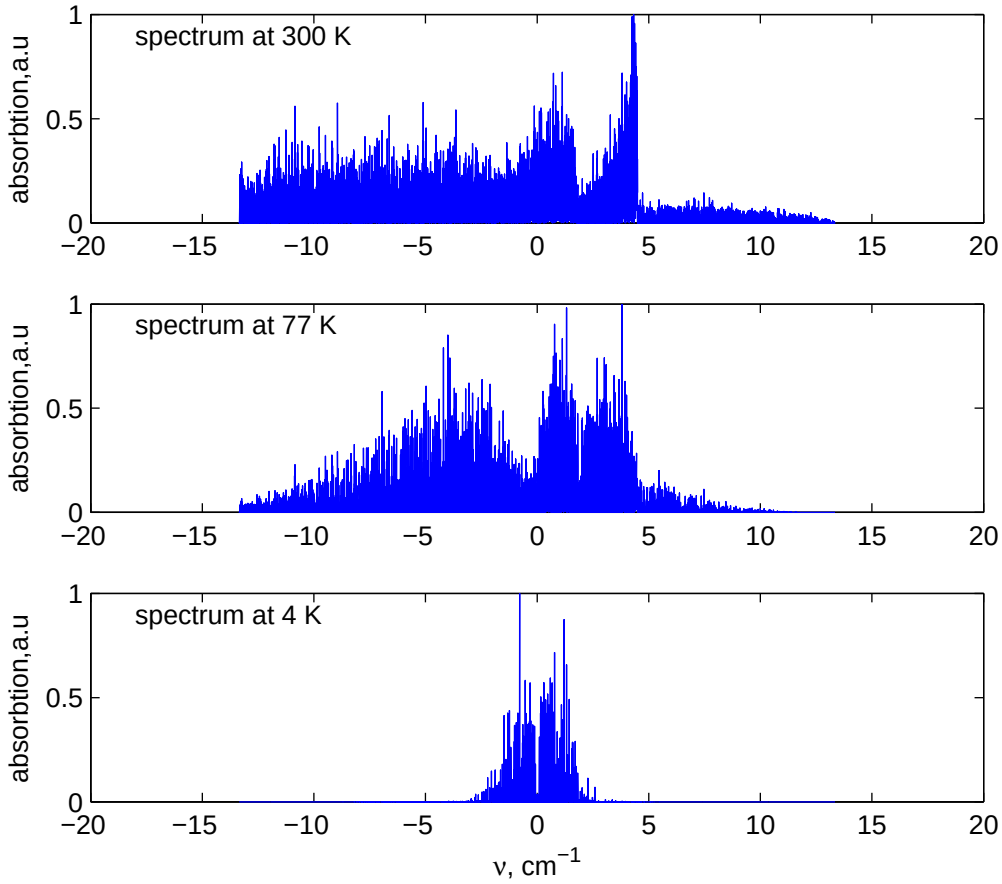

Figure A.4: Simulated spectra for naphthalene at 300, 77 and 4 K. For this simulation, the linewidth of the transition was assumed to be 50 MHz, roughly corresponding to a 4K doppler width. These spectra are arbitrarily cut off at $\pm$ 13 cm^{-1}; this truncates only the 300 K spectrum. The forest of rotational lines that make up the observed spectrum is evident

Appendix B

In Gas Cooling: Buffer Gas Cooling 2.0?

In this appendix, a proposal to cool the buffer gas itself is presented, via sympathetic cooling with an aggressively laser cooled "coolant" species[1]. This proposal is included as an appendix, rather than an application in chapter 6, because significant technological hurdles must be overcome before it becomes possible.

Figure B.1 diagrams a hypothetical experiment in which normal buffer gas cooling is turned on its head. Rather than allowing the sample to be cooled by the buffer gas, a degree of freedom that readily thermalizes with the buffer gas is aggressively cooled via optical pumping with external lasers. Inelastic collisions with helium atoms then re-excite this degree of freedom and absorb energy from the helium gas; it is then pumped back to the lower state, and the cycle continues. If realizable, this would

[1]although lasers are used, it would be more accurate to describe this cooling as "anti-stokes" cooling

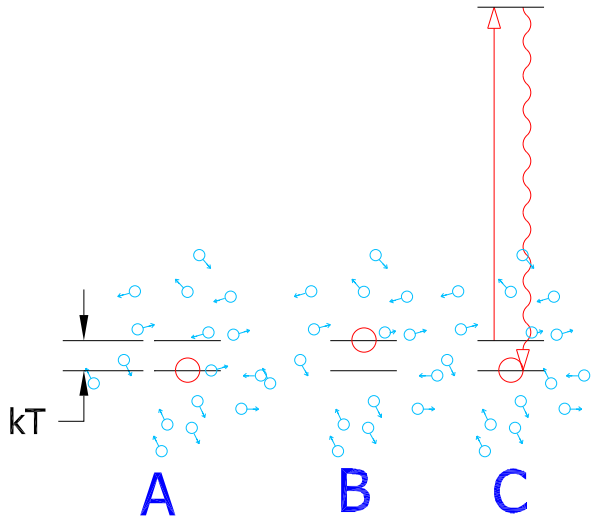

Figure B.1: A proposed scheme to cool an entire buffer gas cell. (A)A high density of species X with a state $\Delta E \approx k_b T$ above the ground state is imbedded in a cold helium gas. (B) collisions with the cold gas excite X to the excited state, extracting energy from the gas. (C) X is optically pumped back to the ground state, and the cycle continues. As outlined in the text, a number of issues prevent this scheme from being realized.

be an enormously valuable tool, as it would allow the sympathetic cooling of almost any other species that was also mixed into the cell. This proposal is related to the demonstrated laser cooling of solids[44], which is moderately successful; materials have been cooled 65 K from room temperature. It is only tangentially related to conventional "laser cooling" in the doppler cooling sense of the term.

For simplicity, this degree of freedom is approximated here as a simple two state system with energy gap ΔE; an example of such a system would be the spin of a 1 μ_b atom which has a large helium collision spin-relaxation cross section. This example system has the advantage that the gap ΔE is tunable via an external magnetic field;

the optimal value is depends on thermalization and repump rates, but will be of order $\Delta E \approx k_b T$, which is assumed in the calculation below.

In order to compare these processes, let us consider a specific example, with a 1 cm cell filled with 10^{16} helium atoms and 10^{14} "coolant" atoms. We further assume $\Gamma = \sigma_{elastic}/\sigma_{inelastic} = 10$; that is, it takes 10 collisions to inelastically reorient the molecule, and a starting (wall) temperature of 4 K. In this example, the mean free time τ is given by

$$\tau = \frac{1}{n_{he}\bar{v}_{He}\sigma} \approx 1\mu\text{sec}$$

The time for a coolant atom to rethermalize, to the upper state, removing $\Delta E \approx k_b T$ from the helium gas, is $\Gamma\tau = \tau_2 = 10$ μsec. We assume it is repumped into the ground state immediately [see below].

The time to reduce the *entire* gas sample - every helium atom, not just the ones which hit coolant atoms - by $k_b T$ per atom is $\tau\Gamma\frac{n_{helium}}{n_{atom}}$, or 1 msec. 1 msec after we turn the laser on, every atom in the gas has lost $O(k_b T)$ of energy - the gas is now at $\approx$ 1.5 K. This represents fast (10^{-3} s) but low power (10 μWatt) cooling.

heating mechanisms

The calculated 10 μWatt cooling will have to compete with conductive heating as the buffer gas thermalizes with the (now warmer) cell walls. As in section 2.4, we wish to compute timescales for these processes; can we cool faster than we heat?

The heating and cooling times are

$$t_{cool} = t\Gamma \frac{n_{he}}{n_{atom}} = \frac{\Gamma}{n_{atom}\bar{v}\sigma} \approx 10^{-3}s.$$

and

$$t_{heat} = t n_{he}^2 r^2 \sigma^2 = n_{he} r^2 \sigma \bar{v}^{-1} \approx 10^{-2}s.$$

so the figure of merit, cooling power over heating power, is:

$$M = \frac{P_{cool}}{P_{heat}} = \frac{T n_{he} n_{atom} r^2 \sigma^2}{\Delta T \Gamma} \approx 10 \tag{B.1}$$

Where T is the temperature of the cell wall, and ΔT is the temperature difference between the cell center and the cell wall.

In order for even this highly idealized thought experiment to work, we need $M > 1$.[2] For the parameters listed above, this seems possible, but deviations from this ideal behavior (see below) are problematic.

Excited state collisions and closed transitions

Reality is likely to be significantly worse than the ideal case presented above. In particular, the coolant atoms are spending a good fraction of the time in an electronically the excited state. This state corresponds to 1000s of K, and any channel, such as inelastic $A^* - A^*$ collisions, which carries this energy into the translational motion of the gas will be a disaster. Such excited state collisions are in fact one of the

[2]The form of equation B.1 can be easily interpreted: M scales as σ^2 because a higher cross section means the coolant atoms thermalize faster, so the cooling works faster. And at the same time, there is more 'insulation' from the walls; so heating goes slower. And why does M seem to get *better* with more helium? We are assuming that the cooling rate is limited by relaxation time; adding helium adds cooling power, since it shortens this relaxation time. But the thermal conductivity to the walls of the cell is independent of helium density, so adding helium is a net gain. If the cooling is limited by something else (laser power, pumping speed, or the natural lifetime), then adding helium won't help.

limiting factors in (much lower) MOT densities. In addition, optical pumping could be a problem; each atom is cycling 1000s of times, and could easily become shelved in a dark state.

Optical density

It is important that the sample NOT be optically dense. This is because the re-emitted photons are explicitly bad, and repump ground state atoms into the 'hot' state. These photons need to leave the sample rather than being reabsorbed. The optical depth of the sample described above is enormous - assuming a strong transition and a typical 4K doppler broadening of 100 MHz, the optical depth will be $D = 10^4$! Great progress can be made by applying a strong magnetic field gradient to the sample; for example, a 1 Tesla field variation corresponds to about 20 GHz of broadening, reducing the optical density to "only" 50, which is still far too high. A transition 100 times weaker than a standard electric dipole transition could make up the rest of the deficit, but we need a transition which decays fast compared to the 10^5 rethermalization rate. Although an atom with a lifetime of 1 μsec apparently satisfies both of these criteria, this remains a significant problem.

Laser power

The above example requires that the atoms are repumped into the ground state at a rate of 10^5 Hz; this is very fast! The fundamental limiting rate is the excited state lifetime, which is typically about 100 times faster than this, or $\approx 10^{-7}$ seconds for a strong optical transition; however, practically realizable pumping rates are typically $\lesssim \Gamma/10$, so there is not much overhead here.

The cooling laser is a significant piece of machinery in this example. With $N_{coolant} = 10^{14}$, and each atom absorbing ≈ 2 photons every 10 μsec, the laser must provide ≈ 10 watts (assuming $\lambda = 500$ nm).

All of this light is rescattered, and will almost certainly heat up the cryostat; this issue can be resolved by running the experiment in a "pulsed" mode. A cycle of "on" for .010 seconds and "off" for .99 seconds would lead to a very manageable 10 mWatt heat load on the cell, but almost complete cooling during the "on" times, since the timescale for cooling is .001 seconds.

The laser also needs to be artificially broadened over about 20 GHz, to match the magnetic broadening applied above. I not aware of any off the shelf components that can provide such a light source.

Bottom line

Unlike the suggested technologies chapter 6, this suggestion faces significant technical and perhaps fundamental barriers before it can be realized. Among other limitations is the fact that the "coolant" densities assumed in this section are 1-2 orders of magnitude beyond those demonstrated in this thesis. It is nevertheless included as a conjecture because the payoff - a potential path to sympathetically cool *any* gas phase molecule to mK temperatures or below - would open the door to entire many new experiments in cold and ultracold physics.

Appendix C

Technical Drawings and Photos

The work of chapters 2,3, and 4 was done in a rectangular aluminum dewar manufactured by precision cryogenics. With the exception of the guided O_2 work of chapter 3, no liquid cryogens were used in this apparatus. The base temperature of the apparatus varies with heat load, but was generally between 4.4 and 6 K. Figure C.1 shows an overview of this dewar.

The work of chapter 5, as well as the EIT experiment of reference [55], was done in a modified Infrared Laboratories HDL-5 dewar. The outer vacuum can supplied by IR labs was replaced by an in-house version made from a 8" square aluminum tube, .500 wall thickness. As in the larger dewar, each side held a large, square port to allow general, adaptable access.

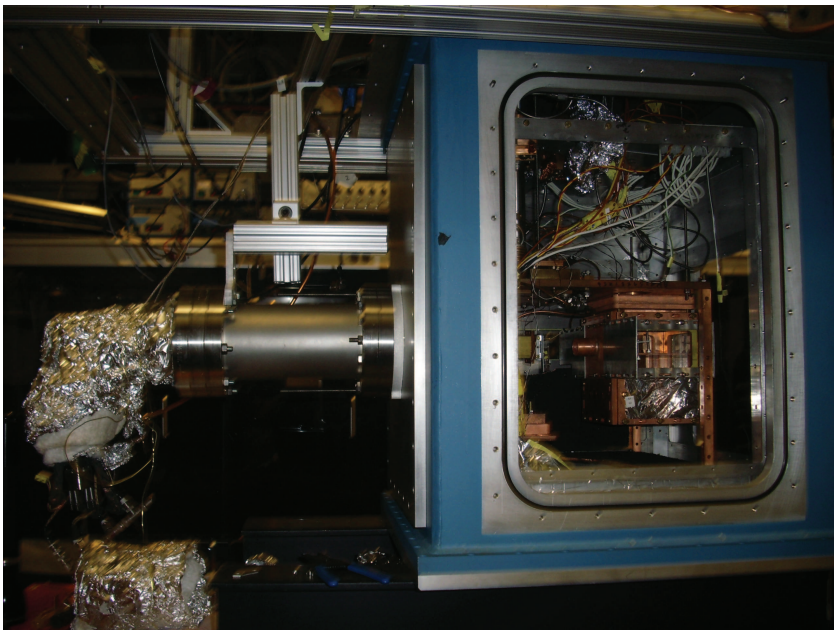

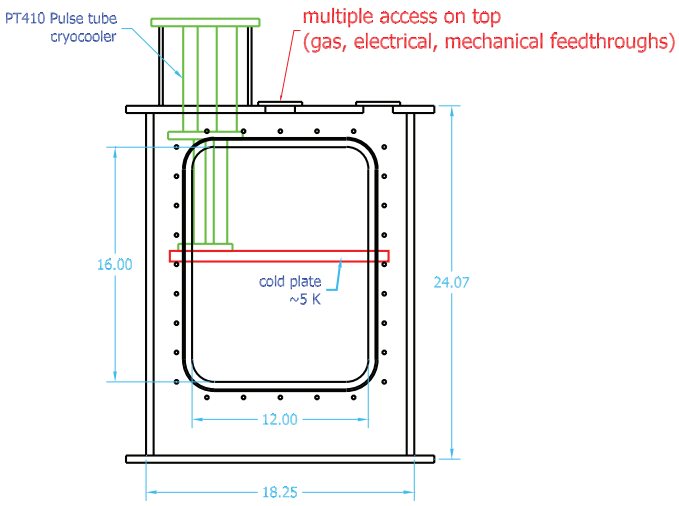

Figure C.1: The dewar used for the work of chapters 2,3, and 4. Each flat side of the dewar held a large rectangular port; these side plates could be removed and modified to provide increased optical access, feedthrus for flow, mechanical, or direct UHV access. Additional access ports are located on the top of the system. Not shown is a .125 thick 6061 aluminum radiation shield anchored to the 35K first stage of the pulse tube cooler. Cooldown time is about 12 hours, dominated by the cooling of this radiation shield; shield base temperature is about 80 K at the bottom of the dewar. The photo of the dewar is configured for the high flux, supersonic potassium beam of figure 2.21. The oven, wrapped in aluminum foil, is visible on the left; the differentially pumped copper "cold box" shown in figure 2.20 is visible inside the dewar.

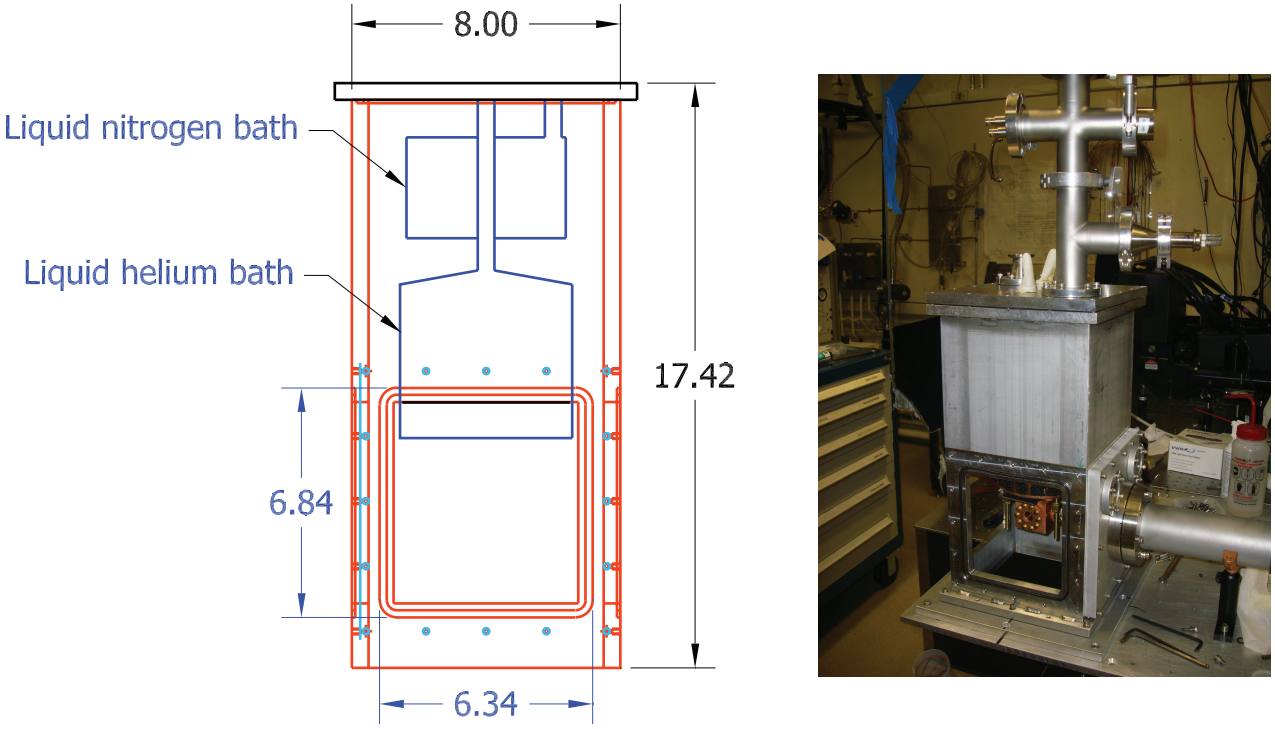

Figure C.2: The dewar used for the work of chapter 5 and reference [55]. The liquid nitrogen hold time for this dewar is about 5 hours (1 liter volume), and the liquid helium hold time with no external heat load is about 10 hours (1 liter volume), assuming the nitrogen is kept full. Not shown is a .125 thick oblong blackbody radiation shield anchored to the nitrogen bath. Cooldown time is about 3 hours, dominated by the cooling of this radiation shield; the shield base temperature is about 105 K at the bottom of the dewar. Cooling this dewar from 300 K to 4.2 K takes about 12 liters of liquid N_2 and 10 liters of helium.

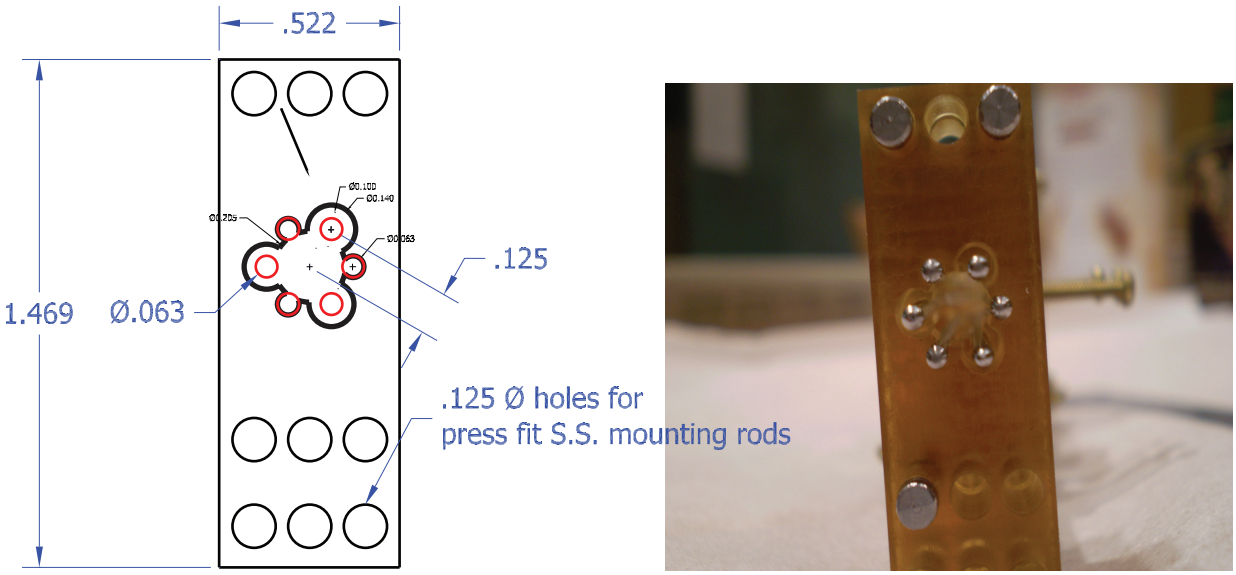

Figure C.3: One of the ultem alignment pieces used for the electrostatic guides of chapter 3. The red circles mark the locations of the 316 SS welding rods used as electrodes. These pieces are mounted in pairs, with each piece holding only the +6000 V or grounded rods; this was an effort to reduce surface currents that was, in retrospect, probably unnecessary.

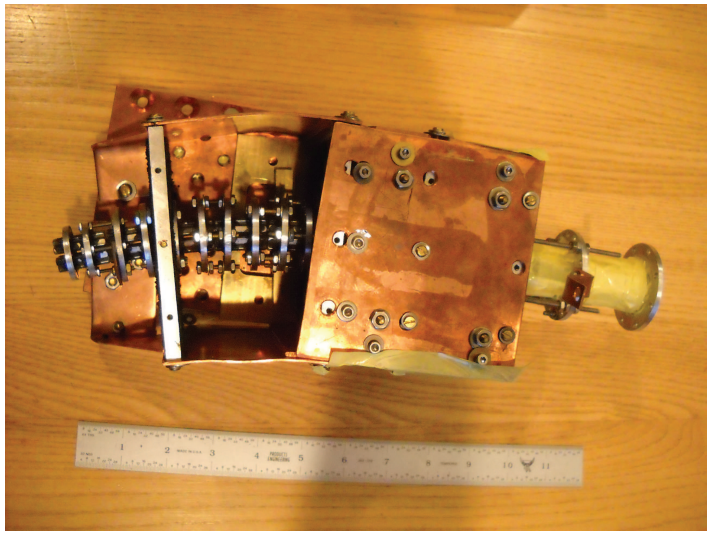

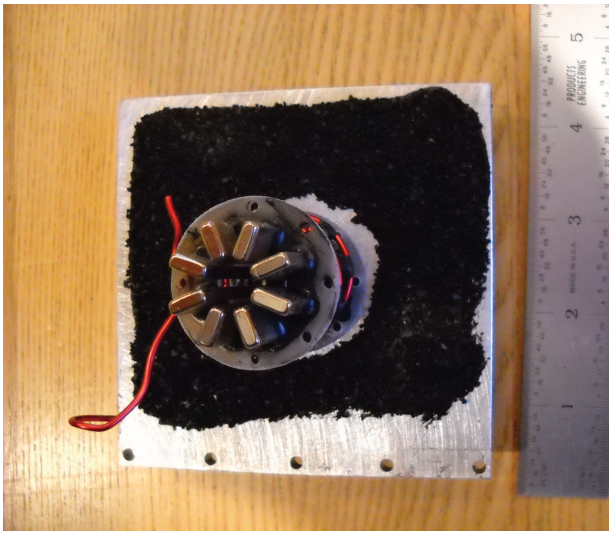

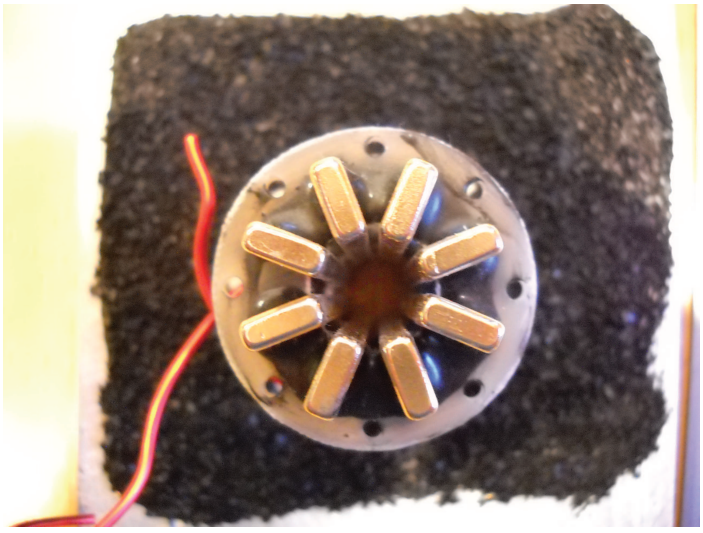

Figure C.4: The magnetic guide used in chapter 3. The charcoal sorbs and differential pumping volumes are visible. Each guide consists of 8 NdFeB magnets held with epoxy (Stycast 2850, Emerson-Cummings), into CNC machined G-10 collets. The net force on the magnets is inward; during assembly, a precision machined aluminum rod is inserted into the central hole.

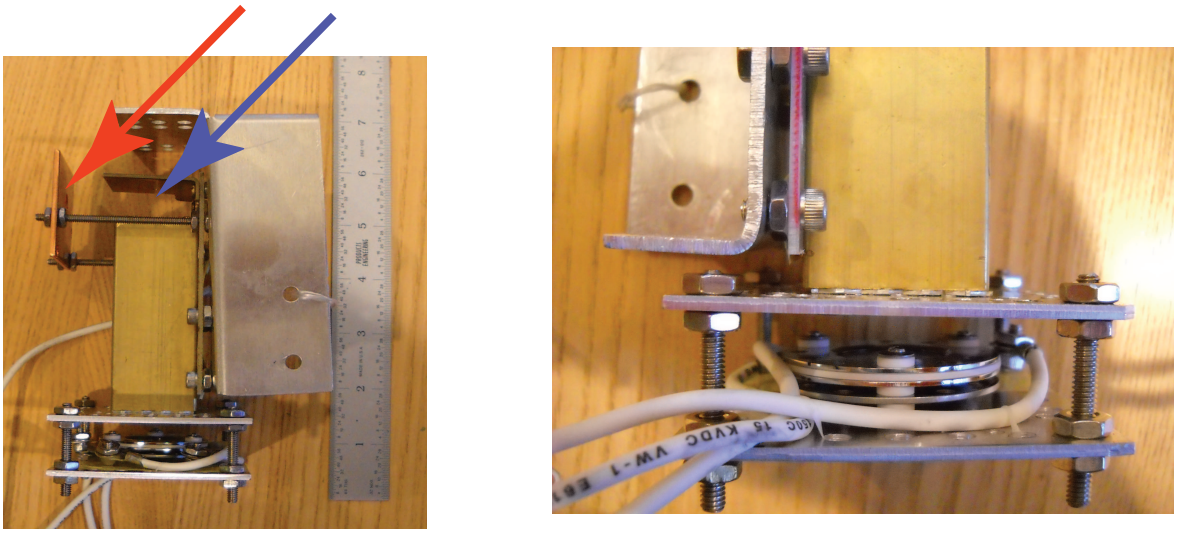

Figure C.5: The multichannel plate based TOF mass spectrometer used to detect ND_3 in chapter 3. The molecular beam enters from the viewer's point of view at the location marked by the blue arrow. The laser enters from the left, through the copper plate; ions are accelerated downwards into the brass drift tube. The copper plate (red arrow) is slightly negatively charged to repel electrons produced when the laser passes through the fused silica windows.

Figure C.6: The "1 K pot" used to reach a cell base temperature of 2.6 K for the guided oxygen work in chapter 3. This 1 liter pot was filled from a storage dewar and had a hold time of several hours. The lowest temperature measured on the cold plate of the pot was 1.3K; this was limited in part by the thermal loads, but also but also by the comparatively small (.5 inch) pumping line. The second .25 inch line is a safety blow off, in case of a leak or operator error resulting in an ice plug in the main pumping line. The first time this pot was tested, enormous taconis oscillations made it unusable; a combination of slowly throttling the valve to the pump (opening over about 30 seconds) and some copper mesh in the pumping line essentially eliminated this behavior.

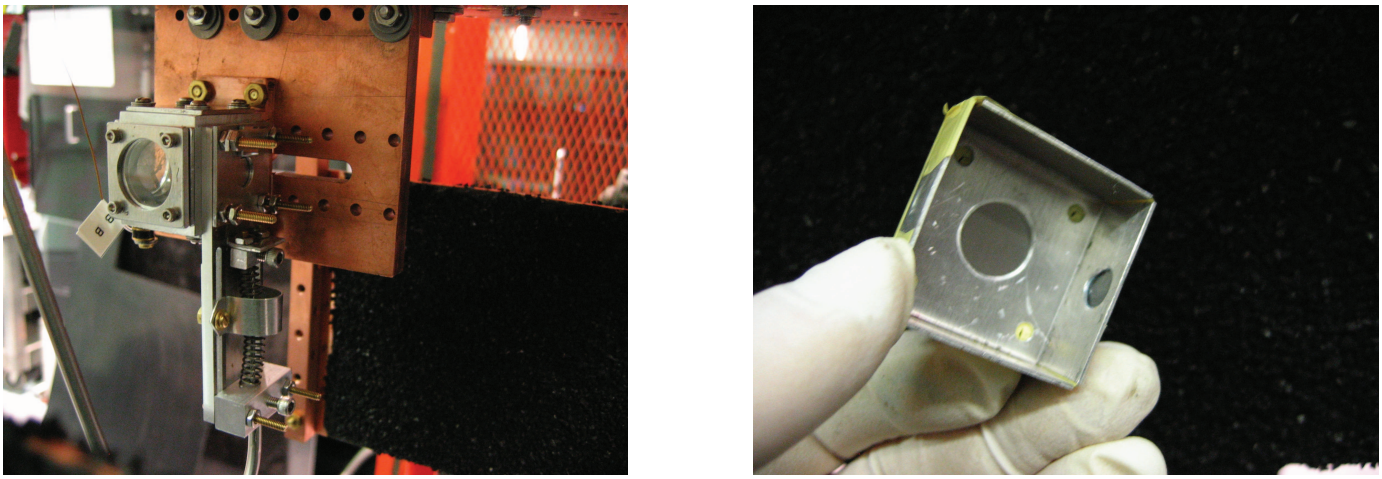

Figure C.7: Components of the two stage cell used to produce the ytterbium beam of figure 2.17. (A). The main cell, with the adjustable aperture (closed in this picture) clearly visible. The sample is mounted inside the aluminum cell, and is ablated through the 1" diameter quartz window. One of our high speed charcoal cryopumps is visible in the lower right. (B) The "second cell", removed in this picture. What appears to be an opaque circle is actually 25% transparent 316 S.S. mesh.

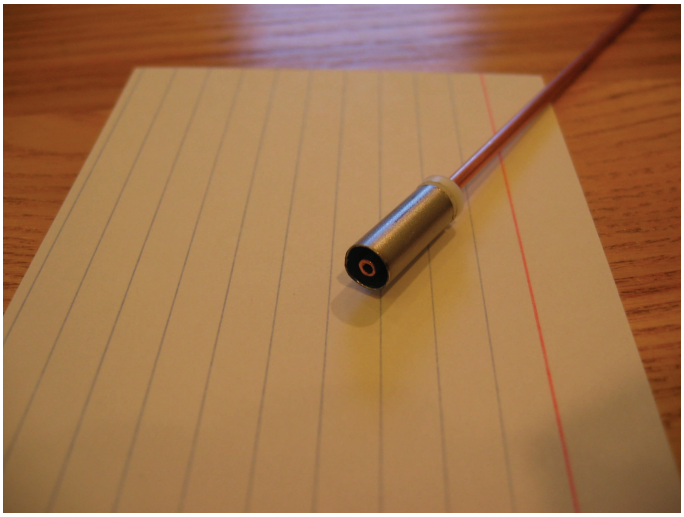

A

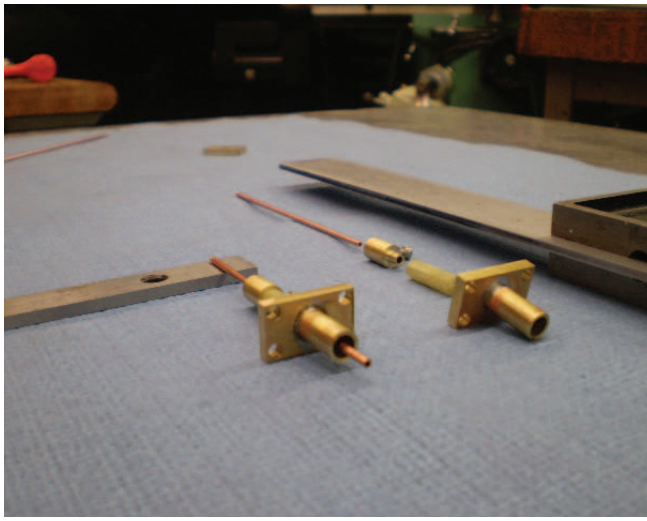

B

Figure C.8: capillary injectors used to inject O_2 at 90 K (A) and ND_3 at 300 K (B). The later design incorporated a cold brass shield tube in an effort to bring the injector tip further into the center of the cell. Pushing the tip of the capillary out into the main cell, as is shown in (B), results in greater heat loads on the cell but significantly less ice buildup between the capillary and the shield tube. The outer tube is thin walled stainless in (A) and G-10 in (B); G-10 is the superior material due to its far better thermal resistance.

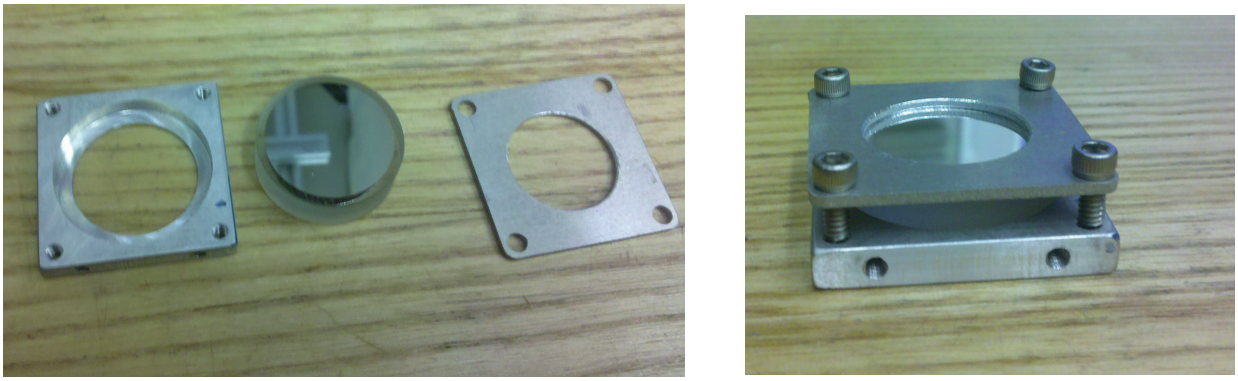

Figure C.9: A simple cryogenics-compatible optics mount. Differential thermal contraction often leads to large stresses being placed on brittle optics at low temperatures unless they are carefully mounted. In this simple design, the slight flexibility of the thin aluminum cover piece limits stresses. Both surfaces which touch the optic are covered in mylar tape to further reduce stress. This design was used dozens of times during the course of these experiments with no failures.

Bibliography

[1] Osama K. Abou-Zied, Hemant K. Sinha, and Ronald P. Steer. S2-s0 spectroscopy of the van der waals complexes of azulene with rare gases. *The Journal of Physical Chemistry*, 100(11):4375–4381, 1996.

[2] J. A. Barnes, T. E. Gough, and M. Stoer. Diffusive trapping: An alternative to supersonic jet cooling for spectroscopic experiments? *Review of Scientific Instruments*, 60(3):406–409, 1989.

[3] M. D. Barrett, J. A. Sauer, and M. S. Chapman. All-optical formation of an atomic bose-einstein condensate. *Phys. Rev. Lett.*, 87(1):010404, Jun 2001.

[4] Sigurd Bauerecker, Michael Taraschewski, Claus Weitkamp, and Heiko K. Cammenga. Liquid-helium temperature long-path infrared spectroscopy of molecular clusters and supercooled molecules. *Review of Scientific Instruments*, 72(10):3946–3955, 2001.

[5] Fred Behlen, Daniel McDonald, V. Sethuraman, and Stuart Rice. Fluorescence spectroscopy of cold and warm naphthalene molecules: Some new vibrational assignments. *Journal of Chemical Physics*, 5:5685–5693, 1981.

[6] Martin T. Bell, Alexander D. Gingell, James M. Oldham, Timothy P. Softley, and Stefan Willitsch. Ion-molecule chemistry at very low temperatures: cold chemical reactions between coulomb-crystallized ions and velocity-selected neutral molecules. *Faraday Discussions*, 142:73 – 91, 2009.

[7] Martin Berninger, Andre Stefanov, Sarayut Deachapunya, and Markus Arndt. Polarizability measurements of a molecule via a near-field matter-wave interferometer. *Physical Review A*, 76(1), JUL 2007.

[8] H. L. Bethlem, G. Berden, F. M. H. Crompvoets, R. T. Jongma, A. J. A. van Roij, and G. Meijer. Electrostatic trapping of ammonia molecules. *Nature*, 406:491–494, 2000.

[9] Hendrick L. Bethlem, Giel Berden, Floris M. H. Crompvoets, Rienk T. Jongma, André J. A. van Roij, and Gerard Meijer. Electrostatic trapping of ammonia molecules. *Nature*, 406:491, 2000.

[10] Hendrick L. Bethlem, Giel Berden, and Gerard Meijer. Decelerating neutral dipolar molecules. *Phys. Rev. Lett.*, 83(8):1558, 1999.

[11] Hendrick L. Bethlem et al. Deceleration and trapping of ammonia using time-varying electric fields. *Physical Review A*, 65(5):053413, May 2002.

[12] Hendrick L Bethlem, M R Tarbutt, Jochen Kupper, David Carty, Kirstin Wohlfart, E A Hinds, and Gerard Meijer. Alternating gradient focusing and deceleration of polar molecules. *Journal of Physics B: Atomic, Molecular and Optical Physics*, 39(16):R263–R291, 2006.

[13] J.L. Bohn. Inelastic collisions of ultracold polar molecules. *Phys. Rev. A*, 63:052714/1–5, 2001.

[14] L. W. Bruch, W. Schllkopf, and J. P. Toennies. The formation of dimers and trimers in free jet ^{4}he cryogenic expansions. *Journal of Chemical Physics*, 117(4):1544–1566, 2002.

[15] D. Budker, W. Gawlik, D. F. Kimball, S. M. Rochester, V. V. Yashchuk, and A. Weis. Resonant nonlinear magneto-optical effects in atoms. *Rev. Mod. Phys.*, 74(4):1153–1201, Nov 2002.

[16] D. Budker and M. Romalis. Optical magnetometry. *Nature Physics*, 3:227–234, 2007.

[17] Hans-Rudolf Buser, Helnrlch Arn, Patrick Guerin, and Stefan Rauscher. Determination of double bond position in mono-unsaturated acetates by mass spectrometry of dimethyl disulfide adducts. *Analytical Chemistry*, 55:818–822, 1983.

[18] L. Cai, J. Marango, and B. Friedrich. Time-dependent alignment and orientation of molecules in combined electrostatic and pulsed nonresonant laser fields,. *Physical Review Letters*, 86:775, 2001.

[19] Anna Rita Campanelli, Aldo Domenicano, Fabio Ramondo, and Istvn Hargittai. Molecular structure and benzene ring deformation of three cyanobenzenes from gas-phase electron diffraction and quantum chemical calculations. *Journal of Physical Chemistry A*, 112(43):10998–11008, 2008.

[20] W. Campbell. *Magnetic Trapping of Imidogen Molecules*. PhD thesis, Harvard University, 2008.

[21] W.C. Campbell, Timur Tscherbul, Hsin-I Lu, E. Tsikata, and J.M. Doyle. Mechanism of collisional spin relaxation in 3? molecules. *Physical Review Letters*, 102, 2009.

[22] W.C. Campbell, E. Tsikata, Hsin-I Lu, L.D. van Buuren, and J.M. Doyle. Magnetic trapping and zeeman relaxation of NH ($X^3\Sigma^-$). *Physical Review Letters*, 98:213001–1–4, 2007.

[23] Lincoln D Carr, David DeMille, Roman V Krems, and Jun Ye. Cold and ultracold molecules: science, technology and applications. *New Journal of Physics*, 11(5):055049 (87pp), 2009.

[24] S. Chapman and T. Cowling. *The Mathematical Theory of Non-uniform Gases*. Cambridge, 1964.

[25] Steven Chu, J. E. Bjorkholm, A. Ashkin, and A. Cable. Experimental observation of optically trapped atoms. *Phys. Rev. Lett.*, 57(3):314–317, Jul 1986.

[26] E. Clementi and G. Corongiu. Van der waals interaction energies of helium, neon, and argon with naphthalene. *J. Phys. Chem. A*, 105:10379–10383, 2001.

[27] Ch. Daussy, T. Marrel, A. Amy-Klein, C. T. Nguyen, Ch. J. Bord, and Ch. Chardonnet. Limit on the parity nonconserving energy difference between the enantiomers of a chiral molecule by laser spectroscopy. *Physical Review Letters*, 83(8):1554–1557, 1999.

[28] editor in chief David R. Lide. *CRC Handbook of Chemistry and Physics*. CRCPress, 2010.

[29] Sarayut Deachapunya, Paul J. Fagan, Andras G. Major, Elisabeth Reiger, Helmut Ritsch, Andre Stefanov, Hendrik Ulbricht, and Markus Arndt. Slow beams of massive molecules, Aug.

[30] D. DeMille, D.R. Glenn, and J. Petricka. Microwave traps for cold polar molecules. *The European Physical Journal D*, 31:375–384, November 2004.

[31] Scott A. Diddams, Leo Hollberg, and Vela Mbele. Molecular fingerprinting with the resolved modes of a femtosecond laser frequency comb. *Nature*, 445:627–630, 2007.

[32] S. Charles Doret, Colin B. Connolly, Wolfgang Ketterle, and John M. Doyle. Buffer-gas cooled bose-einstein condensate. *Phys. Rev. Lett.*, 103(10):103005, Sep 2009.

[33] S. Earnshaw. On the nature of the molecular forces which regulate the constitution of the luminferous ether. *Trans. Camb. Phil. Soc.*, pages 97–112, 1842.

[34] M. S. Elioff, J.J. Valentini, and D. W. Chandler. Subkelvin cooling NO molecules via billiard-like collisions with argon. *Science*, 302:1940–1943, 2003.

[35] U. Even, I Al-Hroub, and Joshua Jortner. Small he clusters with aromatic molecules. *Journal of Chemical Physics*, 115(5):2069–2074, 2001.

[36] Frank Filsinger, Jochen Kpper, Gerard Meijer, JonasL. Hansen, Jochen Maurer, Jens. H Nielsen, Lotte Holmegaard, and Henrik Stapelfeldt. Pure samples of individual conformers: The separation of stereoisomers of complex molecules using electric fields. *Angewandte Chemie International Edition*, 48:6900, 2009.

[37] Frank Filsinger, Jochen Küpper, Gerard Meijer, Lotte Holmegaard, Jens H. Nielsen, Iftach Nevo, Jonas L. Hansen, and Henrik Stapelfeldt. Quantum-state selection, alignment, and orientation of large molecules using static electric and laser fields. *The Journal of Chemical Physics*, 131(6):064309, 2009.

[38] B. Friedrich and D. R. Herschbach. On the possibility of orienting rotationally cooled polar molecules in an electric field. *Zeitschrift fr Physik D Atoms, Molecules and Clusters*, 18(2):153–161, 1991.

[39] Takahige Fujiwara and Edward C. Lim. Binding energies of the neutral and ionic clusters of naphthalene in their ground electronic states. *Journal of Physical Chemistry A*, 107:4381–4386, 2003.

[40] R. Fulton, A. I. Bishop, and P. F. Barker. Optical stark decelerator for molecules. *Physical Review Letters*, 93(24):243004, 2004.

[41] E. Ganeshsrinivas, D. N. Sathyanarayana, K. Machida, and Y. Miwa. Simulation of the infrared spectra of acetamide by an extended molecular mechanics method. *Journal of Molecular Structure: THEOCHEM*, 361(1-3):217 – 227, 1996. Theoretical Chemistry in India.

[42] J. Gerhold. Properties of cryogenic insulants. *Cryogenics*, 38(11):1063–1081, 1998.

[43] M. C. Gordillo and J. Boronat. *he*4 on a single graphene sheet. *Phys. Rev. Lett.*, 102(8):085303, Feb 2009.

[44] T. R. Gosnell. Laser cooling of a solid by 65k starting from room temperature. *Opt. Lett.*, 24(15):1041–1043, 1999.

[45] C. I. Hancox. *Magnetic trapping of transition-metal and rare-earth atoms using buffer gas loading*. PhD thesis, Harvard University, 2005.

[46] J.G.E. Harris, R.A. Michniak, S.V. Nguyen, W.C. Campbell, D. Egorov, S.E. Maxwell, L.D. vanBuuren, and J.M. Doyle. Deep superconducting magnetic traps for neutral atoms and molecules. *Review of Scientific Instruments*, 75:17–23, 2004.

[47] A. Hatakeyama, K. Oe, K. Ota, S. Hara, J. Arai, T. Yabuzaki, and A. R. Young. Slow spin relaxation of rb atoms confined in glass cells filled with dense 4*he* gas at 1.85 k. *Physical Review Letters*, 84(7):1407–1410, 2005.

[48] J. R. Heath, R. F. Curl, and R. E. Smalley. The uv absorption spectrum of c60 (buckminsterfullerene): A narrow band at 3860 . *The Journal of Chemical Physics*, 87:4236–4238, 1987.

[49] G HERZBERG. Spectroscopic evidence of molecular hydrogen in the atmospheres of uranus and neptune. *Astrophysical Journal*, 115(3):337–&, 1952.

[50] Gerhard Herzberg. *Electronic spectra and electronic structure of polyatomic molecules: v. 3 : Molecular Spectra and Molecular Structure*. Van Nostrand Reinhold, 1966.

[51] Steven Hoekstra, Joop G. Gilijamse, Boris Sartakov, Nicholas Vanhaecke, Ludwig Scharfenberg, Sebastian Y. T. van der Meerakker, and Gerard Meijer. Optical pumping of trapped neutral molecules by blackbody radiation. *Phys. Rev. Lett.*, 98:133001, 2007.

[52] Steven Hoekstra, Markus Metsälä, Peter C. Zieger, Ludwig Scharfenberg, Joop J. Gilijamse, Gerard Meijer, and Sebastiaan Y. T. van de Meerakker. Electrostatic trapping of metastable nh molecules, Dec 2007.

[53] J M Hollis and D Phillips. *Jet Spectroscopy and Molecular Dynamics*. Springer, 2004.

[54] Lotte Holmegaard, Jens H. Nielsen, Iftach Nevo, and Henrik Stapelfeldt. Laser-induced alignment and orientation of quantum-state-selected large molecules. *Physical Review Letters*, 102:023001, 2009.

[55] Tao Hong, Alexey V. Gorshkov, David Patterson, Alexander S. Zibrov, John M. Doyle, Mikhail D. Lukin, and Mara G. Prentiss. Realization of coherent optically dense media via buffer-gas cooling. *Phys. Rev. A*, 79(1):013806, Jan 2009.

[56] Totaro Imasaka, Kaoru Hirata, and Nobuhiko Ishibashi. Supersonic jet fluorometry of aniline and its derivatives with a lamp excitation source. *Analytical Chemistry*, 57:59–62, 1985.

[57] Totaro Imasaka, David Moore, and Tuan Vo-Dinh. Critical assessment: use of supersonic je spectrometry for complex mixture analysis. *Pure Applied Chemistry*, 75(7):975998, 2003.

[58] H. Ito, K. Sakaki, M. Ohtsu, and W. Jhe. Evanescent-light guiding of atoms through hollow optical fiber for optically controlled atomic deposition. *Applied Physics Letters*, 70(19):2496–2498, 1997.

[59] M. J. Jamieson, A. Dalgarno, and J. M. Doyle. Scattering lengths for collisions of ground state and metastable state hydrogen atoms. *Molecular Physics*, 87:817–826, 1996.

[60] Du Jing and Zeng Pan. Molecular vibrational modes of c60 and c70 via finite element method. *European Journal of Mechanics - A/Solids*, 28(5):948 – 954, 2009.

[61] Charles Kittel and Herbert Kroemer. *Thermal Physics*. W.H. Freeman and Company, New York, 1980.

[62] T. M. Kojima, N. Kobayashi, and Y. Kaneko. Helium cluster ions rghex+ (rg=ne, ar and kr, $\leq$ 14) formed in a drift tube cooled by liquid helium. *Zeitschrift fr Physik D Atoms, Molecules and Clusters*, 22:645, 1992.

[63] Jochen Kupper, Frank Filsinger, and Gerard Meijer. Manipulating the motion of large neutral molecules. *Faraday Disc.*, 142, 2009.

[64] Samuel. Leutwyler and Joshua. Jortner. The adsorption of rare-gas atoms on microsurfaces of large aromatic molecules. *The Journal of Physical Chemistry*, 91(22):5558, 1987.

[65] Donald H. Levy. Laser spectroscopy of cold gas-phase molecules. *Annual Review Physical Chemistry*, 31:197–225, 1980.

[66] Albrecht Lindinger, J. Peter Toennies, and Andrey F. Vilesov. Laser-induced fluorescence spectra of tetracene complexes with ne, h2o, d2o inside he droplets. *Chemical Physics Letters*, 429(1-3):1 – 7, 2006.

[67] Kopin Liu. Crossed-beam studies of neutral reactions: State-specific differential cross sections. *Annual Review of Physical Chemistry*, 52:139–164, 2001.

[68] W. Majewski and W. Leo Meerts. Near-uv spectra with fully resolved rotational structure of naphthalene and perdeuterated naphthalene. *Journal of Molecular Spectroscopy*, 104:271–281, 1984.

[69] J. Mallinson. One-sided fluxes – a magnetic curiosity? *Magnetics, IEEE Transactions*, 9(4):678–682, Apr 1973.

[70] Jan M. L. Martin, Jamal El-Yazal, and Jean-Pierre Franois. Structure and vibrational spectrum of some polycyclic aromatic compounds studied by density functional theory. *Journal of Physical Chemistry*, 100(38):15358–15367, 1996.

[71] S. E. Maxwell, N. Brahms, R. deCarvalho, D. R. Glenn, J. S. Helton, S. V. Nguyen, D. Patterson, J. Petricka, D. DeMille, and J. M. Doyle. High-flux beam source for cold, slow atoms or molecules. *Physical Review Letters*, 95(17):173201, 2005.

[72] E Narevicius1, C G Parthey, A Libson, J Narevicius1, I Chavez, U Even, and M G Raizen1. An atomic coilgun: using pulsed magnetic fields to slow a supersonic beam. *New Journal of Physics*, 9:358, 2007.

[73] H.J. Neusser and H. Hrause. Binding energy and structure of van der waals complexes of benzene. *Chemical Reviews*, 94(7):1829–1843, 1994.

[74] B. Nolle, H. Nolle, J. Schmand, and H. J. Andra. Atomic-beam deflection by double-π-pulse laser technique. *EPL (Europhysics Letters)*, 33(4):261–266, 1996.

[75] Russell T Pack, Robert B. Walker, and Edward F. Hayes. Mechanisms of atomic and molecular recombination and collision-induced dissociation. *Chemical Physics Letters*, 3:255–262, 1997.

[76] D. Patterson and J.M. Doyle. A bright, guided molecular beam with hydrodynamic enhancement. *Journal of Chemical Physics*, 126:154307, 2007.

[77] David Patterson, Julia Rasmussen, and J.M. Doyle. Intense atomic and molecular beams via neon buffer-gas cooling. *New Journal of Physics*, 11, 2009.

[78] David Patterson, Julia Rasmussen, and John M Doyle. Intense atomic and molecular beams via neon buffer-gas cooling. *New Journal of Physics*, 11(5):055018 (12pp), 2009.

[79] David Patterson, Edem Tsikita, and John M. Doyle. Buffer gas cooling of naphthalene to 6 k. *Journal of Physical Chemistry*, to be published 2010.

[80] Hans Pauly. *Atom, Molecule, and Cluster Beams: Cluster beams, fast and slow beams*. Springer, 2000.

[81] C. J. Pethick and H. Smith. *Bose-Einstein Condensation in Dilute Gases*. Cambridge, 2002.

[82] Gabriel N. Price, S. Travis Bannerman, Kirsten Viering, Edvardas Narevicius, and Mark G. Raizen. Single-photon atomic cooling. *Phys. Rev. Lett.*, 100(9):093004, Mar 2008.

[83] S. A. Rangwala, T. Junglen, T. Rieger, P. W. H. Pinkse, and G. Rempe. Continuous source of translationally cold dipolar molecules. *Physical Review A*, 67:043406, 2003.

[84] Federick Reif. *Fundamentals of Statistical and Thermal Physics*. McGraw-Hill, 1965.

[85] T. Rieger, T. Junglen, S. A. Rangwala, P. W. H. Pinkse, and G. Rempe. Continuous loading of an electrostatic trap for polar molecules. *Physical Review Letters*, 95(17):173002, 2005.

[86] A. Roth. *Vacuum Technology*. North-Holland, Amsterdam, 1996.

[87] Brian Sawyer. Personal communication.

[88] S.Bohnert, K.-F. Klein, D. Dinges, W. Fuerstenberg, and D. Kalymnios. Fiber-delivery system for high-power uv-a lightsource. *SPIE-Proceedings*, 2006.

[89] M. Shirasaki. Large angular dispersion by a virtually imaged phased array and its application to a wavelength demultiplexer. *Opt. Lett.*, 21(5):366–368, 1996.

[90] Ian W. M. Smith and Bertrand R. Rowe. Reaction kinetics at very low temperatures: Laboratory studies and interstellar chemistry. *Accounts of Chemical Research*, 33(5), 2000.

[91] KM Smith, G Duxbury, DA Newnham, and J Ballard. High-resolution mid-IR molecular absorption spectroscopy of collisionally cooled hydrofluorocarbon vapours. *Journal of the chemical society-Faraday transactions*, 93(16):2735–2740, AUG 21 1997.

[92] C. Sommer, L.D. van Buuren, M. Motsch, S. Pohle, J. Bayerl, P.W.H. Pinkse, and G. Rempe. Continuous guided beams of slow and internally cold polar molecules. *Faraday Discussions*, 142:203, 2009.

[93] Steven Stiller and Murray V. Johnston. Supersonic jet spectroscopy with a capillary gas chromatographic inlet. *Analytical Chemistry*, 59:567–572, 1987.

[94] Benjamin K. Stuhl, Brian C. Sawyer, Dajun Wang, and Jun Ye. Magneto-optical trap for polar molecules. *Phys. Rev. Lett.*, 101(24):243002, Dec 2008.

[95] J. Stuhler, P. O. Schmidt, S. Hensler, J. Werner, J. Mlynek, and T. Pfau. Continuous loading of a magnetic trap. *Physical Review A*, 64:031405, 2001.

[96] A. O. Sushkov and D. Budker. Production of long-lived atomic vapor inside high-density buffer gas. *Phys. Rev. A*, 77(4):042707, Apr 2008.

[97] T. Takekoshi, J. R. Yeh, and R. J. Knize. Quasi-electrostatic trap for neutral atoms. *Optics Communications*, 114(5-6):421 – 424, 1995.

[98] Michael J. Thorpe, David Balslev-Clausen, Matthew S. Kirchner, and Jun Ye. Cavity-enhanced optical frequency combspectroscopy: application to human breathanalysis. *Opt. Express*, 16(4):2387–2397, 2008.

[99] J. Peter Toennies and Andrey F. Vilesov. Superfluid helium droplets: A uniquely cold nanomatrix for molecules and molecular complexes. *Angewandte Chemie International Edition*, 43:2622–2648, 2004.

[100] C. H. Townes and A. L. Schawlow. *Microwave Spectroscopy*. Dover Publications, 1955.

[101] L. D. van Buuren, C. Sommer, M. Motsch, S. Pohle, M. Schenk, J. Bayerl, P. W. H. Pinkse, and G. Rempe. Electrostatic extraction of cold molecules from a cryogenic reservoir. *Physical Review Letters*, 102(3):033001, 2009.

[102] L.D. van Buuren, C. Sommer, M. Motsch, S. Pohle, M. Schenk, J. Bayerl, P.W.H. Pinkse, and G. Rempe. Electrostatic extraction of cold molecules from a cryogenic reservoir. *Preprint, Arxiv:0806.2523v1*, 2008.

[103] Sebastian Y. T. van de Meerakker, Boris G. Sartakov, Allard P. Mosk, Rienk T. Jongma, and Gerard Meijer. Optical pumping of metastable NH radicals into the paramagnetic ground state. *Phys. Rev. A*, 68:032508, 2003.

[104] Jacqueline van Veldhoven, Hendrick L. Bethlem, and Gerard Meijer. ac electric trap for ground-state molecules. *Phys. Rev. Lett.*, 94(8):083001, Mar 2005.

[105] T. Vondrak, S. Sato, and K. Kimura. Zero kinetic energy photoelectron study of the naphthalene-ar van der waals complex. *Chemical Physics Letters*, 261:481–485, 1996.

[106] V. Vuletic, T. W. Hansch, and C. Zimmermann. Steep magnetic trap for ultra cold atoms. *Europhysics Letters*, 36:349–354, 1996.

[107] A C Vutha, W C Campbell, Y V Gurevich, N R Hutzler, M Parsons, D Patterson, E Petrik, B Spaun, J M Doyle, G Gabrielse, and D DeMille1. Search for the electric dipole moment of the electron with thorium monoxide. *preprint*, 2009. arXiv:0908.2412v1.

[108] J. Weinstein. Personal communication.

[109] J. D. Weinstein, R. deCarvalho, T. Guillet, B. Friedrich, and J. M Doyle. Magnetic trapping of calcium monohydride molecules at milliKelvin temperatures. *Nature*, 395:148–50, 1998.

[110] John E Wessel and Jack a Syage. Excitonic interactions in naphthalene clusters. *Journal of Physical Chemistry*, 94:737–747, 1990.

[111] DR Willey, RE Timlin, M Deramo, PL Pondillo, DM Wesolek, and RW Wig. Pressure broadening of NH3 by H-2 from 15 to 40 K. *Journal of Chemical Physics*, 113(2):611–615, JUL 8 2000.

[112] D. J. Wineland, R. E. Drullinger, and F. L. Walls. Radiation-pressure cooling of bound resonant absorbers. *Phys. Rev. Lett.*, 40(25):1639–1642, Jun 1978.

[113] Minzhong Xu and Zlatko Baic'. Wave function delocalization and large-amplitude vibrations of helium on corrugated aromatic microsurfaces: Tetracenehe and pentacenehe van der waals complexes. *Journal of Physical Chemistry*, 111(31):7653–7663, 2007.

[114] Xiao Hua Yang, Cindy Lee, and Mary I. Scranton. Determination of nanomolar concentrations of individual dissolved low molecular weight amines and organic acids in seawater. *Analytical Chemistry*, 65:572–576, 1993.

[115] B. Yu, F. Zeng, Y. Yang, Q. Xing, A. Chechin, X. Xin, I. Zeylikovich, and R.R. Alfano. Torsional vibrational modes of tryptophan studied by terahertz time-domain spectroscopy. *Biophysical Journal*, 86(3):1649 – 1654, 2004.